THESIS

Ultrafast Quantum Coherent Control Apparatus

Submitted by

Jesse Wilson

Electrical and Computer Engineering Department

COLORADO STATE UNIVERSITY

May 21, 2007

WE HEREBY RECOMMEND THAT THE **THESIS** PREPARED UNDER OUR SU-PERVISION BY **JESSE WILSON** ENTITLED **ULTRAFAST QUANTUM CO-HERENT CONTROL APPARATUS** BE ACCEPTED AS FULFILLING IN PART REQUIREMENTS FOR THE DEGREE OF MASTER OF SCIENCE.

<u>Committee on Graduate Work</u>

Jorge Rocca

Nancy Levinger
(Chemistry Deparment)

...

Randy Bartels
Adviser

Anthony Maciejewsky
Department Head/Director

ABSTRACT OF THESIS

Ultrafast Quantum Coherent Control Apparatus

In recent years, the availability of ultrafast laser sources has opened up a number of op-
portunities for exploring molecular dynamics that take place on femtosecond time scales.
Coherent control experiments involve creating, manipulating, and measuring these ultrafast
phenomena. Such controllable processes include second harmonic generation (SHG), cre-
ation of vibrational wavepackets, high-harmonic generation, photodissociation, and more.

The foundation to all these experiments is an ultrafast pulse shaper and a high-dimensional
search algorithm. Here we present the design and construction of a spectral phase-only pulse
shaper, including details on alignment and calibration. We also demonstrate the function-
ality of the device by producing several pulse profiles that could be potentially useful in
coherent control experiments. A covariance matrix analysis evolutionary strategy (CMA-
ES) is also implemented, and demonstrated to optimize SHG in a nonlinear crystal.

Finally, recognizing that phase-only shapers cannot produce the full range of temporal
shapes available to a given input pulse, we show the design and construction of a pulse
shaper which uses only a single linear phase mask to gain control over both spectral phase
and amplitude by use of phase gratings.

Jesse Wilson
Electrical and Computer Engineering Department
Colorado State University
Fort Collins, Colorado 80523
Fall 2007

ACKNOWLEDGEMENTS

Και παν ο τι εαν ποιητε εκ ψυχης εργαζεσθη ως τω κυριω και ουκ ανθρωποις.

—*Προϵ Κολοσσαεις 3:23*

Ουχ οτι ηδη ελαβον η ηδη τετελειωμαι διωκω δϵ ει και καταλαβω ϵφ και κατελημφθϵν υπο χριστου.

—*Προϵ Φιλιππησιους 3:12*

Contents

List of Tables

List of Figures

Chapter I

INTRODUCTION

The use of high-powered lasers to control quantum mechanical systems emerged in the early 1990s. As predicted in *Coherent Control of Quantum Dynamics: The Dream Is Alive* [1], the field of quantum control has advanced rapidly over the years. Experiments have ranged from the control of electronic dynamics, molecular vibrations and rotations, to influencing the selectivity and yield of high harmonic generation [2, 3]. The three most important enabling technologies in this field are lasers that generate ultrafast pulses, the Fourier transform pulse shapers that sculpt these pulses into useful control fields, and computer learning algorithms which search for control fields to give the desired results. The content of this thesis will focus on the design and construction of pulse shapers, the development of a genetic algorithm, and the application of one of these instruments in a simple coherent control experiment.

Development of methods for manipulating quantum systems with laser light is motivated by a number of potential applications: selective bond dissociation in polyatomic molecules [4], generating novel reaction products [5], influencing chemical reactions [6], probing quantum dynamics [7, 8], and more. Early experiments to manipulate molecules with light failed because they did not take into account the wave nature of the quantum systems they sought to control [1]. The problem of designing a control signal requires full knowledge of the Hamiltonian, which is only known for the simplest of systems. In 1992, Judson and Rabitz proposed using a closed-loop apparatus with a learning algorithm to discover control fields that yield a target result [9]. This idea paved the way for the first successful use of genetic algorithms, in conjunction with pulse shaping technology, in a laboratory experiment to control molecules [10].

Modern pulse shaping technology emerged from research and development of picosecond pulse compressors. In 1973, Desbois *et al.* found that by spectral filtering, that is by

blocking certain frequency components at the Fourier plane of a Treacy grating compressor, they were able to manipulate the temporal shape of picosecond pulses [11]. Agostinelli *et al.* extended this work by inserting pieces of glass at the Fourier plane, retarding the affected frequency components by an amount specified by the thickness and material dispersion of glass. These early phase masks were capable of producing double pulses, adding linear chirp, and other interesting shapes. A more thorough analysis of picosecond pulse shaping was compiled by Froehly *et al.* [12], where the authors present a detailed spatio-temporal analysis of pulse shaping, and introduce the concept of using a zero-dispersion Martinez stretcher. This approach allows the pulse shaper to be used with transform-limited pulses while preserving their short duration.

This technique, which Froehly *et al.* labeled shaping by Fourier analysis [12], was extended to femtosecond pulses by Weiner *et al.* [13] in 1988. Here they demonstrated masks to produce pulse trains and square pulses; this was quite a feat considering each pulse shape was the result of a unique fixed mask created using microlithography techniques. The authors proposed that in the future the masks could be replaced with dynamic spatial light modulators (SLM), which could be programmed to produce an arbitrary shape. While such devices had already been demonstrated with picosecond pulses, it was not until 1990 that Weiner *et al.* built a pulse shaper using a liquid crystal modulator with sufficient resolution to shape femtosecond pulses [14, 15]. Weiner has published a more recent, thorough review of pulse shaping technology [16], which discusses the various modulation technologies: liquid crystal, acousto-optic, and deformable mirror modulators.

The second chapter of this thesis focuses on a spectral phase only pulse shaper. First the physics of the device are discussed. Then design considerations are discussed while each parameter and decision is derived and explained. With these design parameters carefully chosen, the mechanical aspects of the design can be found in Appendix A. Chapter 2 then continues with a theoretical treatment of the performance characteristics of our design. Then we present a procedure for calibrating the pulse shaper, and demonstrate and measure its capabilities. There are two additional appendices relevant to this chapter. Appendix B details a procedure for aligning the shaper, while Appendix C explores practical

considerations of pulse measurement and characterization.

In Chapter 3, we present a unique approach to simultaneous spectral phase- and amplitude-shaping, which utilizes a single, high-resolution, phase-only SLM. This chapter includes the theoretical background, design, and two implementations of the shaper. We also present experimental results demonstrating the shaper's capabilities.

The fourth chapter covers the details of the search algorithm we use to control the pulse shaper. First we discuss closed-loop control, the central concept to coherent control experiments. Then we consider the nature of the search space, presenting the need for an efficient algorithm that is well suited for enormous search spaces. This leads to brief review of evolutionary strategies and genetic algorithms and their history of application in the field of coherent control. Given the unique requirements of the search space, a covariance matrix adaptation evolutionary strategy (CMA-ES) is implemented. Then we present the first experimental application of this coherent control apparatus: pulse compression. The experiment aims to compress an arbitrary ultrafast pulse to its bandwidth-limited duration, thereby compensating for any dispersive material the pulse has propagated through. The chapter is divided into a theoretical discussion and simulation, followed by laboratory experimental results. These results show that the algorithm and pulse shaper are fundamentally working as designed, as well as demonstrate the advantage of using CMA-ES.

The final chapter summarizes the work presented, and investigates future applications of the coherent control apparatus. These include controlling vibrational dynamics, vibrational overtone spectroscopy, and using coherent control as a contrast mechanism in microscopy.

Chapter II

ULTRAFAST PULSE SHAPING

In order to generate a useful control signal, a pulse shaper modulates the ultrafast pulses before the experiment. In this chapter we describe the parameters and decisions made in our particular design, with mathematical details. Section 2 analyzes the performance limitations and characteristics of the design, showing the resolution and temporal extents attainable with our shaper. Section 3 outlines calibration procedures and shows the typical results. The next section presents a few pulse shapes generated in the laboratory to verify the calibration procedure and confirm that the device performs as expected. Finally in the last section we discuss the lessons learned from working with this apparatus in the lab and present a few improvements that can be made to the design.

There are three relevant appendices found at the end of this thesis: technical drawings are presented in Appendix A, while alignment procedures are detailed in Appendix B, and details of our pulse measurement techniques are in Appendix C.

2.1   Background

2.1.1   Principles of Operation

Shaping ultrafast pulses ($\sim$ 30 fs duration) in the time-domain requires an even faster modulator. A Fourier transform pulse shaper circumvents this need by manipulating the pulses in the spectral domain. This is accomplished by the use of a grating and a lens to map the various frequency components, spatially, to a line (the Fourier transform), which passes through a modulator that may manipulate the phase and/or amplitude of each frequency component individually, to be reconstructed by a second, commensurate lens and grating pair (the inverse Fourier transform). The process is analogous to the technique in digital signal processing of performing an FFT (fast Fourier transform) on the input, manipulating the data in the frequency domain, and performing an IFFT (inverse fast Fourier transform)
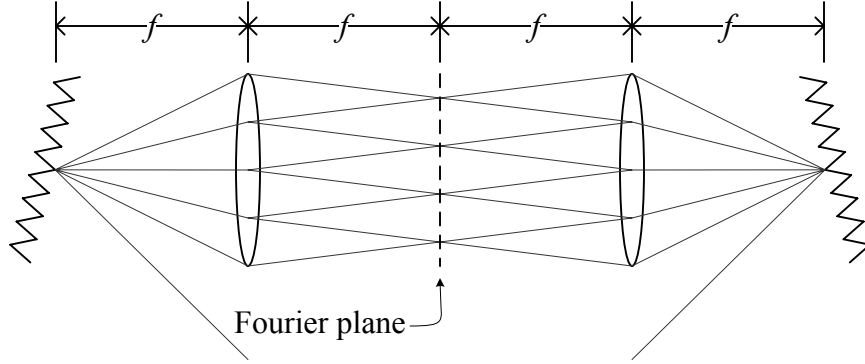
Figure 1: Martinez stretcher layout.

to construct the output signal.

The Fourier transform pulse shaper is based on a zero-dispersion Martinez stretcher [17]. In a stretcher, one grating angularly disperses the light, while the second reconstructs the pulses. The geometry and separation between the gratings determines the relative path lengths of the different spectral components. This device is commonly used in chirped-pulse amplification systems to stretch the pulses before amplification and compress after amplification. A Martinez stretcher uses a pair of lenses between the gratings as shown in Fig. 1. When the optics are placed such that each element is a focal length away from the adjacent elements, the resulting setup neither compresses nor stretches the pulses. Such a configuration, which meets the so-called $4f$ condition, results in an equal path length for all the frequency components and is therefore called a zero-dispersion stretcher. The focal plane between the lenses, called the Fourier plane, comprises the spatially-mapped, focused frequency components. By placing a spatial light modulator (SLM) here, we can perform the required filtering by either attenuating the frequency components (an amplitude mask) or retarding them (a phase mask), or both.

2.2 Design and Construction

A number of constraints have to be considered in the design of a pulse shaper. The most crucial element of the design is the SLM. We concern ourselves with phase-only modulators, in order to avoid losses inherent in amplitude shaping and reduce overall cost. Most spectral

phase shapers use one of three SLM devices: liquid crystal arrays (LC-SLM), acousto-optic modulators (AOM), or deformable mirrors (DM) [16]. We are interested in generating high-energy control pulses, so the low efficiency of AOM technology (10-15%) is a severe drawback. Deformable mirrors are extremely efficient, due to their reflective nature, but can only produce smooth phase masks because of the minimum bending radius of the metallic membrane. Sharp discontinuities characteristic of more complex pulse shapes are not possible. However, LC-SLMs do not have these specific limitations. Their transmission efficiency is typically greater than 90%, while each adjacent pixel can have a sharply different phase, limited by adjacent pixel cross-talk. For these reasons, we base our design around a LC-SLM: 640-pixel phase mask SLM built by Cambridge Research Instrumentation (CRi). An LC-SLM operates by applying a specified voltage across each of the individual pixels. Incident light of a linear polarization will see a refractive index that increases with drive voltage, while orthogonally polarized light will not be retarded. Our SLM is therefore only capable of shaping horizontally polarized incident light.

2.2.1 Design Parameters

The aperture of the SLM determines the spatial size of the beam that will pass through the pulse shaper. In order to make full use of the resolution of the phase mask, the focusing optics must focus each frequency component down to the size of a single pixel (100 μm) at the Fourier plane [16]. We consider a $4f$ shaper with focal length f. From the theoretical considerations in [18], the expression for the focused $1/e^2$ Gaussian beam intensity radius, w_0, at the Fourier plane is

$$w_0 = \frac{\cos\theta_{\text{in}}}{\cos\theta_{\text{d}}}\left(\frac{f\lambda}{\pi w_{\text{in}}}\right), \tag{1}$$

with an input beam radius w_{in} at wavelength λ, where θ_{in} is the angle of the input beam incident on the grating, relative to the grating normal, and θ_{d} is the diffracted angle. As we will discuss later, the final design of the pulse shaper will place the gratings in a Littrow configuration for the central wavelength λ_0, so that $\theta_{\text{in}} = \theta_{\text{d}}$ and Eq. (1) reduces to

$$w_0 = \frac{f\lambda_0}{\pi w_{\text{in}}}. \tag{2}$$

In our pulse shaper, we use cylindrical focusing optics that only focus the spectrally-dispersed axis. The design problem is to select a focal length that matches $2w_0 \equiv d_0$ to the pixel width, while using an input beam size that fits inside the aperture 5 mm vertical aperture of the SLM. For these purposes we define the input beam diameter D such that the energy within that diameter is 99% of the total beam energy. Under these conditions, we have the following expression from Siegman (pg. 676) [19]:

$$d_0 = 2w_0 \approx \frac{2f\lambda_0}{D}. \tag{3}$$

We use a cylindrical focusing optic, so the input beam diameter is set by the SLM aperture in the un-dispersed direction: $D = 5$ mm; anything outside this will be clipped. Given the center wavelength of our laser is $\lambda = 780$ nm, we calculate $f = 320$ mm.

Once the focal length is determined, we select an appropriate groove density to map the entire bandwidth of the input pulses to the phase mask aperture. The aperture behaves as a spectral window, as described in early pulse shaping experiments [20, 21]. The time-domain effect of spectral windowing acts to convolve the input pulse with a sinc function whose width is inversely related to the window's spectral width. Hence a wide window will have little effect on the pulse, while a narrow window will broaden the pulse and leave temporal side lobes. In selecting a grating, we minimize the spectral windowing distortions while seeking to project the narrowest optical bandwidth possible onto each pixel, lending to high spectral resolution of the phase mask.

We begin with the (first order) grating equation,

$$G\lambda = \sin\theta_{\mathrm{in}} + \sin\theta_{\mathrm{d}}, \tag{4}$$

where G is the grating groove density, θ_{in} is the incident angle measured from the grating surface normal, and θ_{d} is the angle of the refracted light as shown in Fig. 2. For maximum efficiency, we set the grating in Littrow configuration for the center wavelength λ_0:

$$G\lambda_0 = 2\sin\theta_{\mathrm{in}} \tag{5}$$
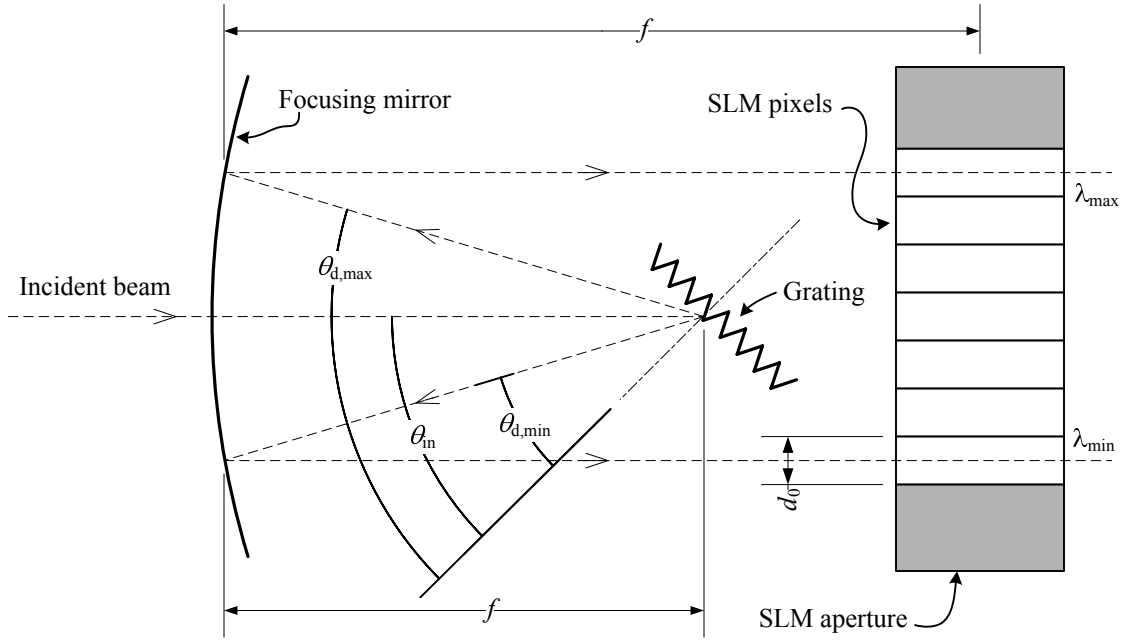
Figure 2: Diagram of spectral windowing extents. The SLM aperture clips the spectrum beyond $\lambda_{\min}$ and $\lambda_{\max}$. Note the distance between the SLM and the focusing mirror is f, and is exaggerated here for illustration clarity.

Table 1: Spectral extents for a few common selected grating groove densities.

G (mm^{-1})	$\lambda_{\min}$ (nm)	$\lambda_{\max}$ (nm)	$\Delta\lambda$ (nm)
600	614	942	313
830	663	893	231
1200	703	853	149
1800	738	818	80
2400	763	793	30

The diffracted angles of the spectral extents are

$$\sin\theta_{\mathrm{d,min}} = G\lambda_{\min} - \sin\theta_{\mathrm{in}}$$
$$\sin\theta_{\mathrm{d,max}} = G\lambda_{\max} - \sin\theta_{\mathrm{in}}$$

(6)

Table 1 lists a few common grating groove densities to the bandwidth that falls within the aperture, which is ~ 68 mm wide.

Here we used a numerical approach to select the most dispersive grating possible that does not lead to temporal distortions in the pulse. The model begins by constructing a

8

transform-limited Gaussian pulse of the form

$$E_{\text{in}}(t) = \exp\left(-at^2\right)\exp\left(i\omega_0 t\right), \tag{7}$$

where $a = 2\ln 2/\tau_p^2$ is related to the the full width at half maximum duration of the pulse (τ_p), and ω_0 is the central frequency. For our design, we used a pulse with $\tau_p = 30$ fs, and a central wavelength of 780 nm. Next we perform a Fourier transform, analogous to the action of the grating and focusing optic.

$$E_{\text{in}}(\omega) = \mathcal{F}\left\{E_{\text{in}}(t)\right\} \tag{8}$$

To simulate the physical extents of the phase mask, we set the frequency components outside the aperture to zero,

$$E_{\text{out}}(\omega) = \begin{cases} 0 & \omega < \omega_{\text{min}} \text{ or } \omega > \omega_{\text{max}}, \\ E_{\text{in}}(\omega) & \text{otherwise}. \end{cases} \tag{9}$$

Then we reconstruct the temporal output pulse with an inverse Fourier transform and observe the pulse broadening due to the spectral apodization. Figure 3 shows the resulting FWHM pulse duration for a range of gratings. In order to maintain the 30 fs transform-limited duration of the input pulses, we selected a 1200mm^{-1} grating, with a gold coating to maximize efficiency for near-IR light.

2.2.2 Spatial Dispersion Characteristics

Here we derive the angular dispersion relationship for a grating-based shaper, determining the mapping of frequency to spatial position at the Fourier plane, $\alpha = dx/d\omega$, arriving at the results in [16]. We begin by differentiating Eq. (4), leaving θ_{in} fixed:

$$d\lambda = G^{-1}\cos\theta_{\text{d}} \; d\theta_{\text{d}}. \tag{10}$$

Light at $\lambda_0 + d\lambda$ diffracted at an angle $\theta_{\text{d}} + d\theta_{\text{d}}$ from the grating which travels a distance f, will diverge from the center wavelength by a distance dx, as related by simple geometry:

$$\frac{dx}{f} = \tan d\theta_{\text{d}} \approx d\theta_{\text{d}}. \tag{11}$$
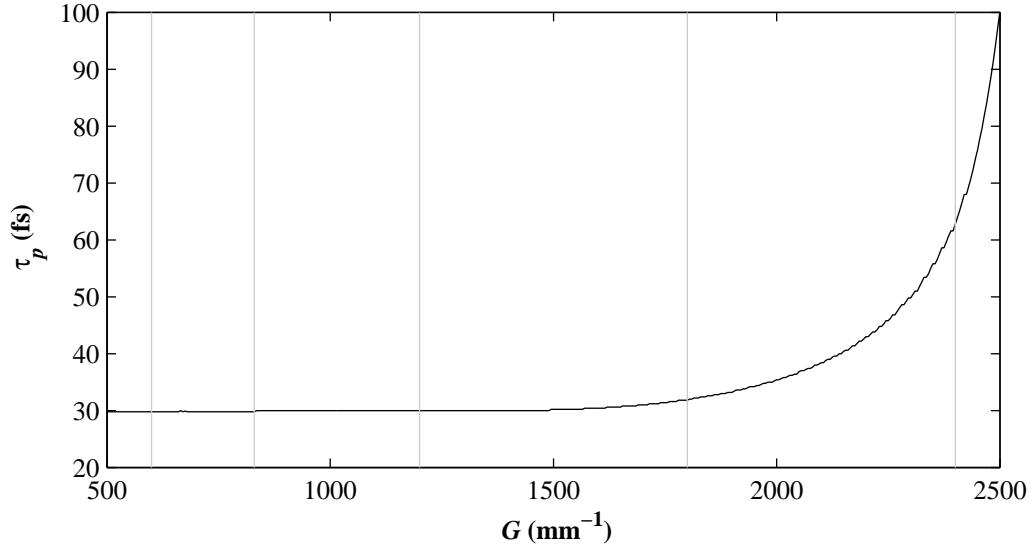
Figure 3: Increase in pulse intensity temporal FWHM τ_p due to spectral apodization with increased grating groove density for a mask of width 65.278 mm and $f = 320.5$ mm. Gray lines mark a few common availably groove densities.

Combining this with Eq. (10) yields the relationship we seek,

$$\frac{dx}{d\lambda} = \frac{Gf}{\cos\theta_{\mathrm{d}}}. \tag{12}$$

Finally we convert from wavelength to angular frequency, $dx/d\omega = -\lambda_0^2/\left[2\pi c(d\lambda/dx)\right]$:

$$\frac{dx}{d\omega} = \frac{-\lambda_0^2 G f}{2\pi c \cos\theta_{\mathrm{d}}} \equiv \alpha, \tag{13}$$

where c is the velocity of light in a vacuum. For our pulse shaper design, $\alpha = 141$ mm rad^{-1} fs.

2.2.3   Layout

The layout of our pulse shaper is based on the design put forth by Präkelt *et al* [22]. The advantages of this layout are in setting the gratings in Littrow configuration to maximize efficiency, using reflective optics to avoid dispersion and transmission losses of glass lenses, and compactness. A computer-aided design package (SolidWorks) was used to design the pulse shaper and all the mirror mounts and spacers. Appendix A contains drawings of the custom parts and assemblies. Aside from the translation, rotation, and goniometer stages, and the Newport mirror mount, all parts were custom built in the machine shop. The stages were purchased from OptoSigma.

10

2.3   Theoretical Performance Characteristics

Here we discuss the theoretical performance limits of this pulse shaper design. The pulses coming out of the shaper can be thought of as being synthesized by a number of individual frequency components. The first limitation implied is that the output pulse cannot exhibit temporal features faster than the bandwidth limit of the input pulse or shaper aperture. However, the temporal precision of the shaper can be smaller than the bandwidth limit of the pulse. For instance, if we apply a linear spectral phase, which has the effect of shifting, or delaying, the pulse in time, it should be possible to delay the pulse by a fraction of its duration.

We would like to arrive at an expression for the frequency filter of the pulse shaper, $H(\omega)$. Following the analysis of Thurston *et al.* [20] and Weiner [18], we consider an input pulse in space and time

$$E_{\text{in}}(x,t) = \frac{1}{2\pi} \int d\omega\, E_{\text{in}}(\omega) e^{-x^2/w_{\text{in}}^2} e^{i\omega t}. \tag{14}$$

The grating and the focusing optic manipulate each frequency component of the pulse so that the Fourier representation of the pulse just before the mask is

$$E_{\text{m-}}(x,\omega) \sim E_{\text{in}}(\omega) e^{-(x-\alpha\omega)^2/w_0^2}, \tag{15}$$

with w_0 and α defined in Eqs. (1) and (13), respectively. After applying the complex mask $M(x)$, the pulse becomes

$$E_{\text{m+}}(x,\omega) \sim E_{\text{in}}(\omega) e^{-(x-\alpha\omega)^2/w_0^2} M(x). \tag{16}$$

The above expression depends on both space and frequency, whereas we seek an expression only in terms of frequency. Here we decompose the field into Hermite-Gaussian modes and assume that all but the lowest order mode will be diffracted to large angles, and can be discarded [16]. The resulting frequency filter can be shown to be [18]

$$H(\omega) = \left(\frac{2}{\pi w_0^2}\right)^{1/2} \int M(x) e^{-2(x-\alpha\omega)^2/w_0^2}\, dx. \tag{17}$$

11

For an infinite resolution mask (i.e. non-pixellated), we can determine the frequency response by evaluating the above expression with a delta function in place of the mask,

$$M(x) = \delta(x) \equiv \begin{cases} 1 & x = 0, \\ 0 & x \neq 0. \end{cases} \tag{18}$$

$$H(\omega) = \left(\frac{2}{\pi w_0^2}\right)^{1/2} \int_{\infty}^{-\infty} \delta(x) \cdot e^{-2(x-\alpha\omega)^2/w_0^2} \, dx \tag{19}$$

By change of variable, $x' = \sqrt{2}(x - \alpha\omega)/w_0$, this becomes

$$H(\omega) = \frac{1}{\sqrt{\pi}} \int_{\infty}^{-\infty} \delta(\frac{w_0}{\sqrt{2}}x' + \alpha\omega) \cdot e^{-x'^2} \, dx' = \frac{1}{\sqrt{\pi}} e^{-2(\alpha\omega)^2/w_0^2} \tag{20}$$

Therefore the frequency response is a Gaussian with a full width at half maximum of $\delta\omega = \sqrt{2\ln 2} \cdot w_0/\alpha$, which depends on the spot size and the grating dispersion. For our pulse shaper design $\delta\omega = 0.79$ rad/ps $= 2\pi$ rad $\times$ 126 MHz.

In reality, the SLM is pixellated. We can use Eq. (17) to determine the response of a single pixel of width Δx by applying a mask that transmits light through a single pixel width and blocks all other frequencies:

$$M_{\text{pix}}(x) = \begin{cases} 1 & |x| < \Delta x/2, \\ 0 & \text{otherwise.} \end{cases} \tag{21}$$

This time the frequency response, Eq. (20), becomes:

$$\begin{aligned} H_{\text{pix}}(\omega) &= \left(\frac{2}{\pi w_0^2}\right)^{1/2} \frac{w_0}{\sqrt{2}} \int_{\sqrt{2}(-\Delta x/2-\alpha\omega)/w_0}^{\sqrt{2}(\Delta x/2-\alpha\omega)/w_0} e^{-x'^2} dx' \\ &= \frac{1}{2} \operatorname{erf}\left[\frac{\sqrt{2}(\Delta x/2 - \alpha\omega)}{w_0}\right] - \frac{1}{2} \operatorname{erf}\left[\frac{\sqrt{2}(-\Delta x/2 - \alpha\omega)}{w_0}\right] \end{aligned} \tag{22}$$

For our particular pulse shaper configuration, we can numerically solve for width of this profile, resulting in $\delta\omega_{\text{pix}} = 1.38$ rad/ps $= 2\pi$ rad $\times$ 219 MHz, which is 70% broader than the bandwidth of the infinite-resolution mask.

Figure 4 shows the effects of focal spot size w_0 on the frequency response of a single pixel. Tighter focusing does not narrow the bandwidth of a single pixel, but results in a sharper profile. The primary drawback to a smaller focal spot is that since the input
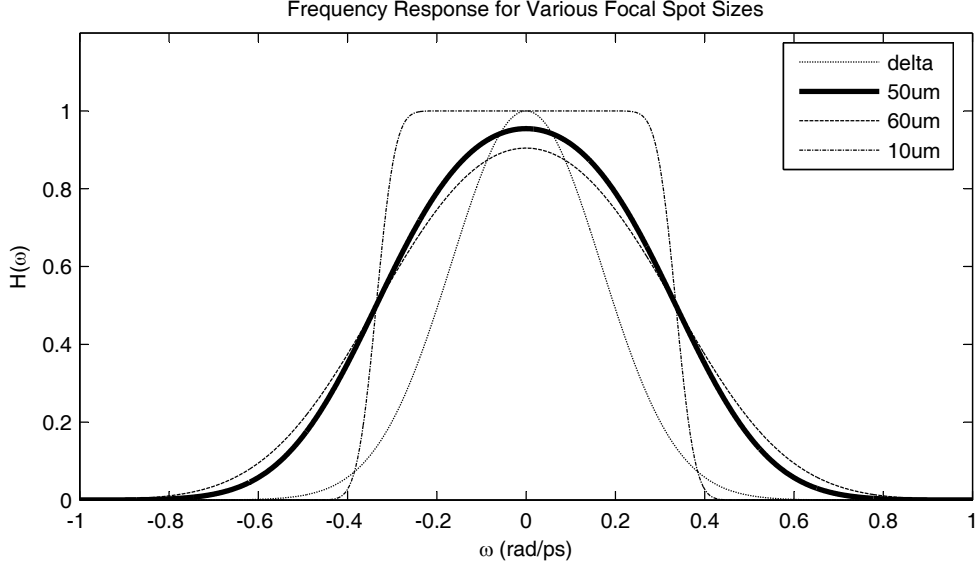
Figure 4: Frequency response of a single SLM pixel for several focal spot sizes. The dotted line (delta) is the response of an infinite resolution mask with a $w_0 = 50\mu$m focal spot. The other lines show the frequency response of a mask with $\Delta x = 100\mu$m pixels, varying the w_0 radius at the focus.

beam size is fixed by the SLM aperture height, we require a shorter-f optic, which in turn demands that we use a more dispersive grating in order to fill the SLM with the pulse spectrum. With our layout, the shorter focal length will draw the components together and require a larger angle on the input grating to avoid clipping the beam on the fold mirror; we tried to keep this angle as close to normal as possible to avoid aberrations. However, a more dispersive grating would have the advantage of increasing α, and thereby reducing the infinite-resolution mask bandwidth $\delta\omega$.

Now we examine three practical limitations on the synthesized pulse shape: minimum linear delay, maximum linear delay, and maximum quadratic phase. First, we find the smallest delay that can be imparted by applying a linear phase. This delay will be governed by the minimum slope:

$$\Delta\tau_{\min} = \frac{\Delta\phi_{\min}}{\Delta\omega}, \tag{23}$$

where $\Delta\phi_{\min} = 0.01$ rad is the minimum phase difference corresponding to one pixel drive level. As we will find in the section on calibration, $\Delta\omega = \Delta x/\alpha = 0.71$ rad/ps (not to be confused with $\delta\omega$). Thus $\Delta\tau_{\min} = 14$ fs, limited by the phase resolution of the SLM and

13

α. Second, we find the largest delay by examining the largest slope of linear phase the shaper can impart, which is just under π per pixel; any more than this, and the slope will be negative.

$$\Delta\tau_{\max} \leq \frac{\pi}{\Delta\omega} = 4.5 \text{ ps.} \tag{24}$$

Finally we determine the upper limit on quadratic phase, to give an idea of the shaper's pulse compression capabilities. The slope of the parabola is limited to π per pixel at the edges of the bandwidth to be shaped. We examine a quadratic spectral phase

$$\phi(\omega) = \tfrac{1}{2} b(\omega - \omega_0)^2 \tag{25}$$

where b corresponds to a length z of dispersive material according to

$$b = \frac{d^2\phi}{d\omega^2} = \frac{d^2k}{d\omega^2} z. \tag{26}$$

The slope at a particular frequency ω is given by

$$\frac{d\phi}{d\omega} = b(\omega - \omega_0), \tag{27}$$

which increases in absolute value as ω moves away from ω_0. Suppose we want to apply a quadratic phase across an optical bandwidth $\Delta\Omega$. The constraint on the maximum curvature is

$$\frac{b\Delta\Omega}{2} \leq \frac{\pi}{\Delta\omega}. \tag{28}$$

In other words,

$$b \leq \frac{2\pi}{\Delta\Omega\,\Delta\omega}. \tag{29}$$

For instance when we consider applying quadratic spectral phase across the entire SLM ($\Delta\lambda = 140$ nm, or $\Delta\Omega = 0.18$ rad/fs), we find the maximum quadratic phase is $b = 0.02$ ps^2/rad, which corresponds to ~ 46 cm of BK7 glass. The actual amount of material dispersion the shaper can compensate for will depend on the bandwidth of the pulses, and additional higher-order phase imparted by the material.

2.4   Calibration

When we first applied the pulse shaper to the pulse compression task in Chapter 4, we programmed the algorithm to directly control the SLM drive voltages to generate phase

masks. The algorithm converged, and demonstrated a limited capacity to compress pulses. But the resulting masks could not be easily interpreted. Furthermore, it was not possible to produce consistent, predictable temporal shapes without knowing the phase response of the SLM. To find the phase imparted by the pulse shaper, we use a spectral interferometry (SI) technique. Using a phase reconstruction algorithm [23], we determine the phase that a particular set of voltages applied to the SLM imparts on the shaped pulse.

2.4.1 Method

At first we placed the pulse shaper in one arm of a Mach-Zehnder interferometer, as shown in Fig. 5. We found that fluctuating air currents and mechanical vibrations, led to a noisy interference pattern. The phase noise, up to π rad, were severe enough that we could not even calibrate wavelength to SLM pixel. Surrounding the setup with an enclosure to minimize air currents helped, but the reconstructed phase was still noisy. Vastly more stable interference fringes were measured by a common-path measurement, where both the reference and probe pulses travel through the pulse shaper. Here we exploit the fact that the SLM shapes only one polarization, leaving the orthogonal polarization unmodulated [14]. Apart from the noise, we verified that the phase measurements using the common path and Mach-Zehnder techniques yield the same results.

To generate the delayed pair of pulses, a birefringent crystal is inserted before the pulse shaper to delay the reference polarization, as shown in Fig. 6. The crystal is KDP, $l = 12$ mm thick, cut at $45°$ for Type I SHG phase matching with 800 nm incident light. To find the delay, we use the group velocity index,

$$n_g = n(\omega_0) + \omega \frac{dn}{d\omega}\bigg|_{\omega_0} \tag{30}$$

The group velocity indices at 780 nm for the ordinary and extraordinary axes respectively are $n_{g,o} = 1.527$ and $n_{g,e} = 1.501$ at $\theta = 45°$, where θ is the angle between the optical axis of the crystal and the direction of propagation of the light [24]. The group velocities given by $v_g = c/n_g$ then determine the delay between the two pulses accordingly:

$$\tau_0 = \left(\frac{1}{v_{g,o}} - \frac{1}{v_{g,e}} \right) l = 960 \text{ fs} \tag{31}$$

15
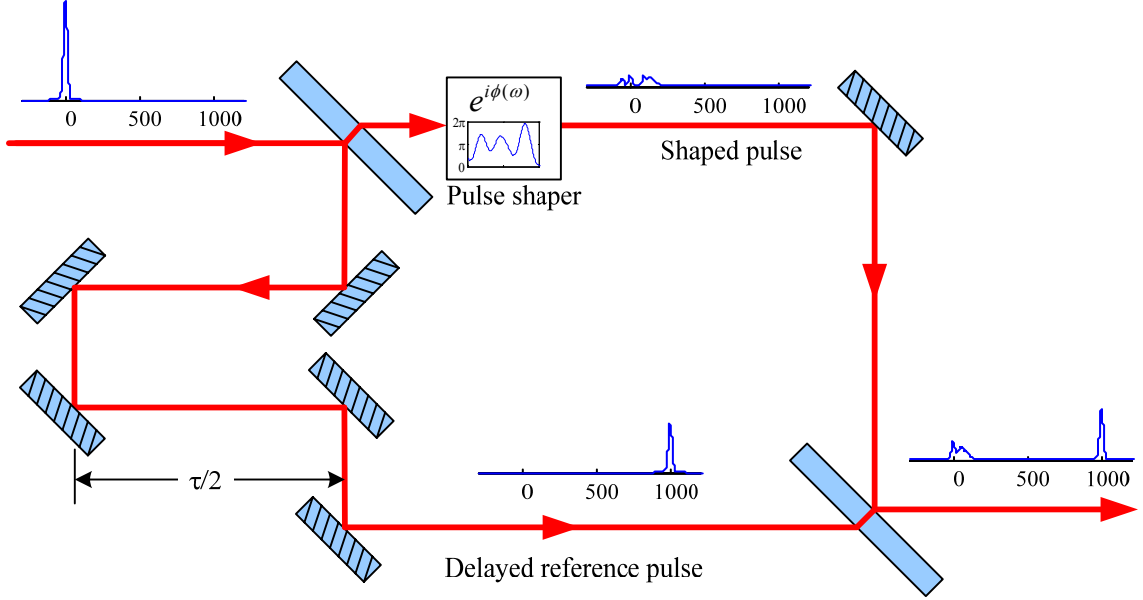
Figure 5: Diagram of Mach-Zehnder interferometer used for phase calibration.

After the pulse shaper, a polarizer projects both components along the same linear polarization so they will produce a spectral interference pattern on a spectrometer. Each spectral interferogram records the phase difference between the reference arm and the shaped arm:

$$\phi(\omega) = \phi_{\text{shaper}}(\omega) - \phi_{\text{reference}}(\omega) \tag{32}$$

For reference, we first apply a mask of all zeros to the SLM and measure the phase difference between the shaped and reference pulses

$$\phi_0(\omega)_1 = \phi_{\text{shaper, zero}}(\omega) - \phi_{\text{reference}}(\omega). \tag{33}$$

To find the phase imparted by the phase mask itself, we subtract $\phi_0(\omega)$, which was produced by applying all zeros to the SLM, and the phase of the reference arm $\phi_{\text{reference}}(\omega)$ cancels out. The phase then imparted by a pulse shaper mask is

$$\phi_{\text{mask}}(\omega) = \phi_1(\omega) - \phi_0(\omega) = \phi_{\text{shaper, mask}}(\omega) - \phi_{\text{shaper, zero}}(\omega). \tag{34}$$

16
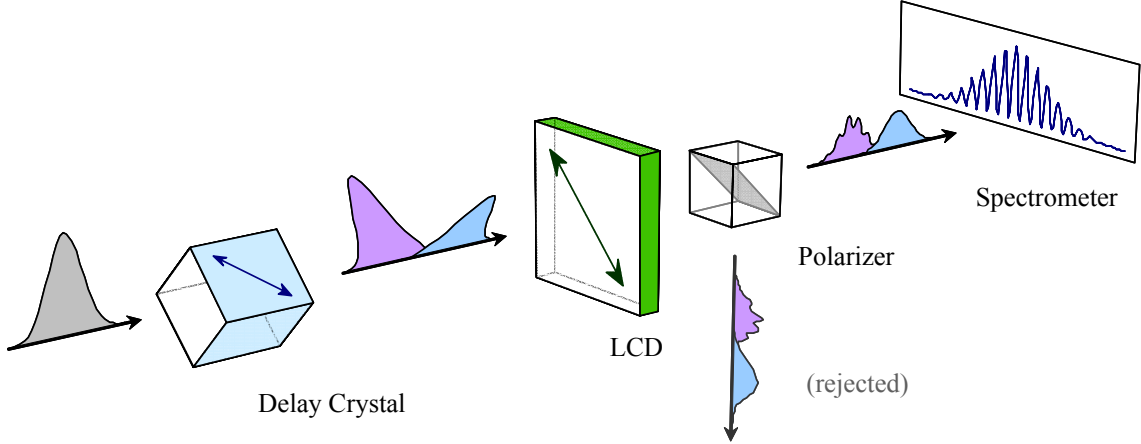
Figure 6: Pulse splitting with a birefringent crystal for use in inline interferometry. One pulse is shaped, while the orthogonal pulse is un-shaped and acts as a reference for interferometry. Credit: Philip Schlup.

2.4.2   Phase Retrieval

To retrieve phase information from the recorded interferograms, we employ the technique described by Takeda *et al.* [23], which originally described numerical analysis of off-axis holography.

We start with a probe and a time-delayed reference pulse,

$$E_0(\omega) = A_0(\omega)e^{i\phi_0(\omega)} \tag{35}$$

$$E_m(\omega) = A_m(\omega)e^{i\phi_m(\omega)} \tag{36}$$

$$E_r(\omega) = A_r(\omega)e^{i\phi_r(\omega)}e^{i\tau_0\omega} \tag{37}$$

We measure two interferograms, one with the zero mask, and one with an applied phase mask.

$$S_0(\omega) = |E_r(\omega) + E_0(\omega)|^2 \tag{38}$$

$$S_m(\omega) = |E_r(\omega) + E_m(\omega)|^2 \tag{39}$$
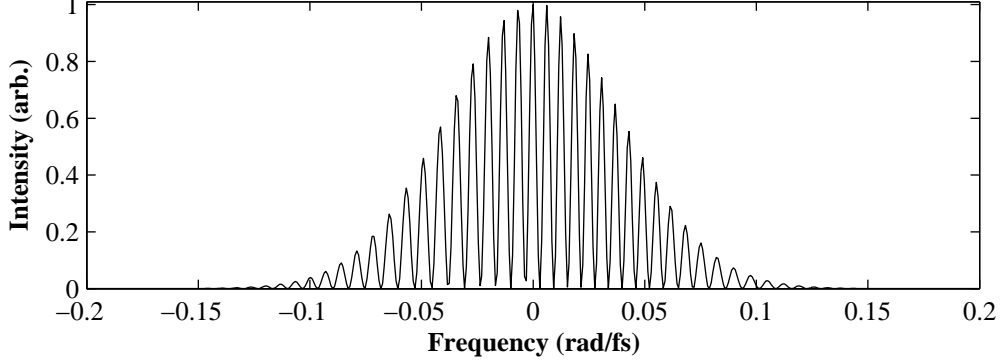
Figure 7: Sample spectral interferogram showing fringes.

Expanding the measured power spectrum:

$$
\begin{aligned}
S_0(\omega) &= (E_r + E_0) \times (E_r^* + E_0^*) \\
&= |E_r|^2 + |E_0|^2 + E_r^* E_m + E_r E_m^* \\
&= A_r^2 + A_0^2 + A_r A_0 e^{i(\phi_0 - \phi_r - \tau_0 \omega)} + A_r A_0 e^{i(-\phi_0 + \phi_r + \tau_0 \omega)} \\
&= A_r^2 + A_0^2 + 2 A_r A_0 \cos(\tau_0 \omega + \phi_r - \phi_0)
\end{aligned}
\tag{40}
$$

Following the notation in [23], we let $a(\omega) = A_r^2 + A_0^2$, $b(\omega) = 2 A_r A_0$, and $\phi(\omega) = \phi_r - \phi_0$. For a particular spectral interferogram, fringes are observed with a modulation frequency related to the time delay between the two pulses,

$$
g(\omega) = a(\omega) + b(\omega) \cos[\tau_0 \omega + \phi(\omega)],
\tag{41}
$$

where τ_0 is the temporal delay between the two interferometer arms, $a(\omega)$ and $b(\omega)$ are due to spectral intensity variations, and $\phi(\omega)$ is the phase difference between the two arms. The above can be rewritten

$$
g(\omega) = a(\omega) + c(\omega) e^{i \tau_0 \omega} + c^*(\omega) e^{i \tau_0 \omega},
\tag{42}
$$

where

$$
c(\omega) = \frac{1}{2} b(\omega) e^{i \phi(\omega)},
\tag{43}
$$

and $c^*(\omega)$ is its complex conjugate. A typical interferogram is shown in Fig. 7. Taking the Fourier transform of Eq. (42),

$$
G(t) = A(t) + C(t - \tau_0) + C^*(t + \tau_0).
\tag{44}
$$

18
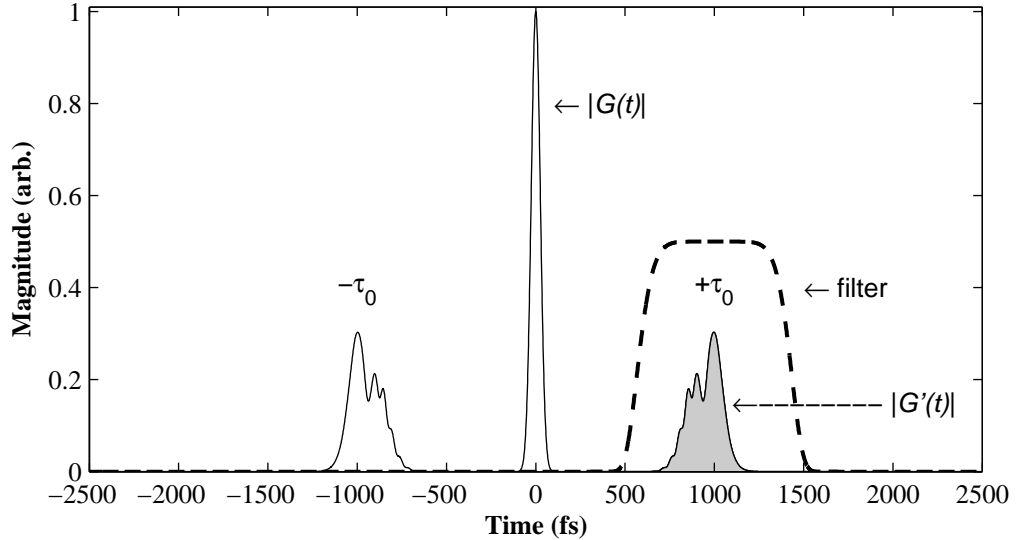
Figure 8: Typical Fourier transform of spectral interferogram.

Examining the Fourier transform of the signal, we see two peaks at $\pm\tau_0$ and a DC component caused by $A(t)$, as shown in Fig. 8. Since we are only after the phase information contained in $C(t - \tau_0)$, we multiply $G(t)$ by a super-Gaussian filter,

$$G'(t) = G(t) \times \exp\left[\frac{-(t - \tau_0)^4}{2\sigma^4}\right].$$ (45)

to obtain, with an appropriate choice of σ,

$$G'(t) \approx C(t - \tau_0).$$ (46)

An inverse Fourier transform of $C(t - \tau_0)$ yields $c(\omega)$ as defined in Eq. (43), the phase of which is the phase difference between the shaped and reference pulses. The difference in this result between a zero mask and a particular phase mask yields the spectral phase imparted by a particular SLM phase mask.

2.4.3 Results

Here we present the experimental results of the calibration method. First we find the wavelengths impinging on each pixel by sweeping a step-function phase mask that jumps from approximately 0 to π across the SLM. The resulting phase shift shows up as a discontinuity in the interferogram, which can be seen in Fig. 9. We use the derivative of each spectral component produced in the sweep, which is large at the discontinuity, to find the location of the

19
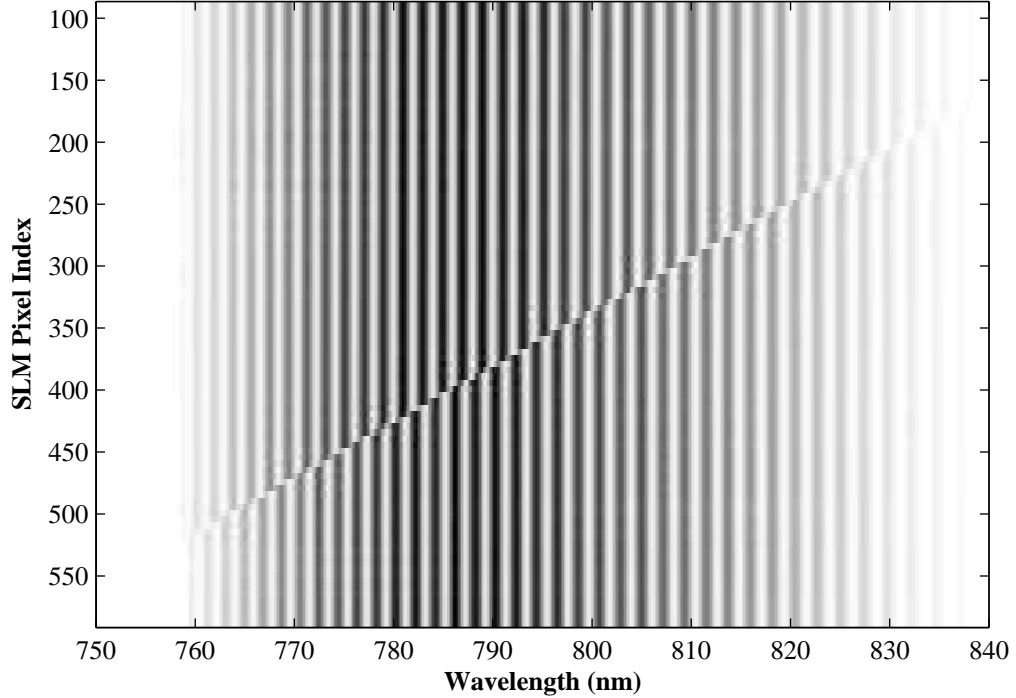
Figure 9: Interferograms showing sweep of a 0-π phase step across the SLM pixels.

step, and fit a line to this data to map SLM pixel index to wavelength. From this linear fit, we extract an experimental spectral dispersion in the Fourier plane of $\alpha \approx 157$ mm rad^{-1} fs, in close agreement with the expected theoretical value of 141 mm rad^{-1} fs, as calculated in 2.2.2.

Figure 10 shows interferograms recorded while applying an increasing drive level to all the SLM pixels, from 0 to 4095. The result is a nearly flat spectral phase applied to the shaped pulse, leading to a simple shift in the interference fringes. The reconstructed phase in Fig. 11 has the appearance of a waterfall, making it clear that the liquid crystal phase response is not linear. As a first approximation, we average this phase response across all wavelengths and fit a 5th-order polynomial to the curve. In practice we need to maintain a frequency dependence in the phase calibration. Storing a polynomial fit for each pixel of the SLM would make the mapping slow. So we split the response into strips 16 SLM pixels wide, with a 5th order polynomial fit to the average phase response across each strip. The fit is interpolated to the edges of the SLM where there is not sufficient spectral energy to
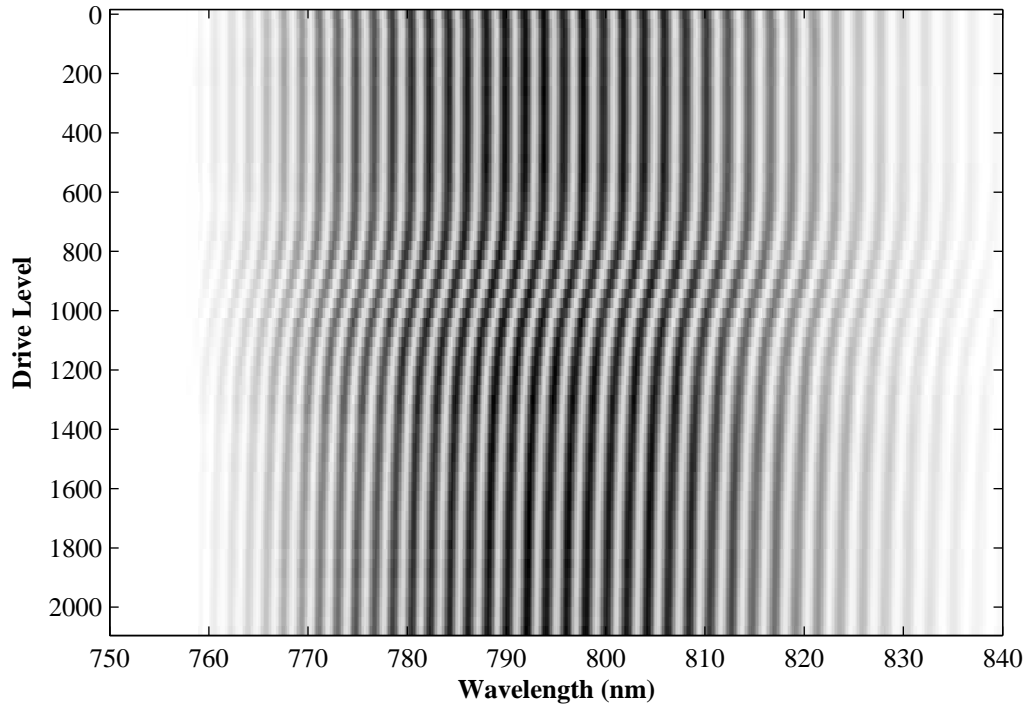
Figure 10: Interferogram fringe shifting as a phase mask of constant voltage across all pixels is swept up in voltage.
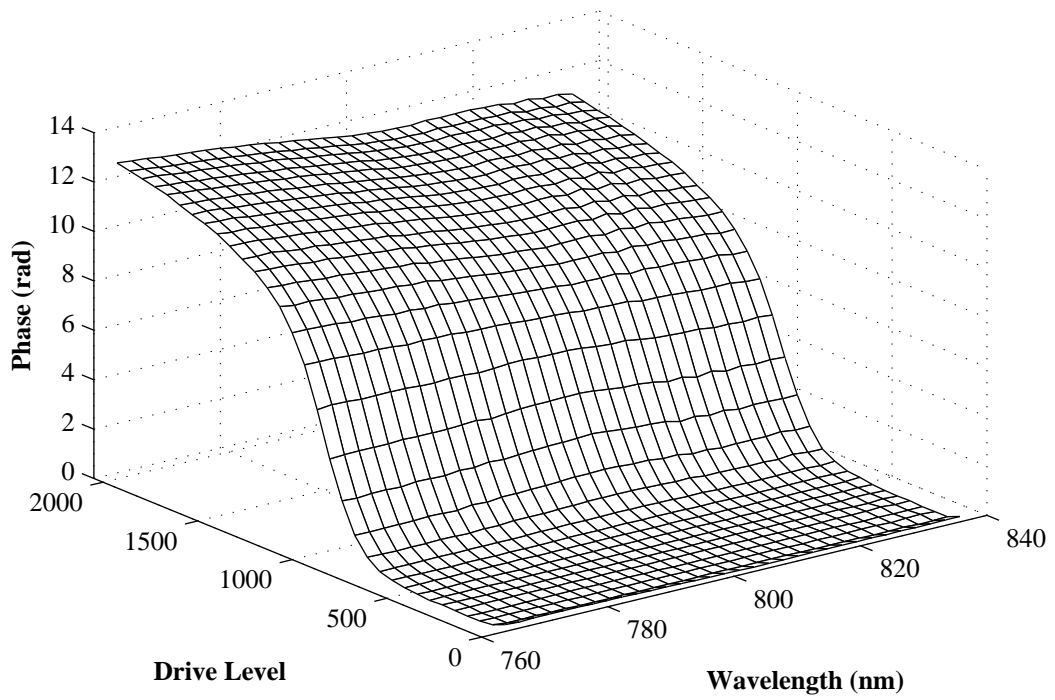
Figure 11: Wavelength- and drive voltage-dependent phase response of SLM.

21
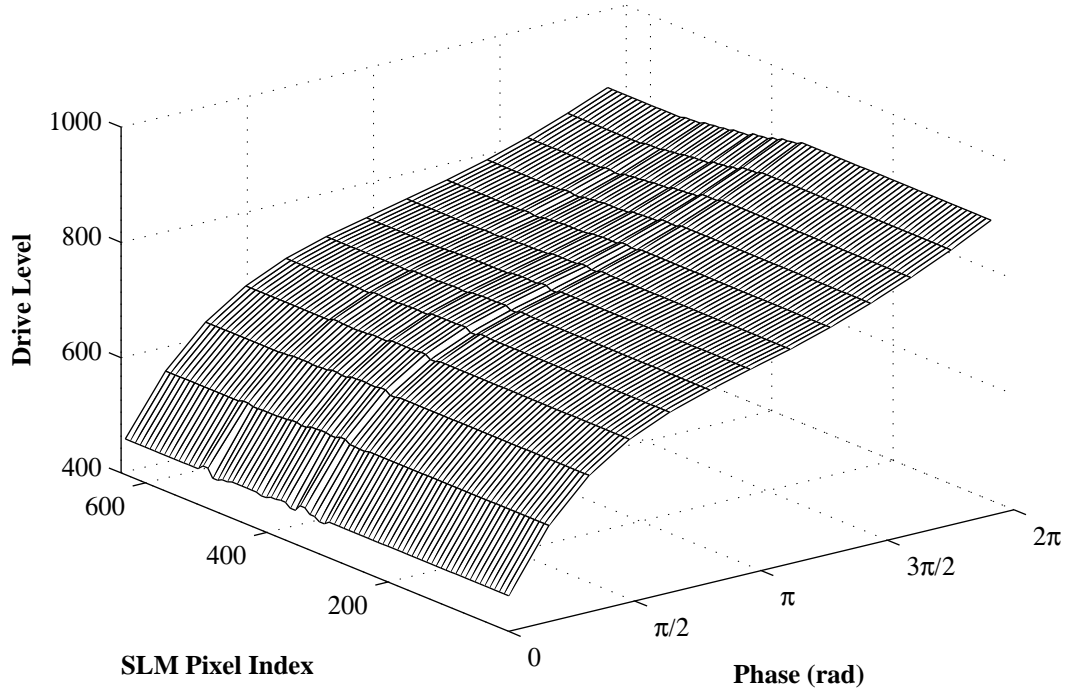
Figure 12: Final SLM phase mapping. Each fitted strip is 16 pixels wide.

attain an accurate phase calibration, as shown in Fig. 12.

2.5 Pulse Shapes

In this section we present a few pulse shapes demonstrating the capabilities of the pulse shaper. First we compress pulses by compensating for spectral phase with the pulse shaper, validating our calibration procedure. Then we apply a sinusoidal spectral phase to generate a pulse train. Finally we use the pulse shaper to create delayed pump-probe pulse pairs. We use SHG-FROG with a PCGP phase retrieval algorithm (see Appendix C) in conjunction with SI to characterize the results. As a practical matter, phases that exceed 2π must wrap back down to zero, as discussed in 4.3.2. For instance, this would convert a linear spectral phase into a sawtooth shape. The consequence of these phase discontinuities is diffraction at the wrap points, leading to undesired spectral amplitude shaping. In Chapter 3, we leverage this diffraction effect to gain control over both spectral phase and amplitude with a single phase-only LC-SLM.

The first verification of the calibration, measurement, and pulse shaper operation is

(a) Initial Spectrum/Phase   **(b) Initial Temporal Intensity**

(c) Compressed Spectrum/Phase   **(d) Compressed Temporal Intensity**
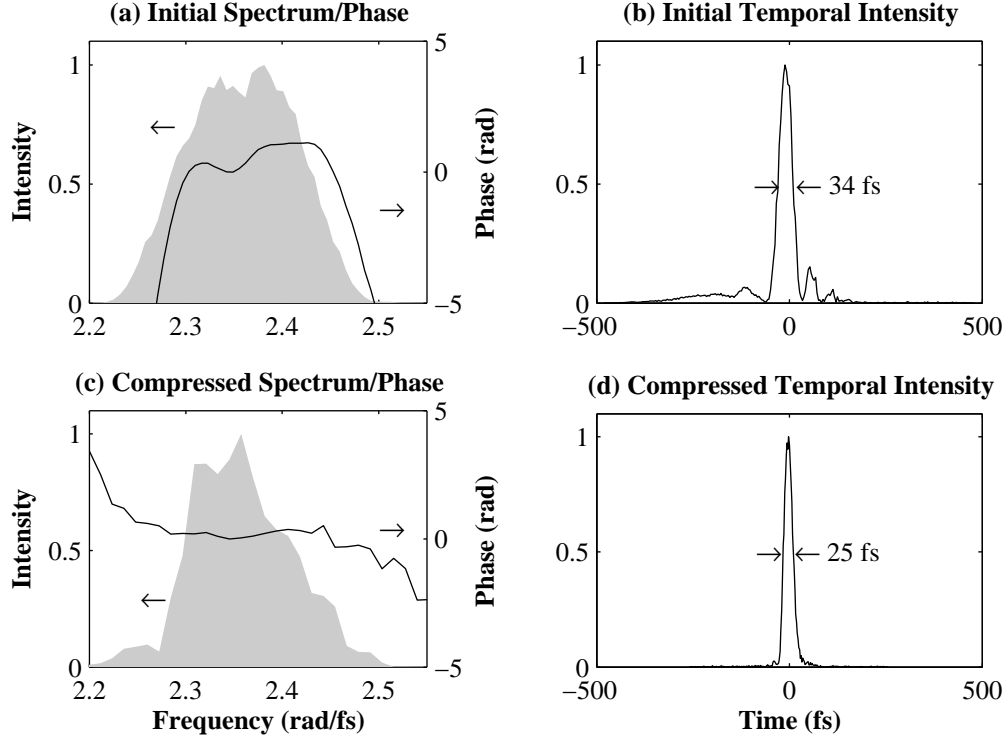
Figure 13: Pulse compression by phase inversion. (a) Initial spectrum and phase, showing some residual nonlinear phase. (b) Initial temporal intensity profile, showing energy on the wings of the pulse. (c) Compressed spectrum and flattened spectral phase. (d) Compressed pulse in time.

pulse compression by spectral phase inversion. We measure the spectral phase with SHG-FROG, invert it, and post the reconstructed phase to the SLM. In this way it compensates for residual spectral phase for which the Martinez stretcher does not compensate. The resulting compressed pulses are shown in Fig. 13 and measure to be ~ 24 fs in FWHM duration by SHG-FROG.

The next test of the phase fidelity of the pulse shaper is the application of a sinusoidal spectral phase. In the time-domain, this produces a pulse train with a spacing determined by the frequency of the sinusoid. We predict the resulting temporal pulse by numerically adding the phase to the measured spectrum of the un-shaped pulses and perform an inverse FFT. Figure 14 shows the resulting measured pulses to be in close agreement with the theory. Note the particularly close agreement in measured spectral phase (solid line) to the phase mask (dashed line) applied to the SLM. We note that the measured spectrum
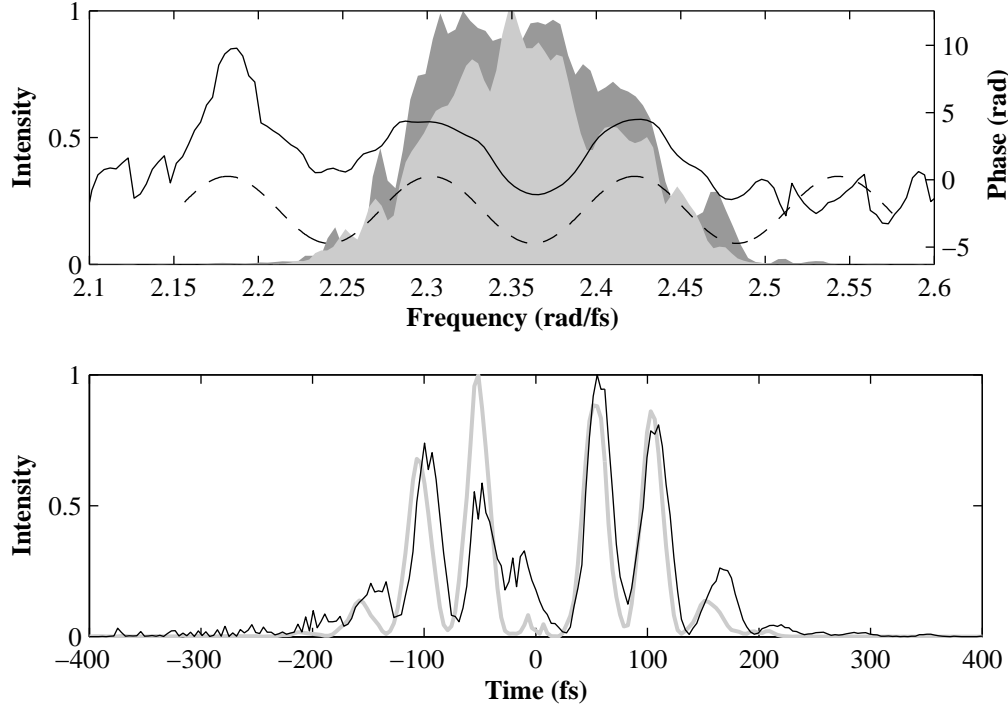
Figure 14: Sinusoidal phase modulation results. Top panel: un-shaped (dark gray patch) and shaped (light gray patch) spectral intensity profiles, applied mask (dashed line) and measured spectral phase (solid line). Bottom panel: measured temporal profile (black line) shown with theoretical profile (gray line).

of the shaped pulses differs from the un-shaped spectrum. In phase-only shaping this is an undesirable but unavoidable artifact of a pixellated SLM and discontinuous phase at 2π wrap points. Any sharp phase discontinuities at the masking plane serve to scatter light into higher-order spatial modes that are either not collected by the second half of the shaper, or are filtered out by an aperture downstream. In Chapter 3, we demonstrate an application which leverages this side-effect to gain simultaneous phase and amplitude control with a single phase-only SLM.

Finally a number of experiments were conducted to delay a small portion of the pulse by imparting a linear phase over a narrow spectral region. This generates something that could be used as a pump-probe pulse pair common to many nonlinear spectroscopy and coherent control experiments. We expect the delay to depend on the slope of the linear phase, while the duration of the probe depends on the optical bandwidth over which the linear phase was
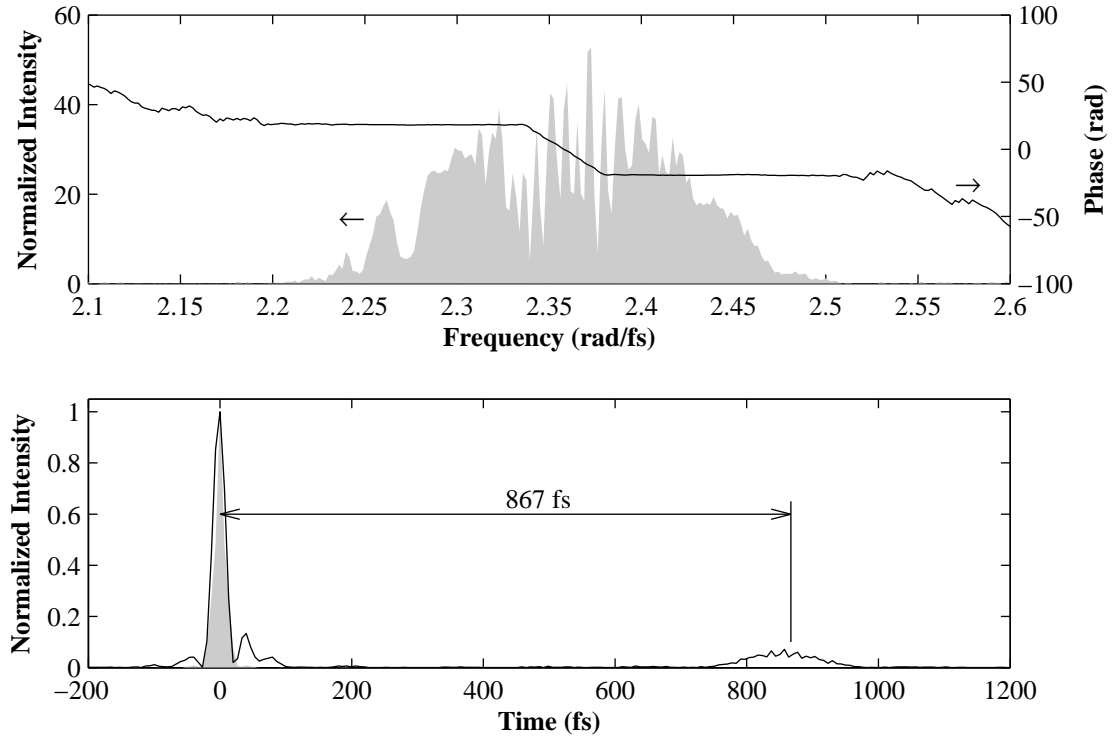
Figure 15: Pump-probe pulse pair created by applying linear spectral phase to a portion of the spectrum. Temporal intensity shown with theoretical transform-limited pulse (gray patch) for reference.

applied. More energetic and shorter probe pulses can be obtained by increasing the length of the sloped segment of the mask, while less energetic and longer pulses can be created with a narrow linear phase segment applied to the SLM. Figure 15 shows one such pump-probe pair with a delay of 867 fs, measured with SHG-FROG. The spectral modulations reflect the phase mask discontinuities at the 2π phase wrapping locations.

2.6 Summary

In the process of designing, building, and testing this pulse shaper, we have learned many lessons about this particular design. The following are a few suggestions that might improve the pulse shaper, extending its capabilities and improving its ease of configuration and use.

First, the diffraction efficiency of the gratings could be improved by minimizing the pitch of the gratings for maximum diffraction efficiency. This can be done by simply lowering the height of the gratings so that a less steep angle is used to diffract the incident light on to

the focusing optics. This is limited by the position of the folding mirrors, which will block the beam if the gratings are placed too low. To work around this, the fold mirrors could be placed as close to the gratings as possible instead of evenly between the gratings and the focusing mirrors. Of course in order to preserve the $4f$ condition, one would need to ensure the sum distance from the curved mirror to the fold mirror to the SLM is f, which means the entire apparatus would be narrower. This might be desirable if a more compact setup is required. Alternatively, one could send the incident beam in toward the grating at an angle so that it barely passes over the curved mirror. This configuration would not require any re-design of the base plate, while providing a near-normal incidence on the gratings. However, beams out of the plane of the table are generally to be avoided due to safety considerations.

Second, from our calibration data it is clear from the phase response curve in Fig. 12 that a 2π range of phases can be accessed using only a range of about 1000 SLM drive levels, while the SLM hardware has 4095 drive levels. Therefore as it is configured, we only access about one fourth of the potential phase resolution of the pulse shaper. We will work with CRi to see if if is possible to reconfigure the liquid crystal driver hardware to stretch the useful $0 - 2\pi$ phase range across all 4095 drive levels. In addition, Fig. 9 shows that most of the spectral energy of the pulses lies across pixels $240 - 480$. At the risk of losing spectral content, we might be able to increase the spectral resolution of the shaper by installing a more dispersive grating.

Finally, it turns out the pulse shaper is non-trivial to align with precision. The many degrees of freedom combined with the fact that each adjustment steers the output beam makes it difficult to determine whether any particular adjustment actually improves the alignment. For experiments requiring a good spatial mode, such as when coupling into a hollow-core fiber, shaper alignment is critical. For these reasons, a thorough alignment technique is developed in Appendix B, which ensures the two halves of the shaper are matched as closely as possible.

Chapter III

PHASE AND AMPLITUDE SHAPING WITH HIGH-RESOLUTION PHASE GRATINGS

3.1   Introduction

Many pulse shaping applications utilize spectral phase-only shaping for simplicity and low cost, as in the previous chapter. But one also needs control over amplitude to access a complete range of temporal shapes. Such control in the standard Martinez configuration has been implemented with pairs of liquid crystal spatial light modulators (SLMs) [25], volume Bragg gratings written with an acoustooptic crystal [26], and recently by a two-dimensional (2D) SLM with a blazed phase grating in the direction lacking spectral dispersion [27].

Here we introduce a new approach to phase and amplitude pulse shaping with a folded Martinez stretcher and a single, linear, high-resolution SLM. Typically, when one designs a pulse shaper employing an SLM, the spatial mode in the Fourier plane is matched to the pixel size of the SLM in order to optimize the spectral resolution, as in Chapter 2. In this chapter we investigate a shaper in which the spatial mode includes a large number of SLM pixels, effectively oversampling the spatial mode, similar to [28]. This permits spectral amplitude shaping via a high spatial-frequency sinusoidal phase grating, which spatially diffracts energy out of the mode reflected back through the shaper. Maximum throughput efficiency is attained for spectral phase-only shaping. This contrasts with 2D phase–amplitude shaping [27], where the blazed grating written onto the SLM must be carefully optimized to obtain diffraction into the output beam of the shaper, even in the absence of spectral amplitude shaping.

3.1.1   Setup

We demonstrate the efficacy of this technique with two implementations of the pulse shaper, shown in Fig. 16: one with a prism for low angular dispersion, the other with a grating
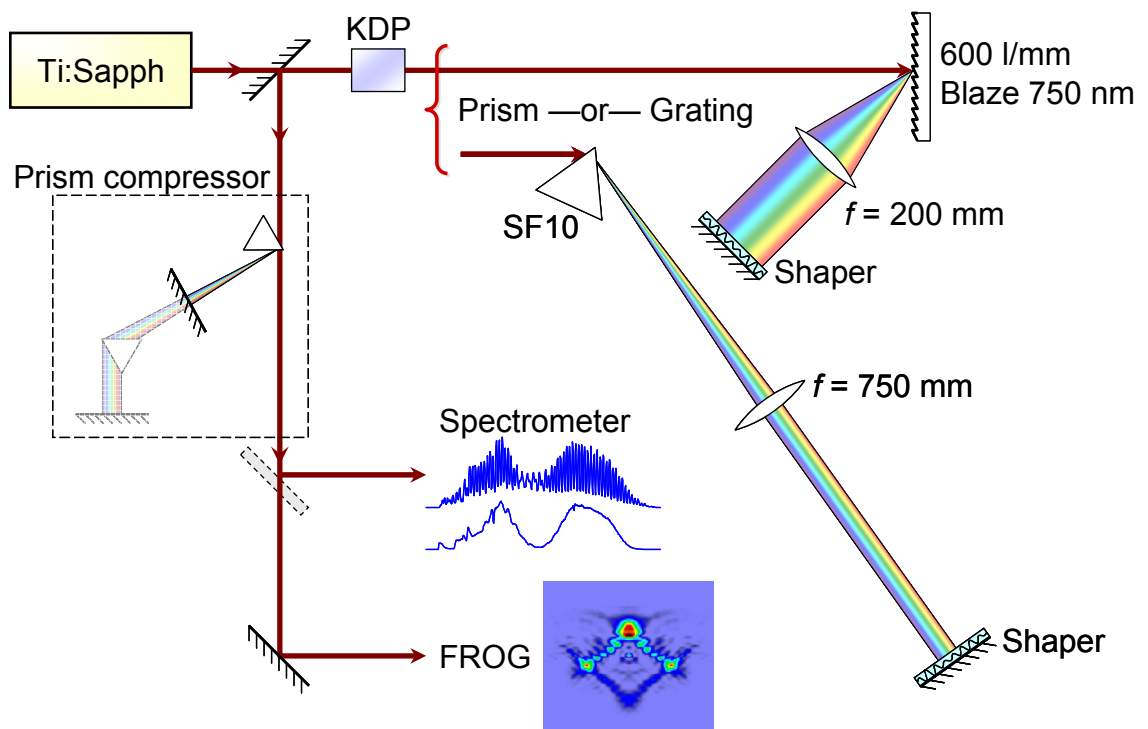
Figure 16: Layout of phase and amplitude shaper experimental setup. Credit: Philip Schlup.

for high angular dispersion. In both cases, the dispersive element is placed at the front focal plane of a convex lens and the reflective SLM is placed at the back focal plane. The phase mask we use is a 1×12,288 Linear Series spatial light modulator provided by Boulder Nonlinear Systems (Lafayette, CO). The liquid crystal elements are each 1.0 μm wide, with a 0.6 μm interpixel gap. The beam from a Ti:sapphire oscillator (KM Labs), with 40 nm optical bandwidth centered at 790 nm, was collimated to $2w_{\text{in}} \approx 4$ mm diameter and sent into the shaper. For the prism implementation, we used a 750 mm focal length lens and an SF10 Brewster prism. The spectral focus is 188 pixels wide. In the grating version, a 600 groove/mm grating is used with a 200 mm focal length lens. The spectral focus is 47 pixels wide, leaving about 260 independent spectral control points. The SLM reflectivity is 93% and the total shaper efficiencies are 77% and 35% for the prism and grating shapers, respectively, although higher throughputs should be possible with a grating optimized for efficiency. For convenience, a single-prism pulse compressor [29] is placed after the pulse shaper to compensate for the second-order dispersion of the non-transform-limited incident pulses. To characterize the pulse shaper, we use a spectral interferometry (SI) technique described in Chapter 2. Temporal pulse measurements in this paper were performed with a second harmonic generation frequency resolved optical gating (SHG-FROG) device [30], making use of a high-speed principle component generalized projection (PCGP) phase retrieval algorithm [31] as described in Appendix C.

3.1.2 Simultaneous Phase and Amplitude Shaping

To understand this approach mathematically, we employ notation for pulse shaper analysis following Ref. [16]. We begin with a pulse incident on the device, restricting ourselves to a Gaussian mode in one spatial dimension x:

$$E_{\text{in}}(x,t) = E_0 \exp\left[-(x/w_{\text{in}})^2\right] u_{\text{in}}(t), \tag{47}$$

where E_0 is the initial amplitude, w_{in} is the $1/e^2$ radius of the beam, and $u_{\text{in}}(t)$ is the oscillatory temporal field. The focused field at the Fourier plane, where we place the phase mask, is related to E_{in} by the Fourier transform and is represented by

$$E_{m-}(x,\omega) = E_{\text{in}}(\omega)e^{-(x-\alpha\omega)^2/w_0^2}. \tag{48}$$

Here $\alpha = dx/d\omega$, which is set by the angular dispersion and the focal length of the Martinez stretcher. $E_{\text{in}}(\omega)$ is the Fourier transform of the incident pulse $E_{\text{in}}(t)$, and w_0 the $1/e^2$ intensity radius of the focused beam at the Fourier plane. The pulse just after the masking plane is

$$E_{m+} = E_{\text{in}}(\omega)e^{(x-\alpha\omega)^2/w_0^2}M(x). \tag{49}$$

We apply a high-resolution phase-only mask, with periodic structure faster than w_0:

$$M(x) = \exp\left[i\Delta(x)\sin(2\pi f_g x) + i\phi(x)\right]. \tag{50}$$

The mask is a superposition of a sinusoidal phase grating with spatial frequency $f_g > w_0^{-1}$ and depth of modulation Δ, and a slow additional phase ϕ. The grating depth can vary from $\Delta = 0$ for full transmissivity to $\Delta \approx 2.4$ (the first zero of the zero-order Bessel function J_0) for full extinction.

We turn our attention to the phase grating component of the mask:

$$t(x) = \exp\left[i\Delta(x)\sin(2\pi f_g x_{\text{fp}})\right]. \tag{51}$$

Expanding this sinusoidal phase into a series of Bessel functions,

$$t(x) = \sum_{m=-\infty}^{\infty} J_m\left[\Delta(x)\right]\exp\left(i2\pi m f_g x\right), \tag{52}$$

where m describes the scattering order of the phase grating, we find that if f_g is sufficiently high, the shaper optics only collect the zero order and convert the phase grating to amplitude control:

$$t(x) \approx J_0\left[\Delta(x)\right]. \tag{53}$$

Now we have an effective mask of

$$M(x) \approx J_0\left[\Delta(x)\right]\exp\left[i\phi(x)\right]. \tag{54}$$

From this result, we expect full spectral amplitude control from a high frequency sinusoidal phase grating, by adjusting $\Delta(x)$ to modulate spatial diffraction across the spectrum dispersed in the Fourier plane. Spectral phase control is imparted by adding the appropriate slow phase value $\phi(x)$.
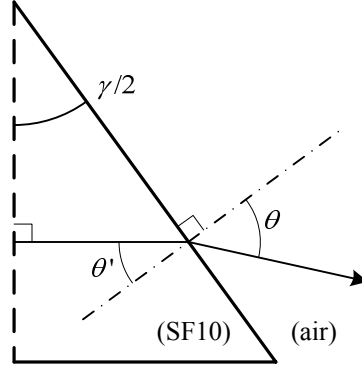
Figure 17: Half-prism diagram with angles for deriving angular dispersion.

Equation (54) is only valid if the pulse shaper optics only collect the zero-order light scattered from the grating. In practice, this spatial filtering condition is met by the experimental apparatus following the shaper, e.g., optical fibers, pulse measurement devices, apertures, etc. [16]

3.1.3   Angular Dispersion

Here we derive the angular dispersion relationship for the prism shaper, determining the mapping of frequency to spatial position at the Fourier plane, $\alpha = dx/d\omega$. For details on angular dispersion in a grating shaper, see Chapter 2.

In the prism case, the angular dispersion is governed by refraction. Here we use a Brewster-cut prism placed for minimum deviation of the beam. The prism has a wavelength-dependent refractive index $n(\lambda)$, is surrounded in air ($n_{\mathrm{air}} = 1$), and has an apex angle of γ. In the following discussion, all angles are measured from the surface normal. As an approximation, we will derive the angular dispersion of half of a prism (Fig. 17), and then double that result to obtain the angular dispersion of a full prism. The minimum deviation condition implies that the beam inside the prism is perpendicular to the centerline at the center wavelength λ_0, fixing θ' as a constant with respect to λ.

We start by applying Snell's law at the interface:

$$\sin \theta = n \sin \theta' \tag{55}$$

31

Evaluating the first derivative of both sides yields

$$\cos\theta \frac{d\theta}{dn} = \sin\theta' + n\cos\theta' \frac{d\theta'}{dn}. \tag{56}$$

Recognizing that $d\theta'/dn = 0$ and substituting Eq. (55), we find

$$\frac{d\theta}{dn} = \frac{1}{n}\tan\theta. \tag{57}$$

The Brewster condition requires that $\tan\theta \approx n(\lambda_0)$, reducing Eq. (57) to

$$\frac{d\theta}{dn} = 1. \tag{58}$$

Therefore the wavelength-dependent angular dispersion for a half-prism is

$$\frac{d\theta}{d\lambda} = \frac{d\theta}{dn} \times \frac{dn}{d\lambda} = \frac{dn}{d\lambda}. \tag{59}$$

From the Sellmeier equations for SF10, $dn/d\lambda = -0.0534 \ \mu m^{-1}$ at 780 nm. As with the grating case in Chapter 2, we make use of Eq. (11) and make the conversion to angular frequency. The result for the full two halves of the prism combined is

$$\frac{dx}{d\omega} = \frac{-\lambda_0^2}{2\pi c} \times \frac{dx}{d\lambda}. \tag{60}$$

Finally for our prism-based shaper we conclude that $\alpha \approx 26$ mm rad^{-1} fs. For the grating shaper, this parameter works out to be $\alpha \approx 44$ mm rad^{-1} fs.

3.2   Calibration

3.2.1   Phase Calibration

To calibrate the device we first find the relationship between pixel and frequency by sweeping a π–step across the SLM and observing the dip in the transmitted spectrum due to the phase discontinuity. From these data, we empirically estimate $\alpha \approx 28$ mm rad^{-1} fs for the prism shaper, and $\alpha \approx 44$ mm rad^{-1} fs for the grating shaper; both agree well with theory.

Next, we make use of the inline SI technique [32] as described in Section 2.4, where a birefringent crystal splits the input pulse into two time delayed pulses with orthogonal polarizations. The SLM only shapes one of the polarizations, leaving the second as a reference. The two pulses are projected to the same polarization using a polarizer at 45° and

the resulting SI fringes are measured with a spectrometer (OceanOptics). Here the phase difference between the pulses is very stable, leading to more reliable phase measurements than by placing the shaper in a Mach-Zehnder interferometer, as described in Chapter 2. We then extract the phase difference with a sideband filtering technique [23].

We calibrate the drive voltage to phase by running all the SLM pixels through their drive range, measuring interference fringes, and computing the resulting imparted phase. For this particular SLM, we make use of the drive range $V = (128 \to 256)$, which yields approximately a 2π range of phase at 800 nm. Figure 18(a) shows this calibration for the prism shaper; results are similar for the grating case. The calibration is verified in Fig. 18(b) by the close agreement between target (gray line) and measured (black) phases. From this information, we generate a functional mapping f that converts a mask of requested phase ϕ at a particular frequency ω to a drive level v for each pixel i,

$$v_i \xleftarrow{\;f\;} \phi(\omega_i). \tag{61}$$

The phase response is split into strips 192 pixels wide to maintain some frequency dependence, just as described in Chapter 2.

3.2.2 Amplitude Shaping Calibration

Armed with a reliable phase calibration, we characterized the amplitude control afforded by our technique. Applying a range of phase gratings, we established an optimal $f_g = 27\ \mathrm{mm}^{-1}$ for the prism-based shaper, and $f_g = 60\ \mathrm{mm}^{-1}$ for the grating-based shaper. We find that for both setups the optimal phase grating period is approximately $2w/5$. The spatial frequency was high enough that the grating diffracted light outside of the aperture of the apparatus, yet low enough that the discrete SLM pixels adequately sample the sinusoid.

We measure transmission T as the ratio of shaped/unshaped spectral intensity at 780 nm, observed at the shaper output. Fig. 18(c) shows T for the 62-μm period sinusoidal phase grating on the prism-based shaper, varying Δ. The curve agrees very favorably with the $|J_0(\Delta)|^2$ dependence predicted theoretically. In Fig. 18(d), we post a phase grating of increasing width to the SLM and record spectra of the resulting pulses. The plot shows the relative reflected intensity recorded by the spectrometer at a wavelength of 790 nm. As

expected, the transmission plateaus once the width phase grating is of order of the spatial mode size in the Fourier plane.

3.2.3 Verification

The above calibration allows the generation of arbitrary pulse shapes with specified amplitude and phase. For best results, we first remove the residual spectral phase distortion present after the prism compressor. To accomplish this, we measure a FROG trace with the mask set to constant zero phase, and retrieve the phase with the PCGP algorithm. The inverted phase is added to the shaper mask to obtain near-transform-limited 28 fs pulses, verified by another FROG measurement. This pulse compression verifies the accuracy of both our calibration and pulse measurement techniques.

3.3 Pulse Shapes

We demonstrate the phase shaping capabilities of the pulse shaper, independent of amplitude, by applying a V-shaped spectral phase. The halves of the spectrum see a linear phase with slope τ, with opposite signs on each half. The effect is to split the pulse into a pair, delayed by 2τ. Results for $2\tau = 400$ fs are shown in Fig. 19.

Amplitude-only shaping here is shown by producing a square spectrum shown in Fig. 20(a). The mask attenuates frequencies outside the desired square, and is set to nearly flatten the top of the spectrum. The inverse Fourier transform of a square spectrum is a sinc function. The intensity profile of such a pulse is a sinc^2, with alternating π phase as shown in Fig. 20(b).

Finally to demonstrate simultaneous control over spectral phase and amplitude, we shape the spectrum into two lobes separated by 0.08 rad/fs and vary their relative phase ϕ as shown in the inset in Fig. 21. The spectral lobes interfere in the time-domain in a manner analogous to a double-slit experiment. The resulting pulse shape intensity profile lies within a region identified in Fig. 21 with a gray Gaussian envelope, shown as a visual guide; the intensity modulation period is set by the splitting of the spectral peaks and agrees with the expected ~ 80 fs period. In analogy with Young's double slit experiment, the intensity

interference structure shifts in the expected manner with the application of a relative phase between the two spectral lobes.

3.4   Summary

In summary, we have demonstrated simultaneous amplitude and phase control of ultrafast laser pulses using a single linear SLM. The amplitude shaping was made possible by over-sampling each spectral focus and writing a phase grating with sufficiently high frequency. The close pixel spacing, large number of pixels, and small footprint of the SLM used here enables this simple and compact design. Moreover, the high reflectivity of the SLM also results in a highly efficient pulse shaper when a prism is used for the angular dispersive element. This pulse shaper design is anticipated to find wide-spread use due to the low cost, high efficiency, and compactness with amplitude and phase shaping capability.
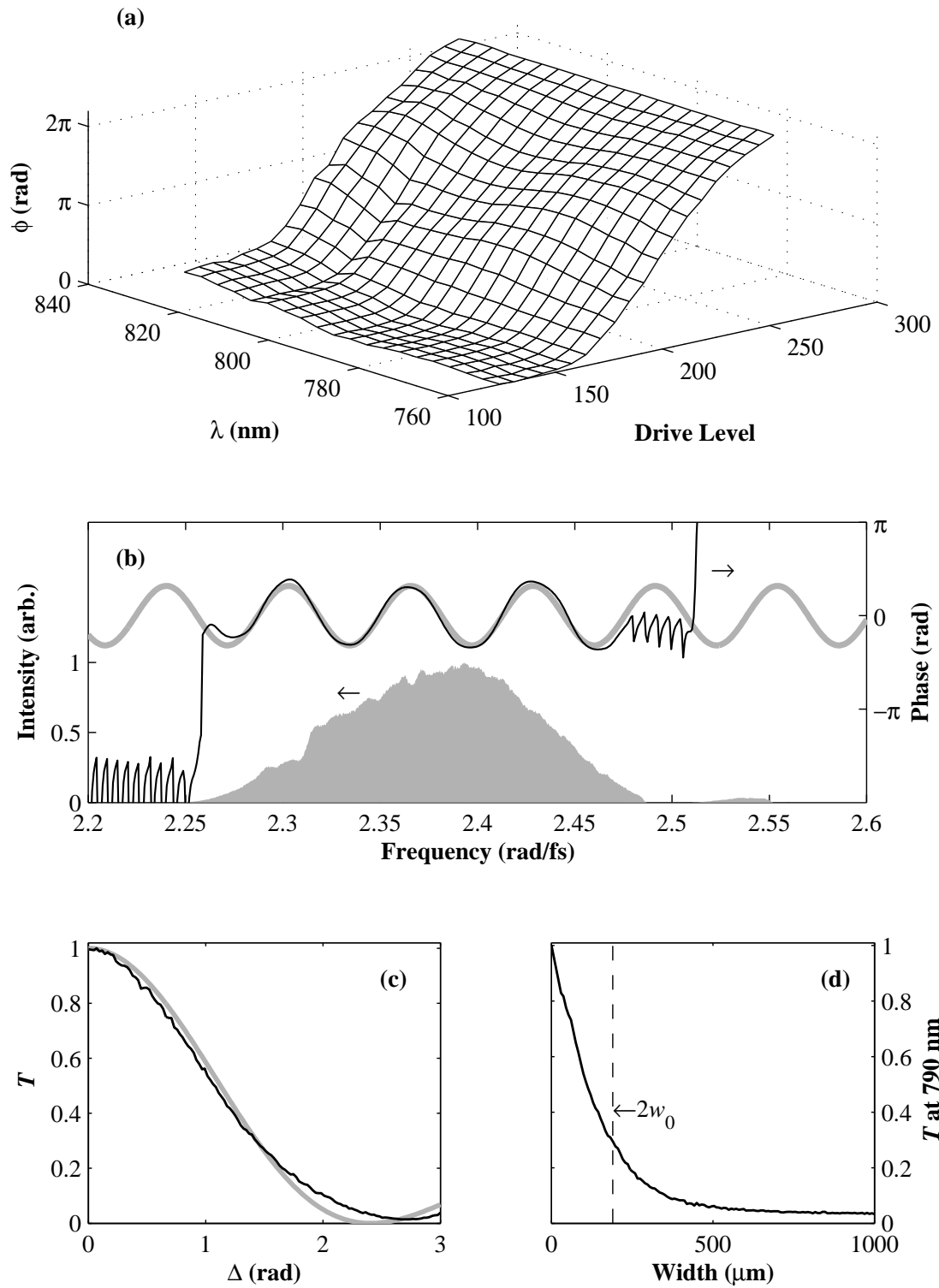
Figure 18: (a) Calibration of phase ϕ with respect to wavelength and drive level. (b) Phase calibration check. (c) Transmission T with respect to the phase grating depth. (d) Transmission, varying the width of the phase grating.

36
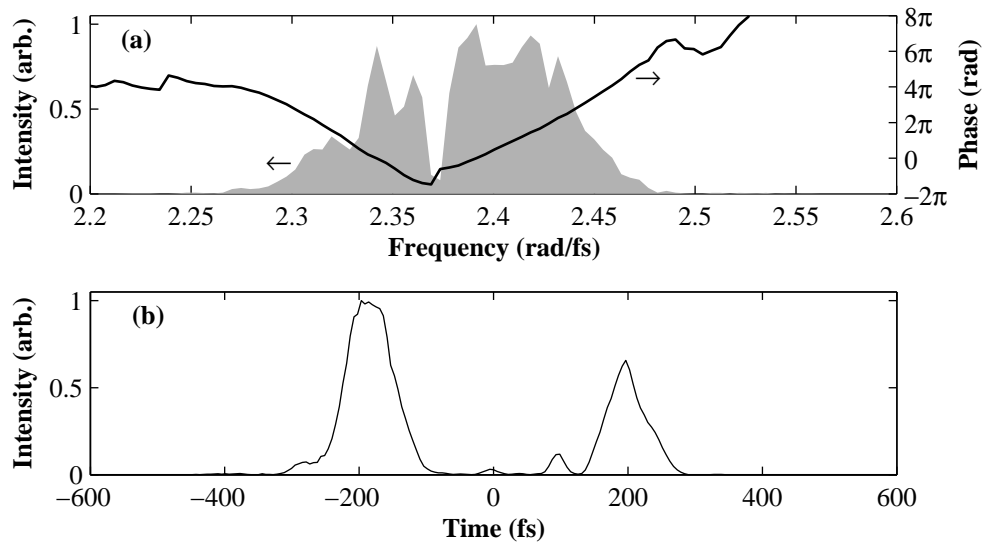
Figure 19: Prism shaper phase demonstration. (a) Spectral intensity and phase for splitting a pulse into a delayed pair. (b) Temporal intensity, showing separation of 400 fs.
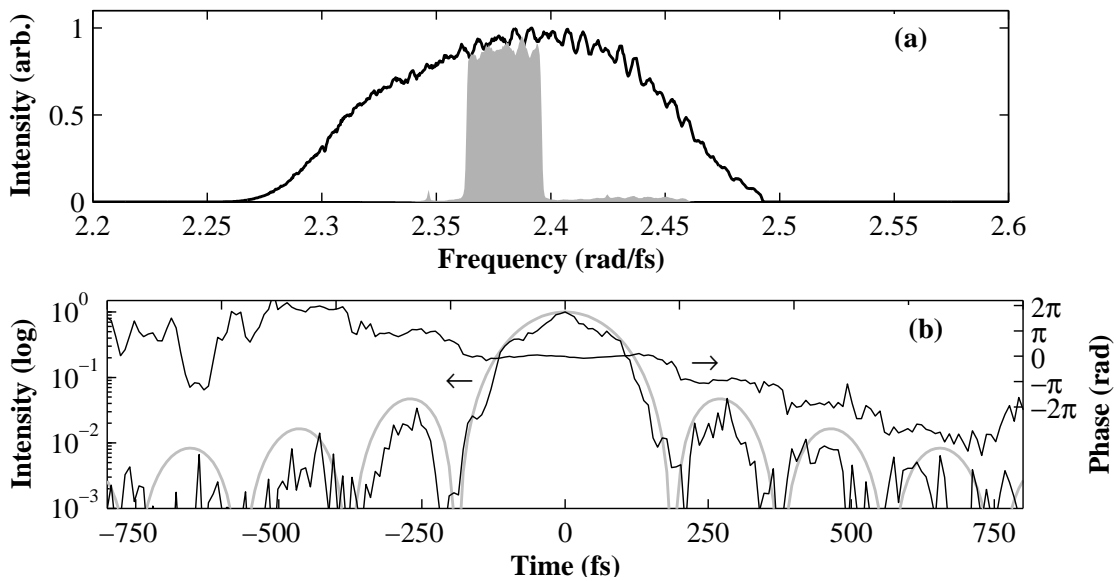
Figure 20: Amplitude-only shaping with the prism shaper. (a) Unshaped and shaped square spectrum. (b) Resulting temporal profile (black line), with a sinc^2 (gray line) for comparison.
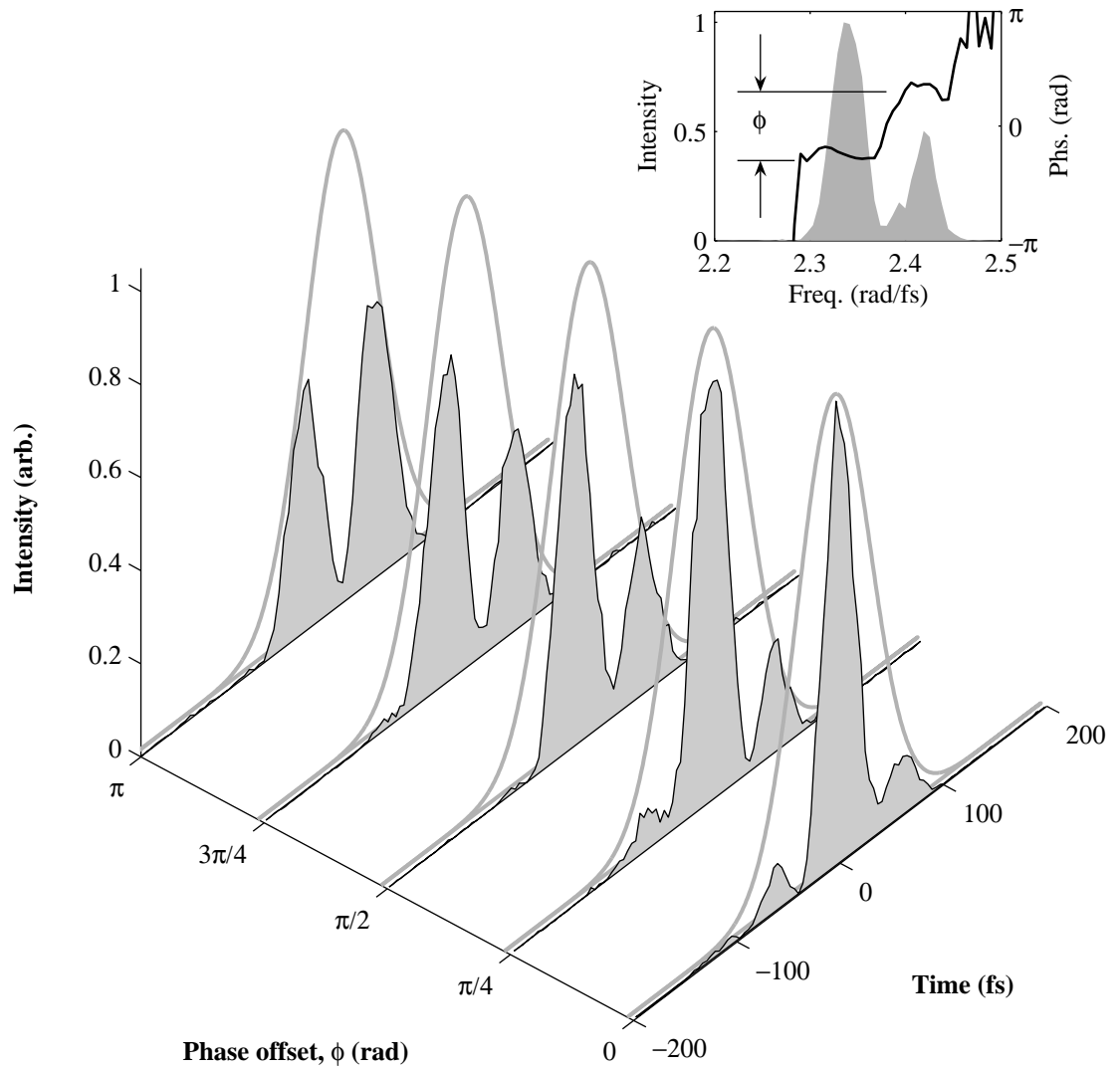
Figure 21: Temporal profiles for the spectral double-slit experiment with the grating shaper. Inset: pulse spectrum and phase.

Chapter IV

CONTROL EXPERIMENT: PULSE COMPRESSION

4.1 Background and Introduction to Closed-Loop Control

With the advent of pulse shaping, the goal of manipulating quantum and molecular systems with laser pulses was in sight. Theoretical investigations into the effects of shaped pulses of light on these systems progressed, but experimental work was at an impasse [1]. In order to design a pulse shape to achieve a desired outcome, full knowledge of the system's Hamiltonian would be required, which is not possible except for exceedingly simple systems. In 1992, Judson and Rabitz [9] recognized these difficulties and proposed a novel technique for designing control fields. They proposed integrating the pulse shaper and experimental apparatus into a closed-loop control system. By abstracting the pulse shaper and experimental apparatus as a 'black box' with inputs to control the SLM, while the outputs report on the influence of the control signal on the experimental outcome, a search algorithm can be attached that seeks the required pulse shape to produce a desired experimental outcome. As Rabitz is fond of saying, we no longer need to simulate the quantum system, because we can use the quantum system itself as an 'analog computer' that solves the Schrödinger equation in real time and instantly reports the influence of any applied control field. Furthermore, the pulse shapes found by the algorithm can be analyzed to provide insight into the physics of the system being controlled. Now the search algorithm becomes the most crucial element.

4.2 Search Space and Algorithm Selection

Decades of intensive work in the fields of computer science and artificial intelligence have led to a plethora of search algorithms to choose from. As any textbook on optimization will explain, common to all these algorithms is the concept of a fitness function or an objective function [33]. As in the child's game of hot and cold, the one performing the

search must have a metric to determine whether his or her steps are coming closer to or leading further away from a solution. The difference between a fitness function and a cost function is trivial; the former we attempt to maximize, the latter we attempt to minimize. An algorithm designed to minimize a cost function can still maximize a function if it is inverted first. For example, if we wish to find a pulse shape which maximized the yield of a chemical reaction, we construct a detector that responds to the desired product, and use the output of the detector as a fitness function which the algorithm seeks to maximize.

The selection of an algorithm depends on the nature of the search space involved [33]. Simple hill climbing algorithms do well with topographies that have a single global maximum, but are easily fooled by local maxima. Stochastic methods such as simulated annealing work around this problem by introducing a random chance of walking down a hill to find a better one. The high-dimensional search spaces characteristic of coherent control experiments require a search algorithm that must be able to rapidly sample a large landscape in order to find a global maximum. With our 640-pixel SLM for example, the search space is a grid of 640 dimensions each with 4095 points to sample, leaving 4095^{640} or about 1×10^{1058} unique points to sample. Allowing 100 milliseconds to perform an experiment to find the fitness function of a point, it would take about 4×10^{1040} billion years to explore the entire landscape! For such a problem, we use an evolutionary strategy [34]. The evolutionary algorithm commonly used in coherent control experiments begins by sampling a number of random points in the search space and ranking those points according to their fitness score. The best are selected, and a number of random points near them are selected for exploration. In this way we continue narrowing the search space until a good solution is found.

Another intuitive way of thinking about evolutionary algorithms is in Darwinian terms of a population of living organisms. Any unique point in the search space can be represented by a 'chromosome'. A set of random chromosomes is generated to produce an initial population. Each member of the population is then tested and assigned a fitness score. The best performers become the parents of the next generation, while the algorithm discards the poor performers. The algorithm creates each subsequent generation by mutating parent

chromosomes. From there the process repeats itself, with each generation progressively refined from the previous.

In our experience with coherent control problems, these algorithms reasonably converge within hundreds or thousands of fitness function trials, or tens of generations. This means we can find reasonable solutions within minutes, instead of eons, once the apparatus is operational. The data from a convergence run of an evolutionary algorithm can be collected and analyzed to lend insight into the underlying physics of the system [35] and answer questions about search space topography. Some theoretical work has been performed on characterizing the search space by Rabitz *et al.* [36]. The authors propose a quantum mechanical argument that there are no local maxima, that any peak or plateau in the landscape *must* be an optimal solution, though many may exist. What remains is the question of robustness, which is linked to the width of the peak. This leads to another advantage of the evolutionary strategies. Since the solutions are developed in real, noisy, imperfect laboratory environments, the solutions are naturally robust. Unstable solutions may be found, but will not be able to survive for many generations, and will be naturally discarded by the algorithm.

4.3   *Implementation of an Evolutionary Strategy*

In high-dimensional search spaces, general evolutionary strategy (ES) algorithms struggle with convergence when the search entropy (or step size) σ is the same for all degrees of freedom. Typically the search begins with a large σ, which decreases a small amount per iteration; this approach is known as *annealing*. The problem is that if, early on, a member of the population has a value in a certain dimension close to the solution, the next step with a large σ will be likely undesirable. By lowering σ, the next step will retain a value close to the solution in that particular dimension, but if the values on other dimensions are far off, they will be slow to converge. A better strategy exists, known as a covariance matrix adaptation evolutionary strategy (CMA-ES) [37]. In CMA-ES, each dimension i has its own step size σ_i. Not only are the population values adapted, but, as will be shown, the step sizes are also cleverly chosen to speed the search along. For maximum flexibility,

a CMA-ES algorithm has been developed in MATLAB, based on an excellent tutorial and sample code by Hansen [38].

4.3.1 CMA-ES Formalism

Using the standard notation, we describe our algorithm as a (μ, λ)–ES, where μ represents the parent population, and λ the offspring.

To develop a description of the algorithm, we begin by describing a simple search problem of one variable, x. We seek a value for x that optimizes a fitness function $f(x)$. A standard (μ, λ)–ES will begin with an initial random population $(x_1, x_2, \ldots x_\lambda)$ with λ individual members. One method for generating these random guesses is by use of a normal distribution with standard deviation (step size) σ and mean x_0 defined as $\mathcal{N}(x_0, \sigma) = x_0 + \mathcal{N}(0, \sigma)$. In practice, the initial σ and x_0 are chosen to yield an adequate sampling of the search space. For example, for topographies with few global optima and many local 'false' optima, a large initial σ will encourage adequate sampling, preventing the search from falling into the trap of a local solution. x_0 is chosen as a good initial guess, e.g., a chromosome which yields transform-limited control pulses.

With this initial guess in place, the algorithm evaluates $f(x_i)$ for all members of the population, and sorts the members by their relative performance. There are many mechanisms available for generating the parent population for the next iteration, but we simply select the top μ performers. To create the next generation, we use only the mutation operator. A new chromosome x' is generated from a parent chromosome x by $x' = x + \mathcal{N}(0, \sigma)$. Since the old x was one of the top performers, using it as the mean for the normal distribution that generates offspring will tend to move the population in the direction of an optimal solution. As mentioned above, a good choice for σ will depend on the characteristics of the search space and the present population. For instance, if the optimal solution is near the present population, we want a small σ. When seeking a global optimum, one typically starts with a large σ and decreases its value with each iteration according to $\sigma' = \tau \cdot \sigma$ where $\tau < 1$ is a decay constant that determines how quickly to anneal the population.

The above approach works well for single- and low-dimensional searches. But as we

increase the number of variables to optimize, it becomes difficult to find a good choice for σ. If σ is too small, the search takes small steps per generation and takes a long time to reach an optimal solution. If σ is too big, the population tends to jump around, oscillating about an optimal solution. The CMA-ES technique uses the multivariate normal distribution to generate the next population set, $x = \mathcal{N}(0, \mathbf{C})$, where $\mathbf{C}$ is the *covariance matrix*. This covariance matrix is adapted along with the population as the algorithm progresses, optimizing the search parameters in addition to the population. The details of this technique are beyond the scope of this thesis and can be found in [37, 38].

4.3.2 Chromosome Representations

Originally in genetic algorithms, a chromosome was a binary bit string that contained all the information necessary to represent a point in the search space. Evolutionary strategies are flexible in that a chromosome can be any representation that maps to such a point. In the software developed here, this can be any representation that can be mapped to the 640 pixel elements of the SLM. The most obvious and simple chromosome format is a 640-element integer array that can contain values ranging from 0 to 4095, but as shown earlier, this leads to a rather large search space. Simplified representations can be of a lower dimension yet can provide adequate coverage when mapped to the full search space. One easy simplification, the linear piecewise representation, reduces the number of dimensions by only keeping track of a small number of evenly spaced points, interpolating in between in a linear fashion. Such a representation can be improved upon by using smoother interpolation between points, such as splines. Chromosomes can also be constructed from a set of basis functions. For example, a polynomial basis makes intuitive sense for pulse compression experiments where the material dispersion we seek to compensate for is primarily quadratic. In practice, we have found the spline representation to be the most fruitful.

In creating these phase mask representations, a few physical concerns peculiar to our shaper ought to be considered. First of all, smooth masks are desirable. Any sudden changes in the phase of adjacent pixels on the mask act to diffract the beam, scattering power and distorting the spatial mode quality. Second, the maximum phase any individual pixel can

Initial Pulse   **Glass**   **Pulse After Propagation**

$$E(0,t) = e^{-a_0 t^2 - i\omega_0 t}$$ $$E(z,\omega) = E(0,\omega)e^{i \cdot k(\omega) \cdot z}$$ $$E(z,t) = e^{-a(z)t^2 - i\omega_0 t}e^{i\phi(z,t)}$$
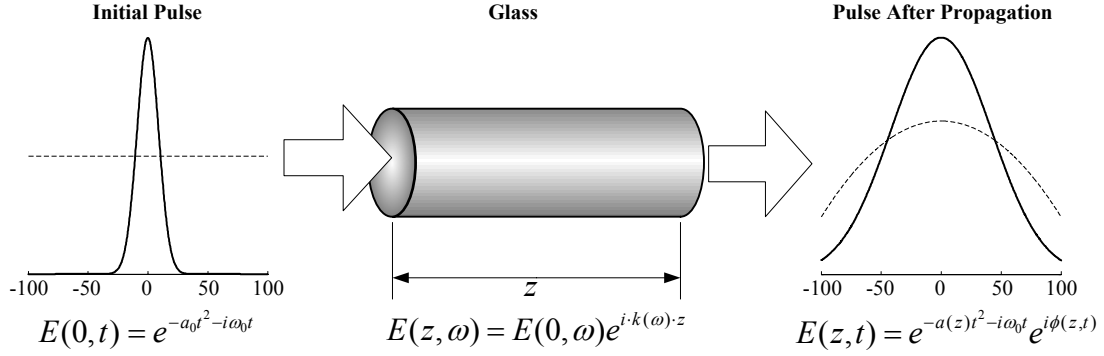
Figure 22: A short pulse propagating through a length of dispersive glass accumulates a primarily quadratic spectral phase, and ends up stretched in time afterwards.

delay a frequency component by is approximately 3π in our shaper. Greater phase shifts are often desired between frequency components, so a phase wrapping technique has been implemented. Since by nature one can add any multiple of 2π to a phase without physically altering the phase, $\phi = \phi + 2\pi \cdot n$, we wrap the phases according to:

$$\phi_{\text{wrapped}} = \texttt{mod}\,(\phi, 2\pi)\,, \tag{62}$$

At the cost of some spectral attenuation at the wrap points, this opens up a much wider range of phases, provided that no two adjacent pixels have a phase difference greater than π. Since these are physical constraints caused by the SLM, the phase mask is wrapped at 2π before being posted to the SLM, independent of the chromosome representation.

4.4 Experiment: Introduction

One primitive implementation of a coherent control experiment is to compress an ultrafast pulse. When a short pulse propagates through a dispersive medium, such as glass, the variation in refractive index with respect to frequency causes the various frequency components of a pulse to travel at different phase velocities, resulting in a temporally stretched, or chirped, pulse (see Fig. 22) [19]. We illustrate this by describing the real electric field of a pulse with a central frequency of ω_0 as a linear superposition of individual frequency components:

$$E(z,t) = \frac{1}{2\pi} \int \frac{1}{2} E(z,\Omega)e^{i\omega t} d\omega + \text{c.c.}, \tag{63}$$

44

where $\Omega = \omega - \omega_0$ and c.c. denotes the complex conjugate. For low intensities, propagation through a lossless dispersive medium is easily modeled in the frequency domain:

$$E(z, \Omega) = E_0(\Omega)e^{ik(\omega)z}, \qquad (64)$$

where the input pulse spectrum is defined in terms of an envelope A and a phase ϕ,

$$E_0(\Omega) = A(\Omega)e^{i\phi(\Omega)}. \qquad (65)$$

The phase response of the material is described by $k(\omega) = n(\omega) \cdot \omega/c$. For a large number of materials, n is well characterized, and expressed by a familiar version of the Sellmeier equation

$$n^2(\lambda) = 1 + \frac{B_1\lambda^2}{\lambda^2 - C_1} + \frac{B_2\lambda^2}{\lambda^2 - C_2} + \frac{B_3\lambda^2}{\lambda^2 - C_3}. \qquad (66)$$

Now we show the effects of material dispersion on the temporal duration of a pulse. In order to facilitate evaluating the integral in Eq. (63), we expand $k(\omega)$ as a truncated Taylor series about ω_0:

$$k(\omega) \approx k_0 + k'\Omega + \tfrac{1}{2}k''\Omega^2, \qquad (67)$$

where $k_0 = k(\omega_0)$, $k' = \left(\frac{\partial k}{\partial \omega}\right)_{\omega_0}$, and $k'' = \left(\frac{\partial^2 k}{\partial \omega^2}\right)_{\omega_0}$. Here k_0 is a constant phase shift across all frequencies, and k' is the group delay; we neglect both of these in this discussion. For the rest of this discussion we concern ourselves only with k'', the term which imparts quadratic spectral phase, leading to temporal broadening of the pulses. k'' is related to Eq. (66) by

$$\frac{\partial^2 k(\omega)}{\partial \omega^2} = \left(\frac{\lambda}{2\pi c}\right)\frac{\lambda^2}{c}\frac{\partial^2 n}{\partial \lambda^2}. \qquad (68)$$

With this knowledge, Eq. (64) becomes

$$E(z, \Omega) = A(\Omega)e^{i[\phi(\Omega)+k''\Omega^2 z]}. \qquad (69)$$

This implies that a careful choice of initial spectral phase $\phi(\Omega) = -k''\Omega^2 z$ will cancel out the effects of material dispersion. Thus by imparting a negative quadratic spectral phase, a pulse shaper can compensate for material dispersion so that a pulse has flat spectral phase, with a bandwidth-limited temporal duration after propagation. Because an arbitrary phase can be programmed on to the SLM, compression with a pulse shaper is not limited to

simple quadratic and cubic phase correction, making the device useful in applications where traditional grating and prism compressors cannot completely compensate the phase.

4.4.1 SHG as a Fitness Function

In order set the algorithm about this task, we must come up with a useful fitness function. Any intensity-dependent nonlinear process should work, as the peak intensity of a pulse will be at a maximum for transform-limited pulses, and will decrease with any spectral phase that stretches the pulse out. In this case we will use the spectral energy of second harmonic generation (SHG) as a fitness measure [39]. SHG is both easy to implement in a computer model and readily set up and measured in the lab using nonlinear optical crystals. Here we show that the spectral energy is indeed maximal for an un-chirped, transform-limited pulse.

Suppose we have a real electric field,

$$E(t) = \tfrac{1}{2}A(t)e^{i\phi(t)}e^{i\omega_0 t} + \text{c.c.}, \tag{70}$$

incident on a material with a non-zero second order susceptibility ($\chi^{(2)} \neq 0$). The result of a second-order nonlinear interaction with this field is $[E(t)]^2$:

$$[E(t)]^2 = \tfrac{1}{4}A(t)A^*(t) + \tfrac{1}{4}\left[A(t)e^{i\phi(t)}A(t)e^{i\phi(t)}\right]e^{i\cdot 2\omega_0 t} + \text{c.c.} \tag{71}$$

For the remainder of this discussion, we restrict ourselves to the second harmonic term, oscillating at $2\omega_0$,

$$E_{\text{SHG}}(t) = \tfrac{1}{4}A(t)e^{i\phi(t)} \cdot A(t)e^{i\phi(t)} \cdot e^{i\cdot 2\omega_0 t} \tag{72}$$

We are really after a measurable quantity. A laboratory spectrometer will return the power spectrum, the square of the magnitude of the Fourier transform,

$$S_{\text{SHG}}(\omega) \sim \tfrac{1}{4}\left|\int E_{\text{SHG}}(t)e^{i\omega t}dt\right|^2. \tag{73}$$

Accounting for the $2\omega_0$ carrier frequency of the second harmonic, this becomes

$$S_{\text{SHG}}(\omega - 2\omega_0) = \tfrac{1}{4}\left|\int A(t)e^{i\phi(t)} \cdot A(t)e^{i\phi(t)}e^{i\omega t}dt\right|^2. \tag{74}$$
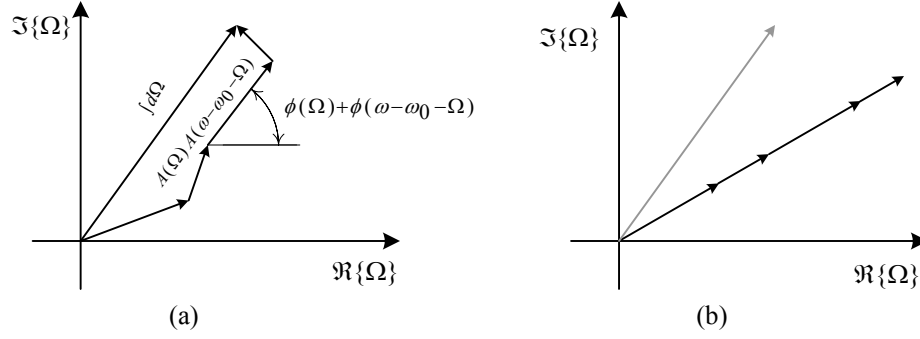
Figure 23: Illustration of the Triangle Inequality. For a given set of magnitudes, if their corresponding phases are different (a), the magnitude of the vector sum will be less than if their phases were equal (b).

Since multiplication in the time domain is equivalent to convolution in the frequency domain, we have

$$
\begin{aligned}
S_{\mathrm{SHG}}(\omega - 2\omega_0) &= \tfrac{1}{4} \left| \int_{-\infty}^{\infty} A(\Omega) e^{i\phi(\Omega)} A(\omega - \omega_0 - \Omega) e^{i\phi(\omega - \omega_0 - \Omega)} d\Omega \right|^2 \\
&= \tfrac{1}{4} \left| \int_{-\infty}^{\infty} A(\Omega) A(\omega - \omega_0 - \Omega) e^{i[\phi(\Omega) + \phi(\omega - \omega_0 - \Omega)]} d\Omega \right|^2
\end{aligned}
\tag{75}
$$

This integral can be considered an infinite sum of complex vectors. As Fig. 23 illustrates, the Triangle Inequality states that the magnitude of this sum will be greatest if all the vectors are in phase. As long as $\phi(\omega - \omega_0)$ is strictly linear or constant, $\phi(\Omega) + \phi(\omega - \omega_0 - \Omega)$ will be constant with respect to Ω. But if, as material dispersion affects the spectral phase of a pulse, ϕ is quadratic, then the phase of these vectors will vary with Ω, reducing the magnitude of the sum. Since this leads to a reduction in any component of S_{SHG}, we conclude that the following integral, which we use as our fitness function, is greatest for a transform limited pulse with only linear or constant spectral phase:

$$
f = \int S_{\mathrm{SHG}}(\omega) d\omega.
\tag{76}
$$

4.4.2 Expected Dispersion Parameters

For the experimental compression experiment we use two rods of BK7 glass to stretch the pulses. For BK7 at a central wavelength of 800 nm, the second derivative of Eq. (66)

47

evaluates to

$$\frac{d^2 n}{d\lambda^2} = 0.0494 \ \mu\text{m}^{-2}.$$

(77)

The dispersion parameter is then

$$D = -\frac{\lambda}{c}\frac{d^2 n}{d\lambda^2} = -1.3173 \times 10^{-4} \ \text{s/m}^2.$$

(78)

The expected broadening of a transform-limited pulse with a FWHM bandwidth of $\Delta\lambda$ is given by

$$\Delta\tau_p \approx -D \ L \ \Delta\lambda$$

(79)

In our case, we are using pulses with a bandwidth of 15 nm. For a 4 cm length of BK7 this amounts to 79 fs, while a 12 cm length of BK7 will broaden the pulses by 237 fs.

4.5 Simulation

The numerical simulation for the pulse compression process uses the search algorithm described earlier in this chapter, implementing a simulated fitness function. Figure 24 presents the fitness function algorithm in pseudocode. Here we present a description of the simulated fitness function, followed by the results of the numerical simulation.

4.5.1 Fitness Function Implementation

For the input to the simulation, we set up a pulse with an arbitrary chirp,

$$E(z,t) = E_0 e^{-a(z)t^2} e^{-i\left[b(z)t^2 - \omega t\right]},$$

(80)

with b commonly referred to as the chirp parameter in units of rad/fs^2. For a transform-limited pulse, $b = 0$. For an initially transform-limited pulse, the parameters $a(z)$ and $b(z)$ are given by [19]

$$a(z) = \frac{a_0}{1 + 4\left(a_0 k'' z\right)^2}$$

(81)

and

$$b(z) = \frac{1 + 2a_0^2 k'' z}{1 + 4\left(a_0 k'' z\right)^2},$$

(82)

48

z, cm	$a(z)$, ps^{-2}	$b(z)$, rad/ps^2
4	112.07	222.68
12	15.179	90.481

Table 2: Chirped pulse parameters after propagating through BK7.

where k'' is the group delay dispersion term, as previously described in Eq. (68). For BK7 at 800 nm, $k'' = 448$ fs^{2}rad^{-1}cm^{-1}. For an initial pulse with FWHM duration $\tau_p = 50$ fs,

$$a_0 = \frac{2\ln 2}{\tau_p^2} = 554.5 \text{ ps}^{-2}. \tag{83}$$

For the two lengths of glass in question, the pulse parameters are shown in Table 2. We expect that applying a quadratic phase of $-b$ to the phase mask in the pulse shaper should compensate for the chirp on a pulse and compress it to the bandwidth-limited duration.

The algorithm presented in Fig. 24 proceeds as follows. First, conjugate time and frequency axes t, w of length n = 1024 are initialized. Then an initial chirped pulse E0 is established following Eq. (80). Then to obtain a signal corresponding to what falls on the physical SLM, the numerical model of the pulse shaper performs an FFT on the input pulse. The aperture bounds are determined by the grating groove density, lens focal length, and SLM aperture dimensions as described in Chapter 2; any spectral components lying outside the SLM aperture are set to zero to simulate apodization. Then the phase mask $\phi(\omega)$, described by a trial chromosome, is applied according to

$$E_{\text{out}}(\omega) = E_{\text{in}}(\omega)e^{i\phi(\omega)}, \tag{84}$$

and an inverse Fourier transform produces the output pulse in time.

To compute the SHG signal generated by a given input pulse, we simply square the electric field in the time domain,

$$E(t)_{\text{SHG}} = |E_{\text{out}}(t)|^2. \tag{85}$$

One more FFT operation results in a power spectrum, much like one would measure with a laboratory spectrometer.

$$S_{\text{SHG}}(\omega) = |\mathcal{F}\{E_{\text{SHG}}(t)\}|^2, \tag{86}$$

```
1   Initialize( a, b )
2       set up time axis t
3       set up frequency axis w
4       wmin = lower bound of SLM aperture
5       wmax = upper bound of SLM aperture
6       E0 = exp(-(a+i*b)*t^2)
7   ...
8   double FitnessFunction( chromosome )
9       phi = chromosome.getPhaseMask()
10      Ef = fft( E0 )
11
12      // spectrum clipping on SLM aperture
13      for all frequencies w
14          if (w < wmin) OR (w > wmax) then Ef(w) = 0
15
16      // add the chromosome's phase
17      Ef = Ef * exp( i*phi )
18
19      // calculate SHG
20      E = ifft( Ef )
21      Eshg = E * E
22      Sssh = abs( fft( Eshg ) )^2
23
24      return sum( Sssh )
```

Figure 24: SHG fitness function pseudocode. `t`, `w` are real vectors of the time and frequency axes, respectively. `E0` is a complex vector describing the initial electric field in time, and `phi` is a real vector describing the phase mask on the SLM. `Sssh` is a real vector describing the power spectrum of the SHG signal.

The energy of the power spectrum, approximated with a sum over the sampled field, is then used as a fitness measure,

$$f = \sum_i S_{\text{SHG}}(\omega_i) \tag{87}$$

4.5.2 Simulation Results

Figures 25 and 26 show the results for simulating compression with an input beam stretched by 4 cm of BK7 glass, while Figs. 27 and 28 show the results for 12 cm of BK7 glass. The algorithm tends to find good solutions within 10 or 20 generations. As will be shown in the next section, experimental noise will increase this convergence time.

We can determine, from the final phase mask of each run, the group delay dispersion (GDD) applied to the pulse, from which we can find $d^2n/d\lambda^2$ and compare it to the known values for BK7 presented earlier. The quadratic phase imparted to a pulse propagating in a dispersive material is:

$$\frac{d^2\phi}{d\omega^2} = \frac{d^2k}{d\omega^2} \cdot z = \left(\frac{\lambda}{2\pi c}\right) \frac{\lambda^2}{c} \frac{d^2n}{d\lambda^2} \cdot z. \tag{88}$$

A mask that compensates for this phase should have the same magnitude of curvature. We estimate $d^2\phi/d\omega^2$ from the best mask by fitting a quadratic polynomial. From there it is simple to calculate $d^2n/d\lambda^2$, which turns out to be 0.0494 μm^{-2} for the 4 cm simulation and 0.0489 μm^{-2} for the 12 cm simulation. These are in excellent agreement with the expected value of 0.0494 μm^{-2}.

4.6 Experimental Procedure and Results

Figure 29 shows schematically the experimental setup. The beam from a Ti:sapphire oscillator (KM Labs), with 40 nm optical bandwidth centered at 790 nm, was collimated to $2w_{\text{in}} \approx 4$ mm diameter and sent into the shaper, then through a length of glass, and is then characterized by a SHG-FROG device [40], which is used to both provide the SHG fitness function and subsequently characterize the pulse. The nonlinear medium in the FROG is a 100 μm thick BBO crystal. First, with the glass removed, the pulse shaper is adjusted so that the pulses exiting the shaper are nearly transform-limited. To verify this,

Phase Mask Evolution

Phase (rad)

← quadratic fit

40
30
20
10
0
−10

2.6 2.55 2.5 2.45 2.4 2.35 2.3 2.25 2.2

0 200 400 600 Generation

Frequency (rad/fs)

SHG Spectrum Evolution

Intensity (arb.)

15000
10000
5000
0

5 4.9 4.8 4.7 4.6 4.5 4.4

0 200 400 600 Generation

Frequency (rad/fs)
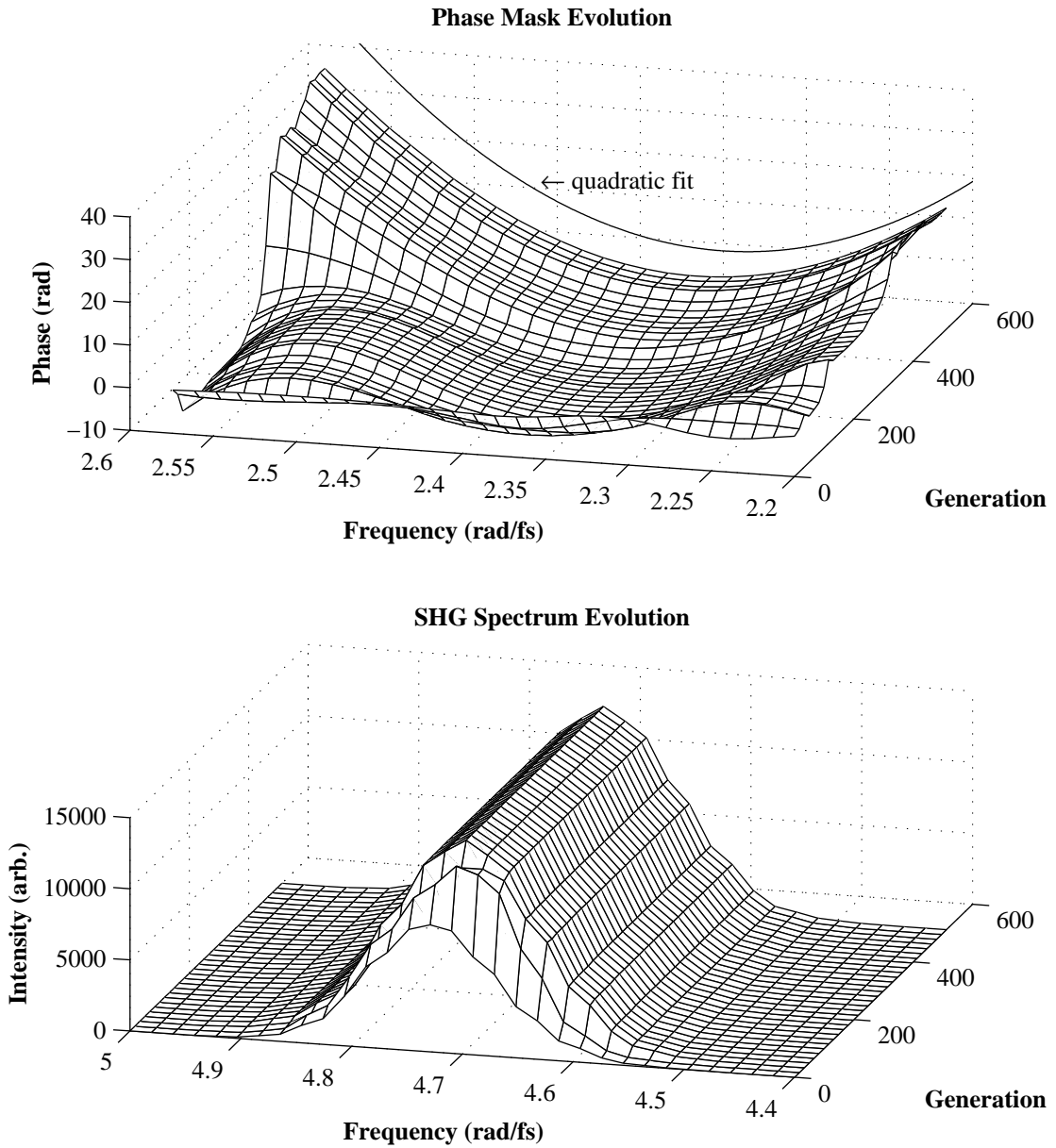
Figure 25: Simulated phase mask and SHG spectrum evolution for 4 cm BK7 compression run.

52
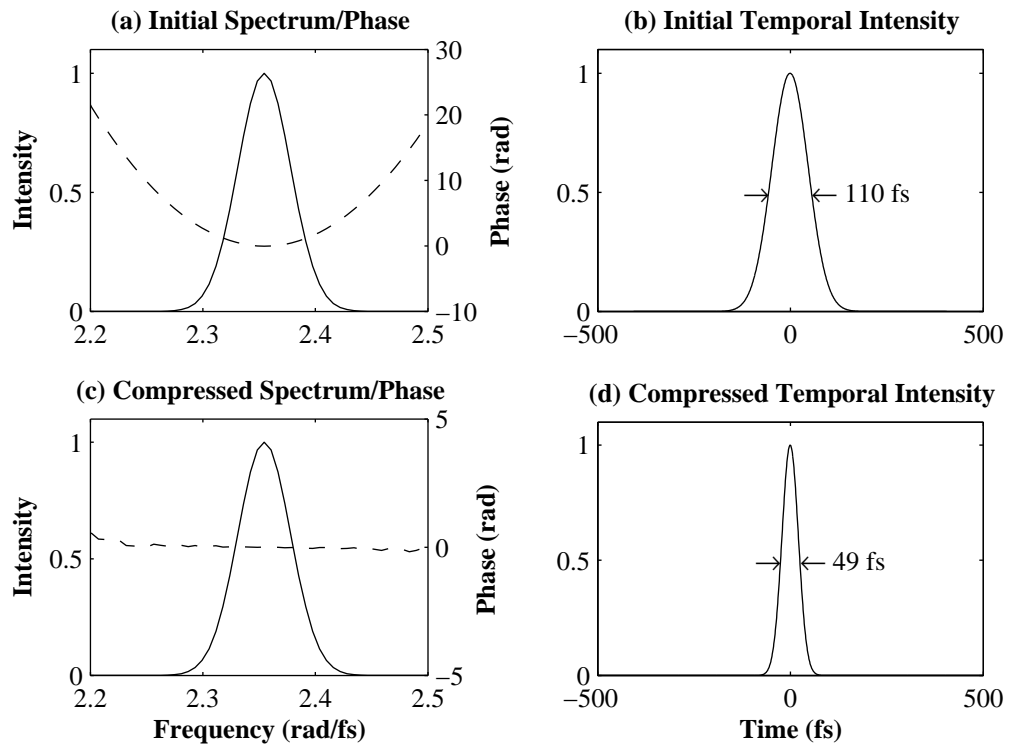
Figure 26: Simulated pulse profiles before and after compression with 4 cm BK7 in the path of the beam. Solid lines are intensity, dashed lines are phase.

Phase Mask Evolution

← quadratic fit

Phase (rad)

40
20
0
−20
−40

Frequency (rad/fs)

2.6   2.55   2.5   2.45   2.4   2.35   2.3   2.25   2.2

Generation

600
400
200
0

SHG Spectrum Evolution

x 10^4

Intensity (arb.)

15
10
5
0

Frequency (rad/fs)

5   4.9   4.8   4.7   4.6   4.5   4.4

Generation

600
400
200
0
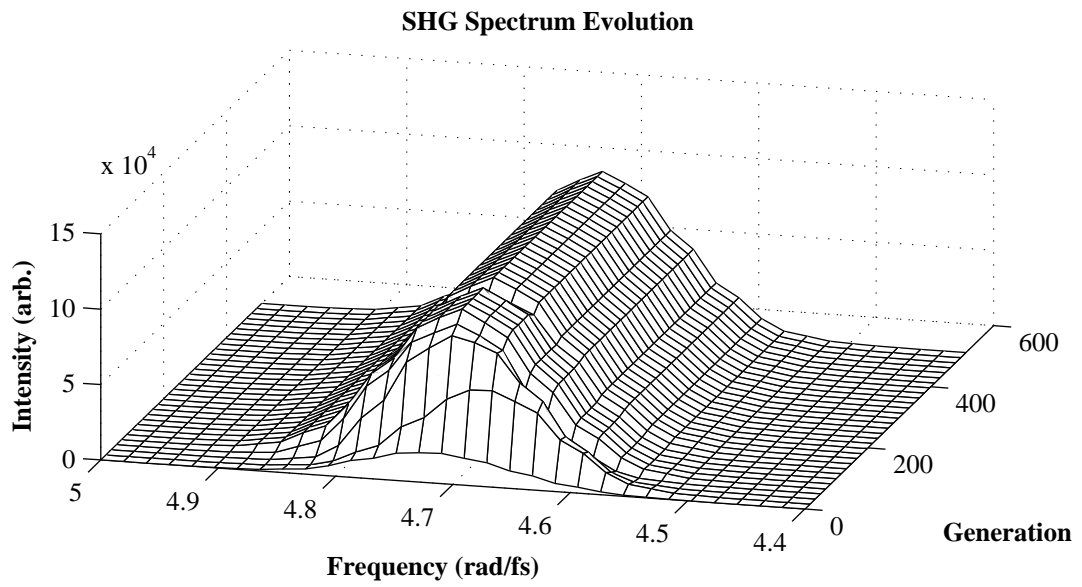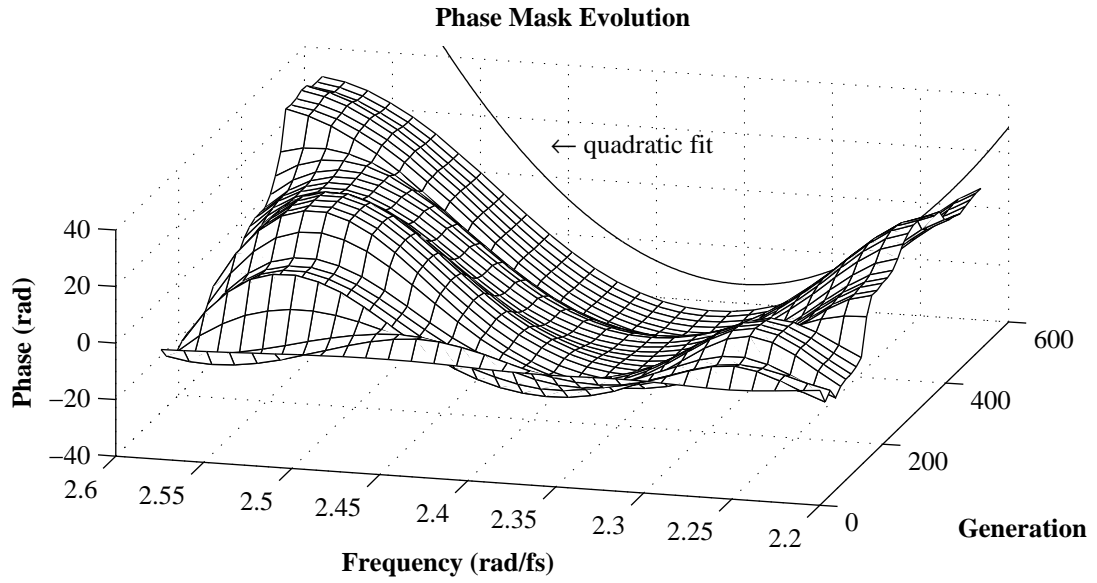
Figure 27: Simulated phase mask and SHG spectrum evolution for 12 cm BK7 compression run.
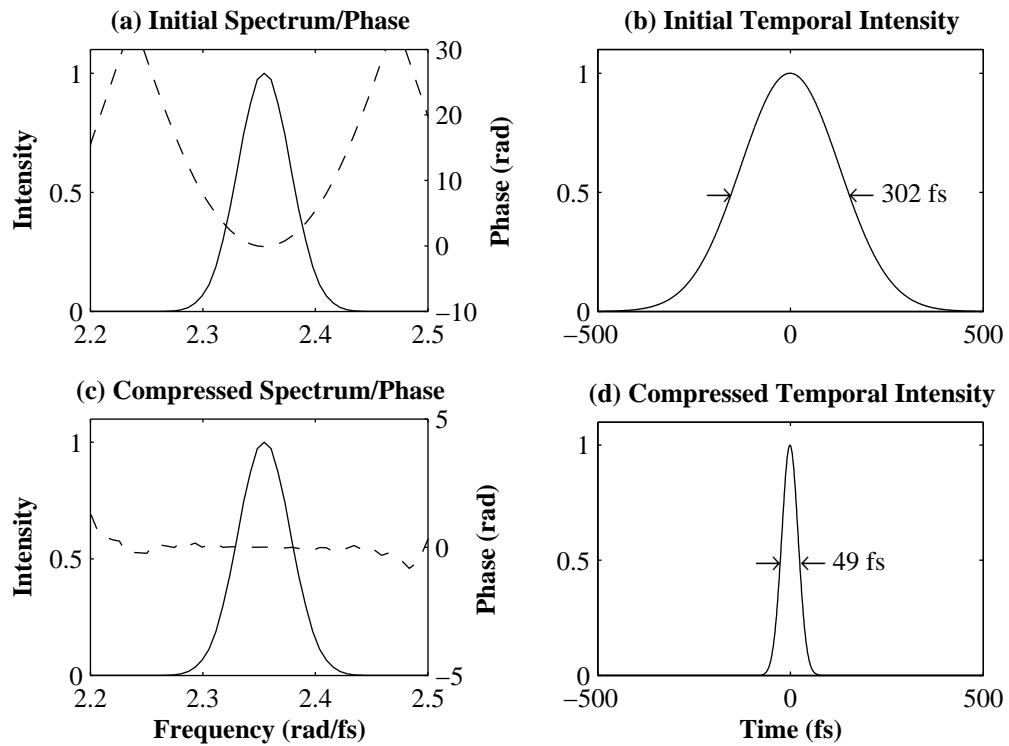
Figure 28: Simulated pulse profiles before and after compression with 12 cm BK7 in the path of the beam. Solid lines are intensity, dashed lines are phase.

a measurement of the pulse is taken with all the SLM elements set to 0. To measure the fitness function, the delay line in the SHG-FROG is set to time-zero (so that both pulses reach the doubling crystal simultaneously). The area under the SHG spectrum's curve is computed, and that value is used as a measure of fitness. As in the simulation, the blue light exiting the crystal will be most intense for a transform limited pulse. Finally the piece of glass is inserted in the path of the beam, and the algorithm searches for a phase mask that maximizes the signal in the FROG's spectrometer.

First we insert 4 cm of BK7 glass in the path of the beam. Figure 30 shows the evolution of the phase mask and the measured SHG spectrum for a run of a ($\lambda = 14, \mu = 7$) CMA-ES algorithm over 512 generations, utilizing a 32-point spline phase mask. For about the first 100 generations, the trial masks appear to be very random, but the solution converges quickly. Figure 31 shows the temporal and spectral intensity profiles and phases of the pulses both before and after running the compression algorithm. The top panels show the pulse with a zero phase mask applied in the pulse shaper, while the bottom panels show the final compressed pulse. Figures 32 and 33 show the corresponding results for 12 cm of BK7 glass inserted.

From the best phase masks found for both lengths of glass, we find an estimate for $d^2n/d\lambda^2$ by fitting a quadratic curve to the mask. For 4 cm of BK7, we estimate $d^2n/d\lambda^2 \approx$ 0.095 μm^{-2}. For 12 cm, we estimate $d^2n/d\lambda^2 \approx 0.0559$ μm^{-2}. To put the differences between these and the actual values into perspective, we can use the known values of GVD and estimate the length of glass which turns out to be 7.7 cm and 13.5 cm for the 4 cm and 12 cm lengths of BK7, respectively. In spite of this discrepancy, both compression runs yielded essentially transform-limited pulses. These GVD calculations assume that the glass is the only source of dispersion, neglecting the shaper itself and potential spectral amplitude attenuation at wrap points on the mask.

4.7 *Algorithm Comparison*

To demonstrate the benefits of using the CMA-ES algorithm, we compare it with a standard ES. Here we are interested in which algorithm finds a phase mask with the highest fitness
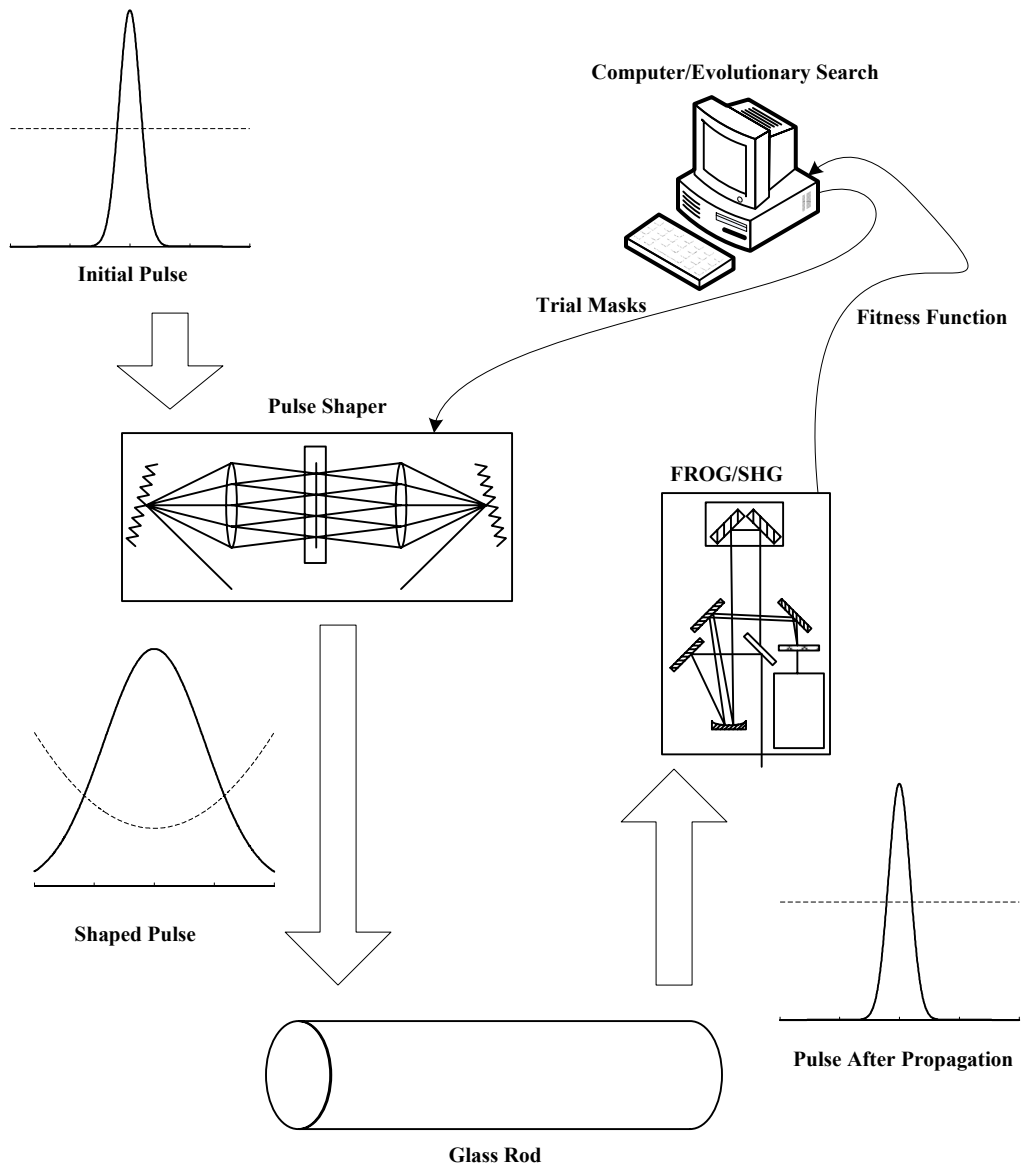
Figure 29: Schematic of pulse compression experimental setup.

Phase Mask Evolution

← quadratic fit

Phase (rad)

10

0

−10

600

400

200

0

Generation

2.6   2.55   2.5   2.45   2.4   2.35   2.3   2.25

Frequency (rad/fs)

SHG Spectrum Evolution

Intensity (arb.)

1000

500

0

500

400

300

200

100

Generation

4.95   4.9   4.85   4.8   4.75   4.7   4.65   4.6

Frequency (rad/fs)
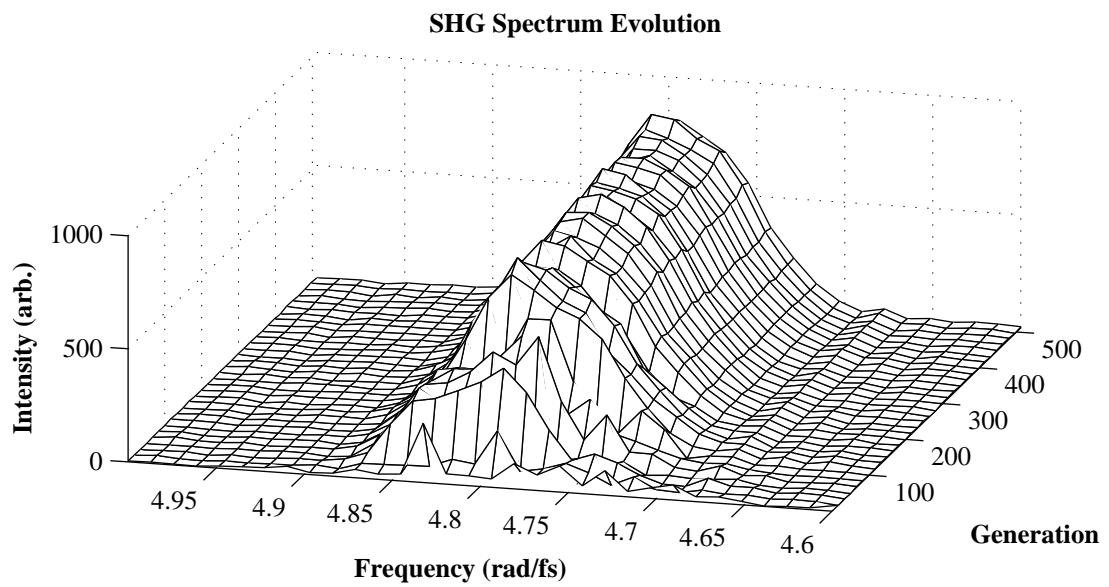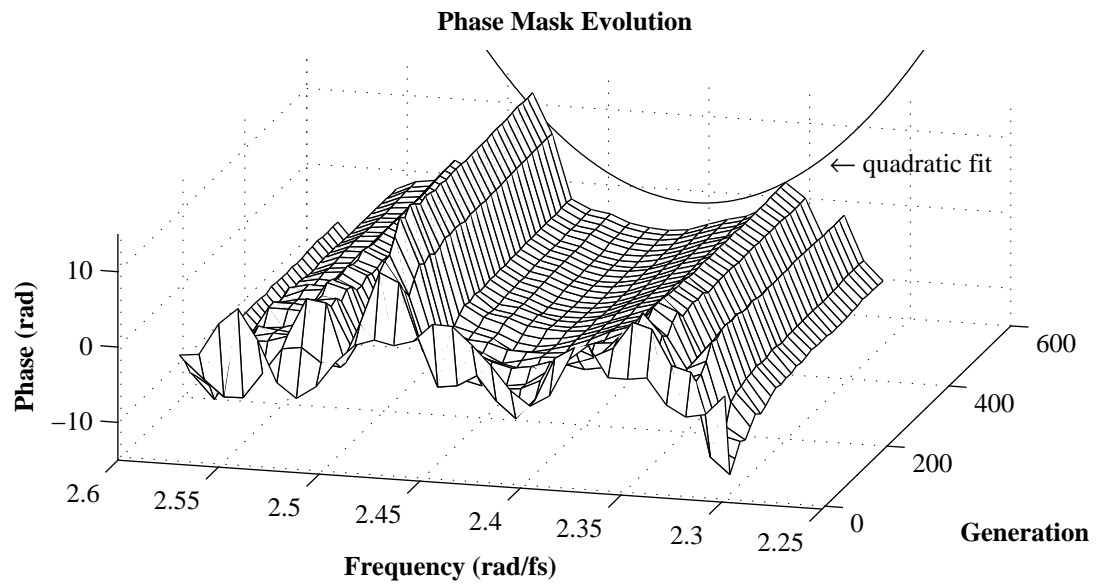
Figure 30: Phase mask and SHG spectrum evolution for 4 cm BK7 compression run.
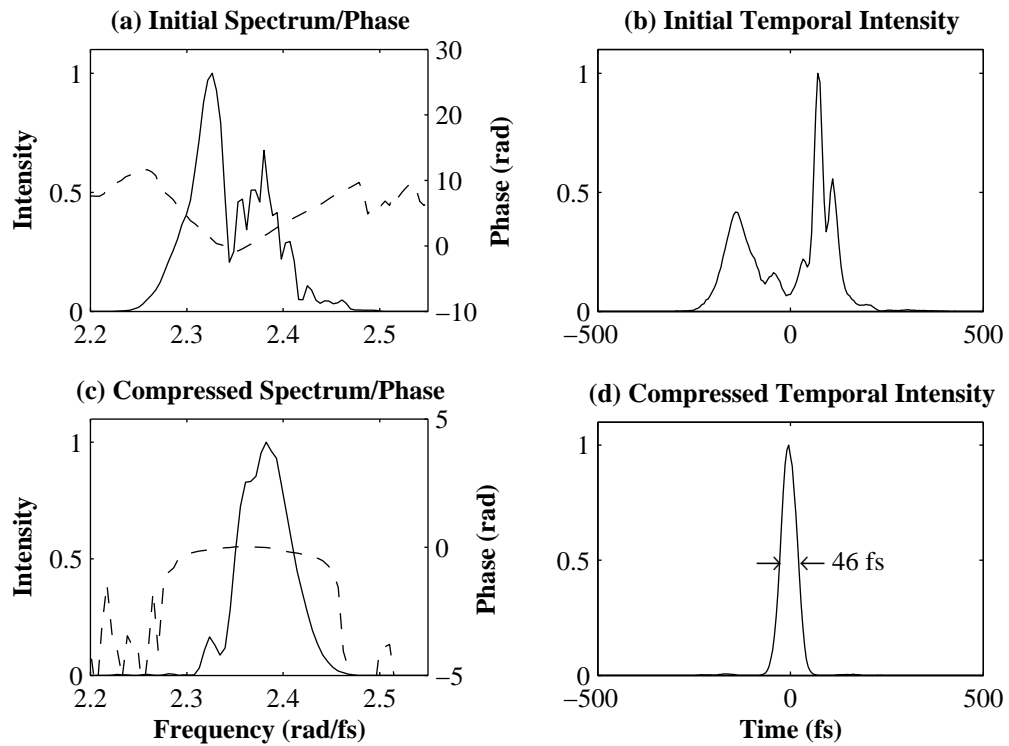
Figure 31: Pulse profiles before and after compression with 4 cm BK7 in the path of the beam. Solid lines are intensity, dashed lines are phase.

Phase Mask Evolution

SHG Spectrum Evolution
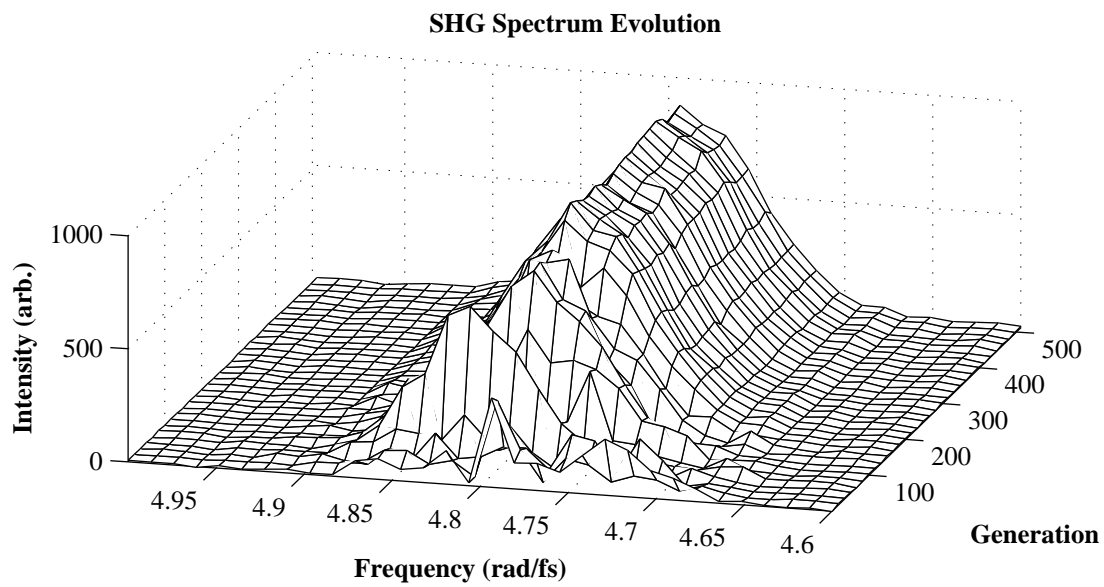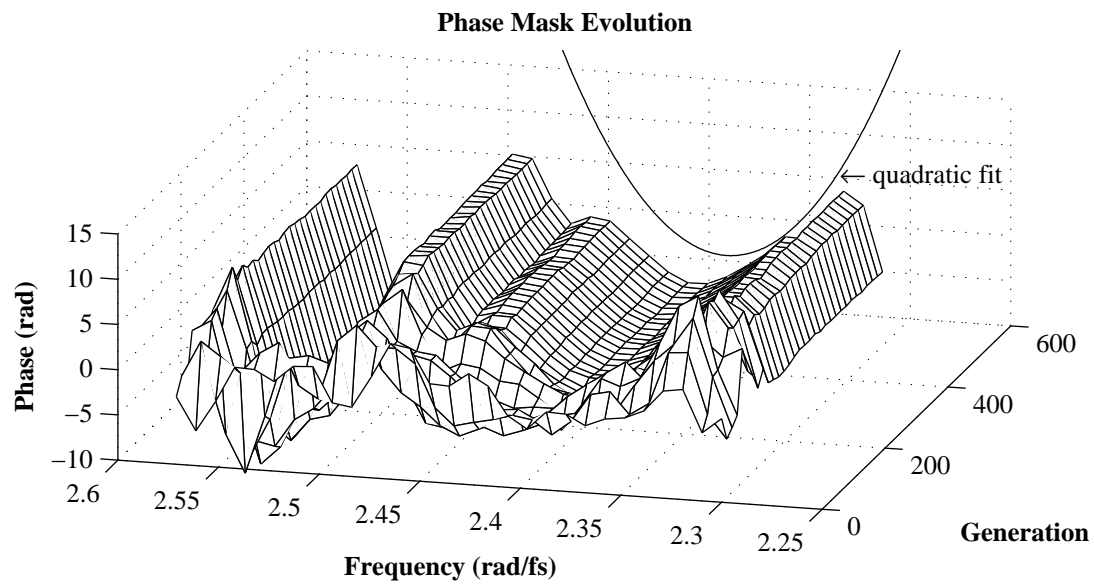
Figure 32: Phase mask and SHG spectrum evolution for 12 cm BK7 compression run.

60
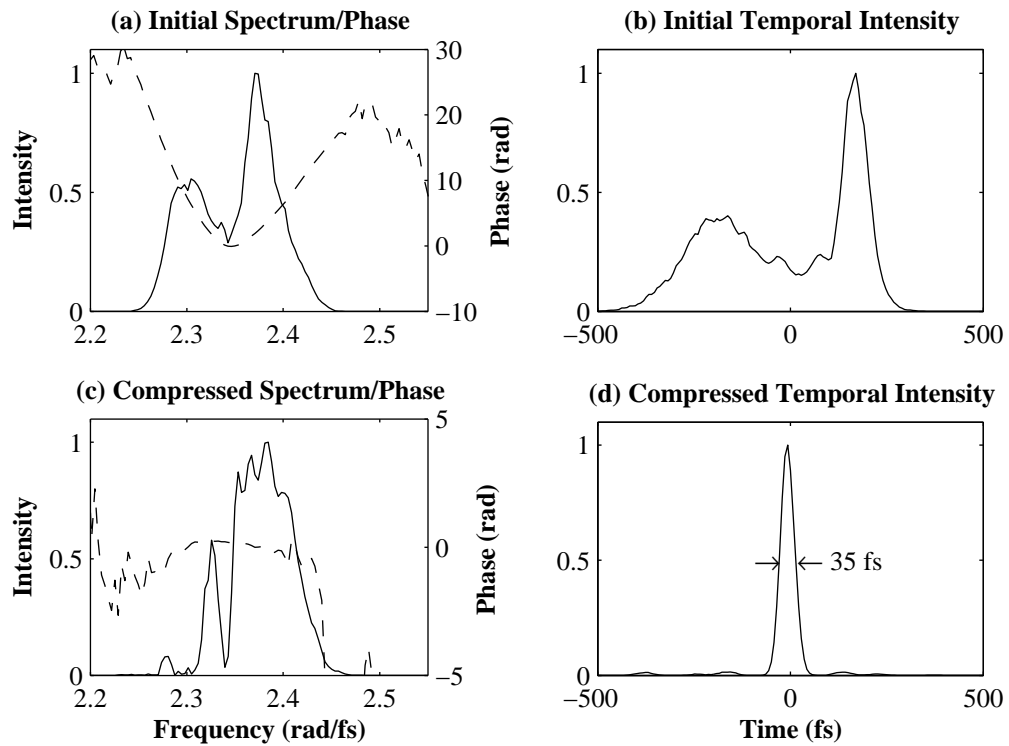
Figure 33: Pulse profiles before and after compression with 12 cm BK7 in the path of the beam. Solid lines are intensity, dashed lines are phase.

function using the fewest number of trials. We compare both algorithms for low- and high-dimensional searches. In the following trials, we begin with an initial guess $x_0 = 0$ corresponding to a zero phase mask. Initially $\sigma = 1.0$ rad for both algorithms, which was empirically found to work best. For CMA-ES, we follow a rule-of-thumb for determining μ and λ [38]. However for ES, we ran a number of combinations of μ and λ, finally selecting values that led to best algorithm performance.

In simulation, we compare $(\lambda = 10, \mu = 5)$ CMA-ES with $(\lambda = 16, \mu = 4)$ ES for a 32-dimensional spline phase mask and $(\lambda = 14, \mu = 7)$ CMA-ES with $(\lambda = 64, \mu = 16)$ ES for a 32-dimensional spline phase mask. Both algorithms ran for at least 512 generations, and were repeated 3 times. To visualize performance, we plot the maximum f of each generation versus the number of trials, as shown in Fig. 34. For an 8-dimensional search space, the performance of CMA-ES is on par with ES. But for a higher-dimensional search space, CMA-ES outperforms ES, as expected.

In Fig. 35 we compare the experimental performance of $(\lambda = 10, \mu = 5)$ CMA-ES with $(\lambda = 32, \mu = 4)$ ES for a 32-dimensional spline phase mask and $(\lambda = 14, \mu = 7)$ CMA-ES with $(\lambda = 32, \mu = 4)$ ES for a 32-dimensional spline phase mask. Again, we show that for low-dimensional searches, there is little benefit to using the CMA-ES method. However, the CMA-ES algorithm converges much more rapidly than the ES when the dimensionality of the search space is increased.

4.8   Conclusions

The algorithm performed well in its task of optimizing the SHG signal. The numerical simulations produced reasonable phase masks which agree well with theoretical dispersion characteristics. The experimental data shows the control system is capable of optimizing a feedback signal even in the presence of laboratory noise and unknowns. Here we have demonstrated the application of a new algorithm to coherent control. For higher-dimensional search spaces, CMA-ES outperforms the traditional ES in both simulation and experiment. We expect this algorithm to find usefulness in the field, finding solutions more quickly than previously possible.
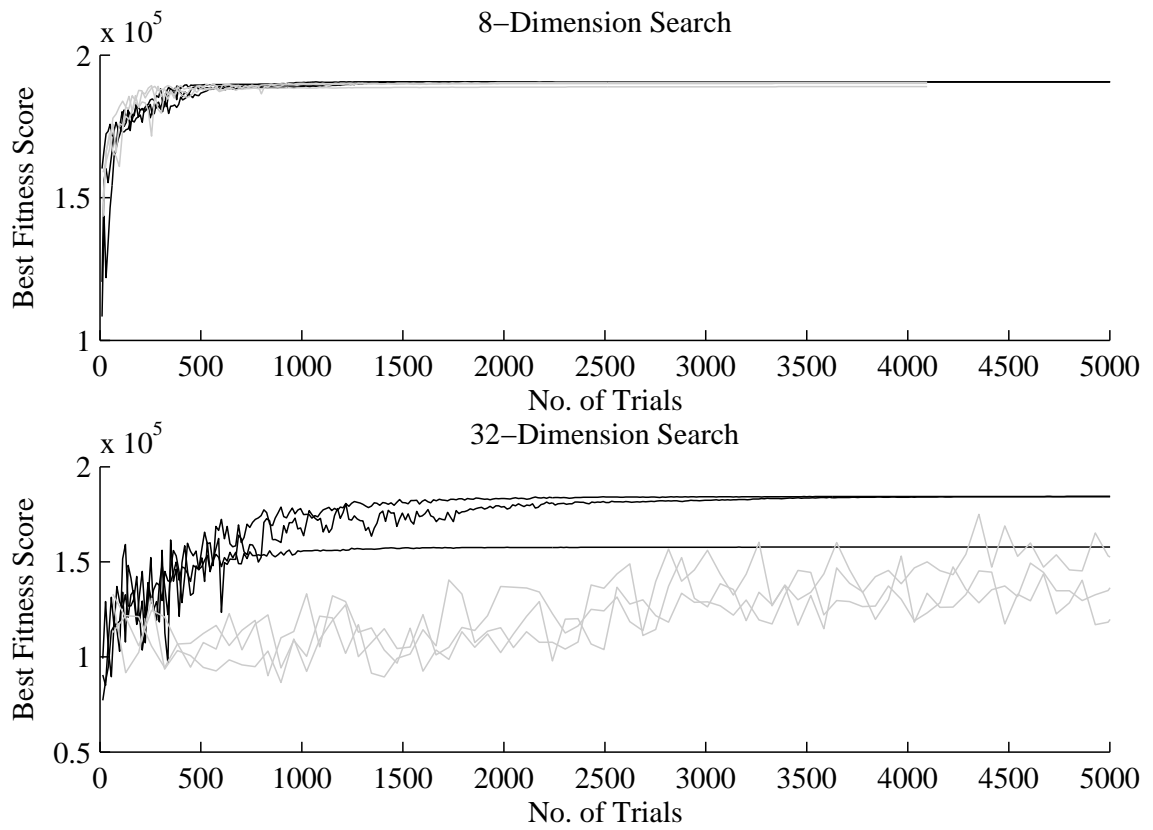
Figure 34: Theoretical comparison of performance of CMA-ES (black lines) and ES (gray lines). Fitness scores are integrated spectral energy of SHG signal.
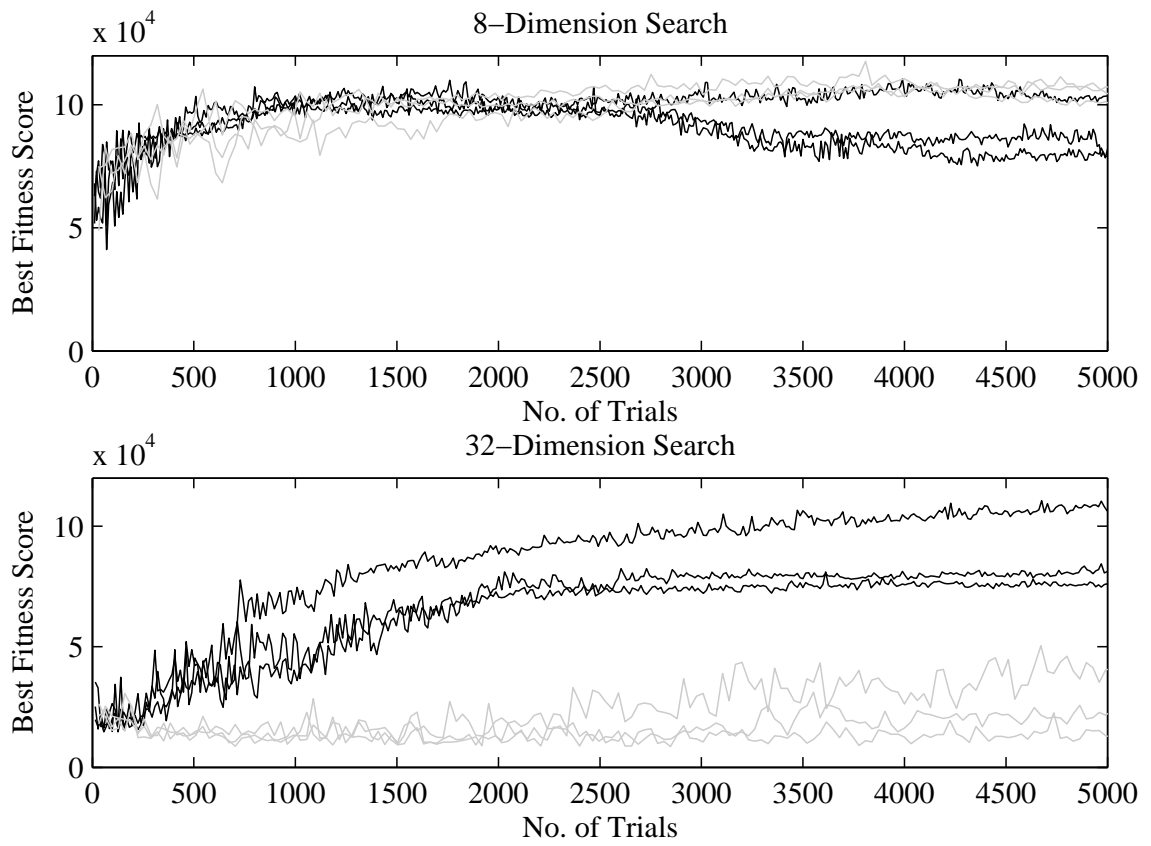
Figure 35: Experimental comparison of performance of CMA-ES (black lines) and ES (gray lines). Fitness scores are integrated spectral energy of SHG signal.

Chapter V

CONCLUSIONS AND FUTURE WORK

In anticipation of delving in to experimental research in quantum coherent control, I have presented in this thesis the development of the necessary prerequisites: ultrafast pulse shaping and learning algorithms. In the first chapter, the concepts of Fourier synthesis pulse shaping were presented and applied to the design and construction of a spectral phase-only pulse shaper. Through SHG-FROG and spectral interferometry, we confirmed the pulse shaper's operational capabilities. In Chapter 3, a spectral phase and amplitude pulse shaper was presented, which can access a wider range of temporal pulse shapes. Again, an analysis of the shaper's operation was explored, and the shaper's functionality demonstrated in the laboratory. Finally in Chapter 4 we implemented a CMA-ES algorithm and applied it to a rudimentary coherent control application: pulse compression using a nonlinear process (SHG) as a measure of fitness. In this, we show the closed-loop control apparatus achieves its goal of tailoring pulse shapes to meet a defined objective. Future research will use this apparatus in several coherent control applications.

First we will study molecular vibrations, in particular those of SF_6. Our experimental setup consists of a hollow-core, gas-filled fiber, into which we direct a pump pulse, followed by a probe pulse [41]. The probe pulse exhibits spectral sidebands corresponding to the vibrational wavepacket excited by the pump. We expand upon previous work by shaping the pump pulse and using a computer-controlled feedback loop to enhance particular sidebands, as shown in Fig. 36. By doing this, we will probe the anharmonicity of the vibrational potential of the v_1 mode of SF_6.

The second area we wish to explore is the search landscape, or topography, of coherent control problems [36]. We have already begun collaboration with Computer Science Department to see what information search algorithms experts may glean from our experimental data. We have already benefitted greatly from these discussions, from which came the idea
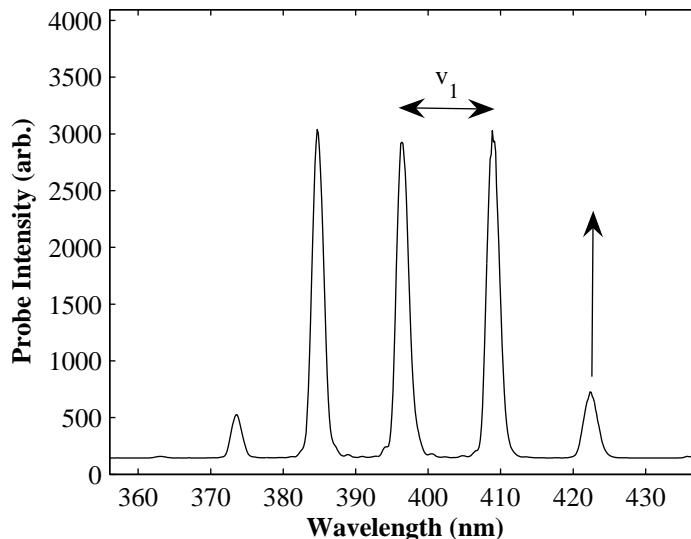
Figure 36: Measured SF_6 sidebands. In a coherent control experiment, we will attempt to enhance $2v_1$ while suppressing v_1.

of implementing the CMA-ES algorithm in Chapter 4.

Finally, we will re-build a variant of the spectral phase and amplitude shaper described in Chapter 3 and use it in microscopy applications. It has been shown that in pump-probe microscopy, shaped pump pulses can be used as a contrast mechanism [42]. Here we will investigate the use of controlled pump pulses to provide contrast between proteins and complex molecules that, with traditional techniques, have strikingly similar spectroscopic signatures.

The field of coherent control is young, and there remain many exciting opportunities to discover new applications. Through the apparatus described in this thesis, we have laid the groundwork for much future research.

Appendix A

PULSE SHAPER TECHNICAL DRAWINGS

This appendix contains drawings of the phase-only pulse shaper described in Chapter 2, including exploded assemblies of the individual components. Units are in mm unless otherwise specified.

The OptoSigma stages used are part numbers 123-2480 (25 mm 2-axis goniometer), 122-0070 (40 mm extended contact bearing steel stage), and 124-0030 (40 mm rotation stage).

160.25

160.25

320.5

137.65

104.14

6°

PULSE SHAPER ASSEMBLY
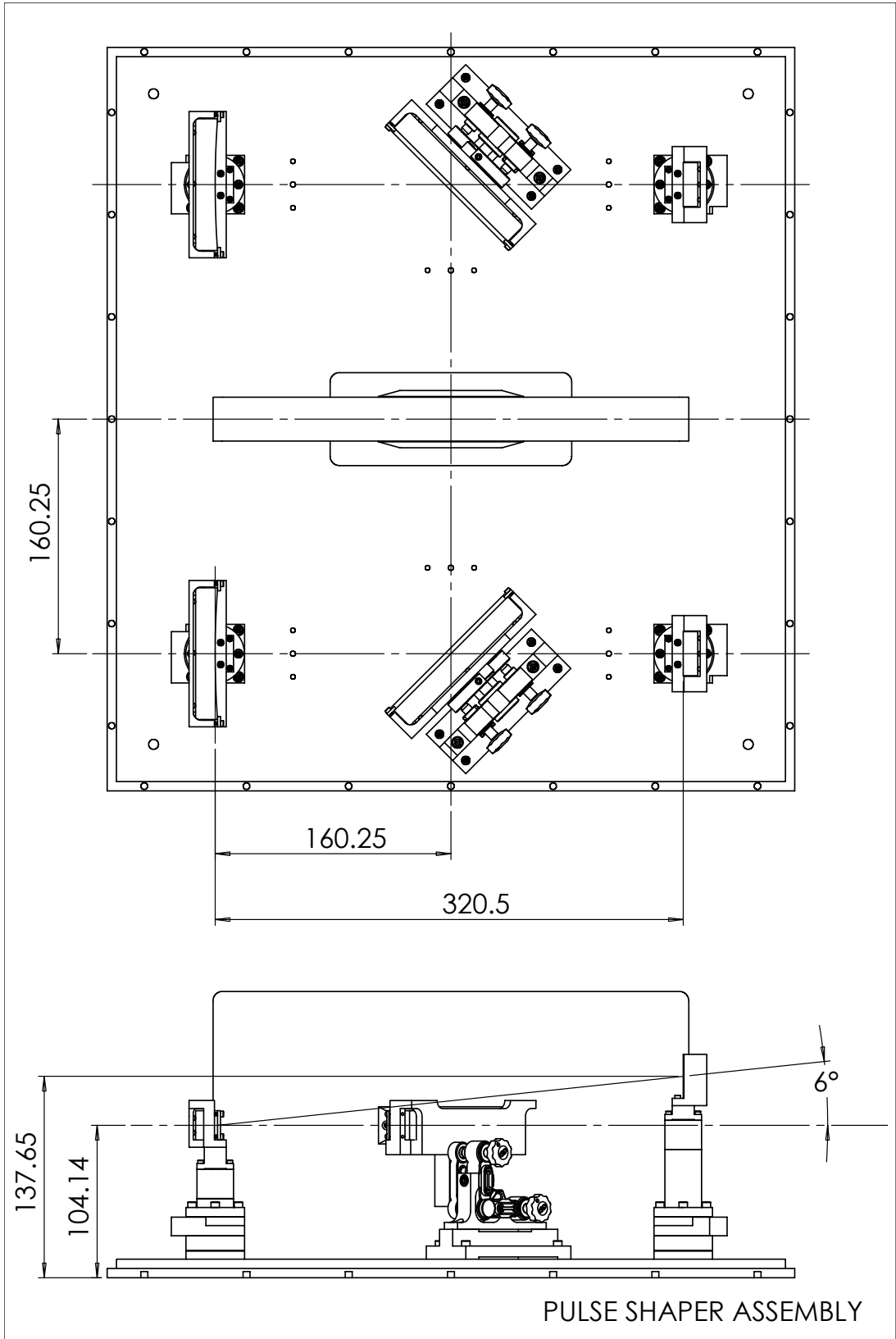
Figure 37: Pulse Shaper Assembly

GRATING ASSEMBLY

FOLD MIRROR ASSEMBLY

FOCUSING MIRROR ASSEMBLY

BASE PLATE

SPATIAL LIGHT MODULATOR
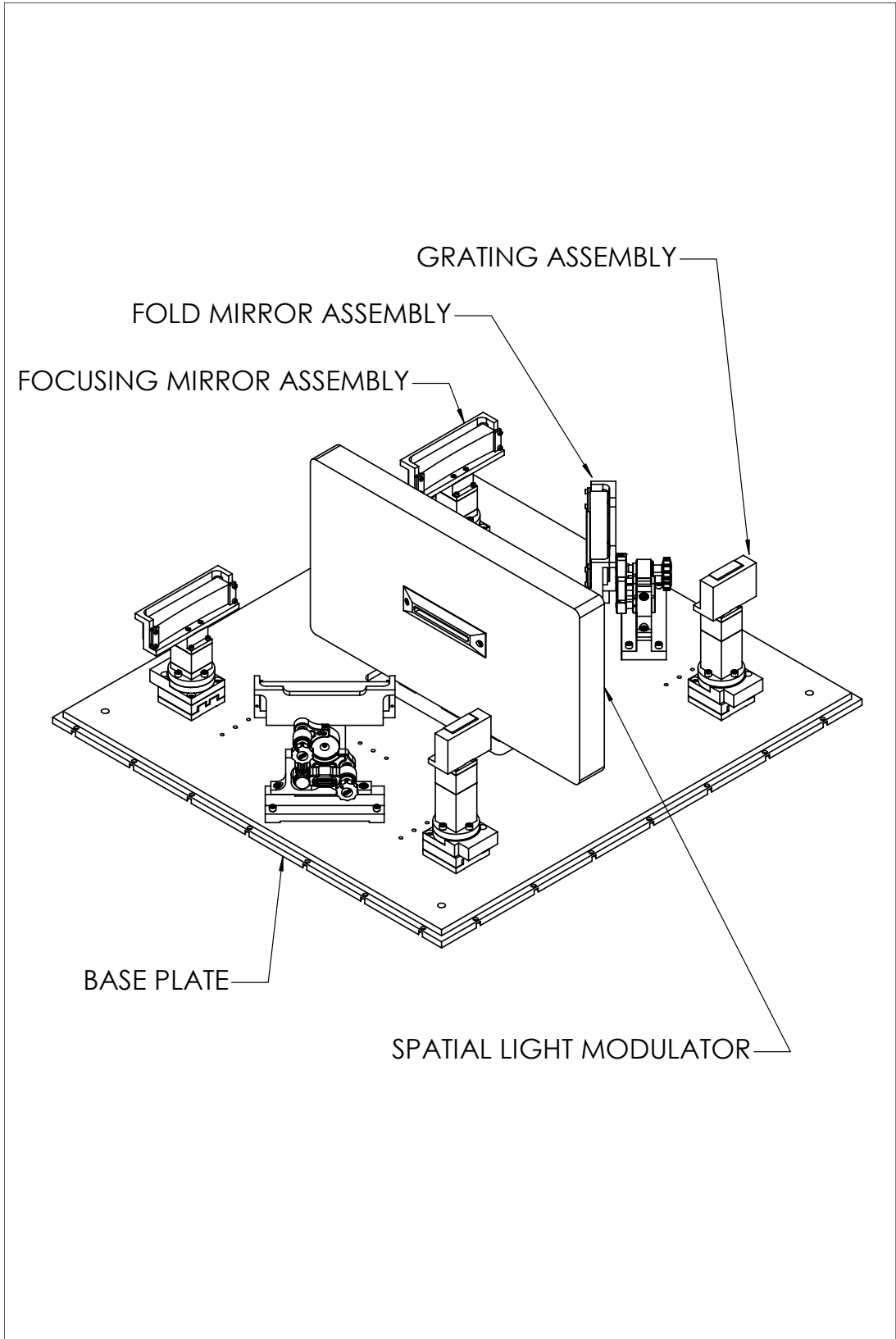
Figure 38: Pulse Shaper Components

FOCUSING MIRROR

FOCUS MIRROR MOUNT

BALL BEARING (3X)

RETAINING CLIP (2X)

SQUARE SPACER

GONIOMETER

ROUND SPACER

ROTATION STAGE

TRANSLATION STAGE
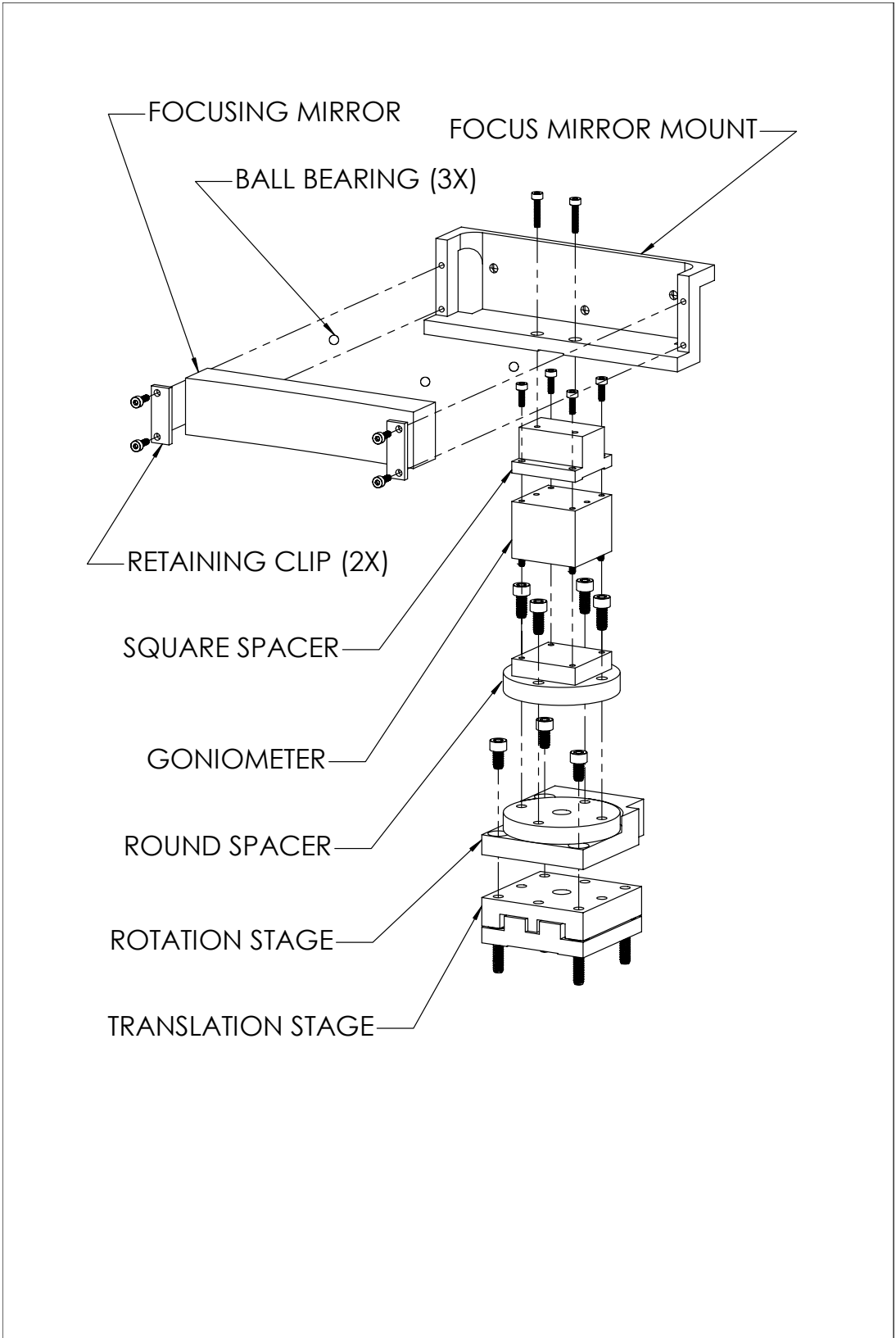
Figure 39: Focusing Mirror Assembly

FLAT MIRROR

FOLD MIRROR MOUNT

MOUNT ADAPTER

POST

BALL BEARING (3X)

RETAINING CLIP (2X)

MIRROR MOUNT

BRACKET

BASE
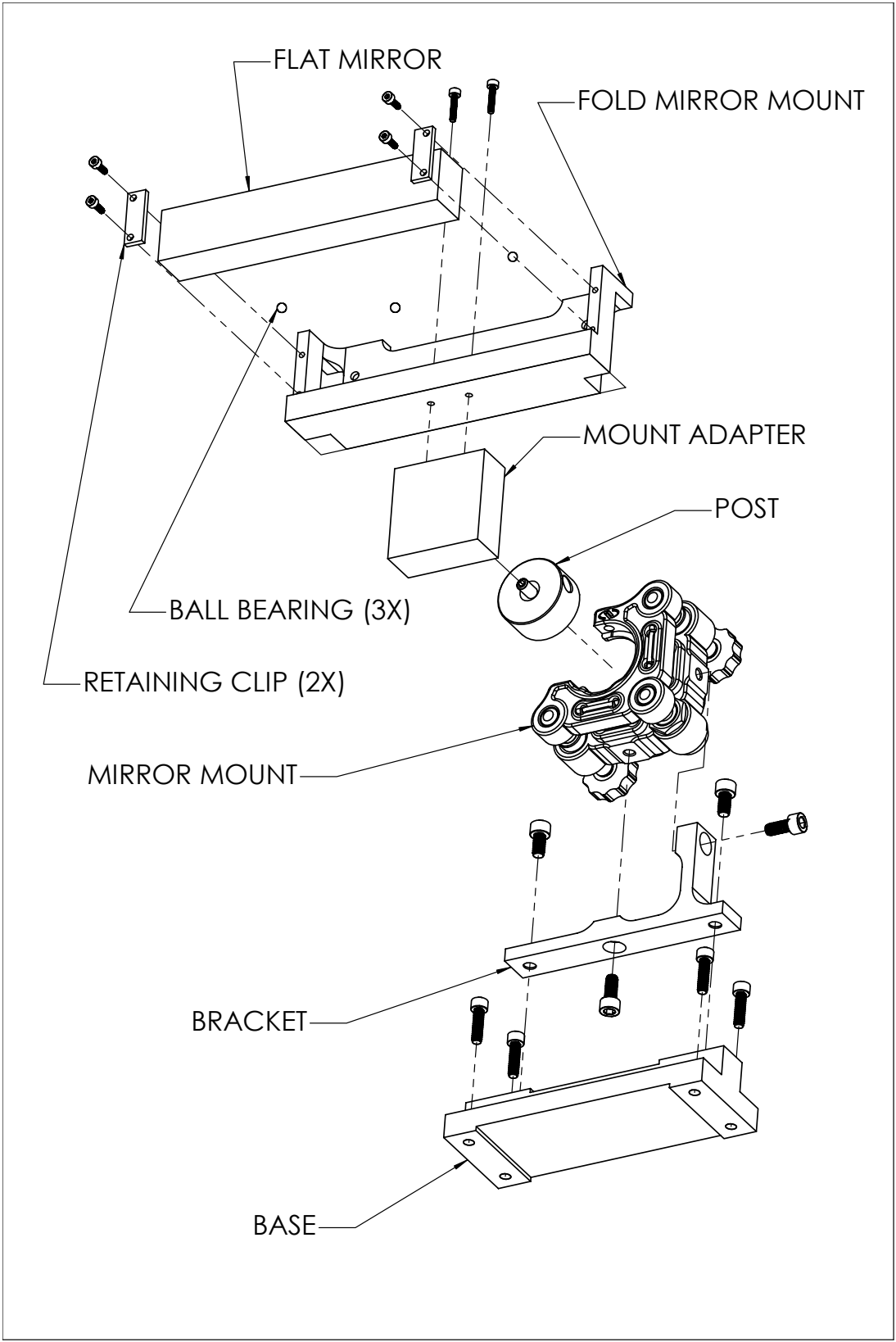
Figure 40: Fold Mirror Assembly

RETAINING CLIP (2X)

GRATING

GRATING MOUNT

BALL BEARING (3X)

SQUARE SPACER

GONIOMETER

ROUND SPACER

ROTATION STAGE

TRANSLATION STAGE
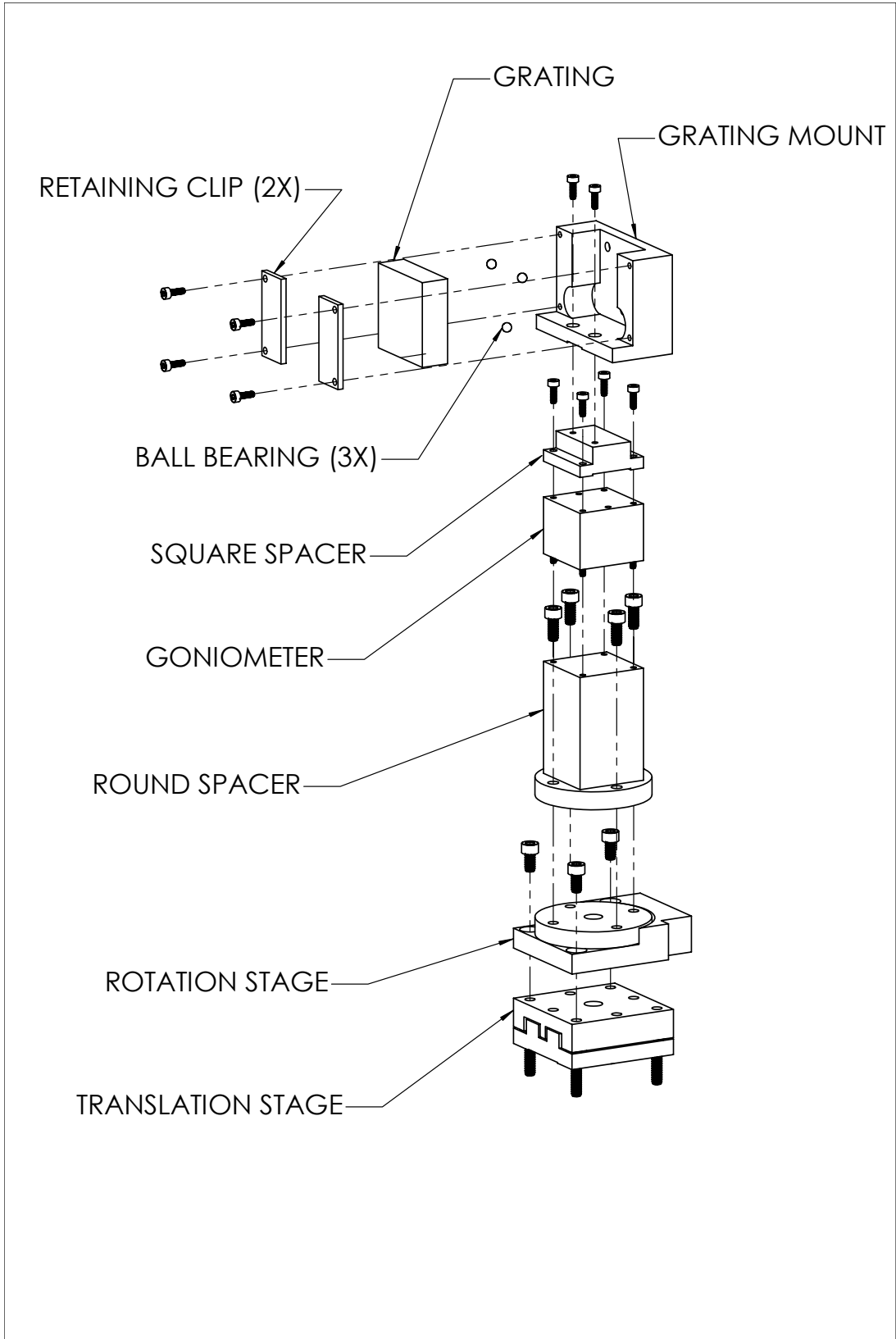
Figure 41: Grating Assembly

Appendix B

PULSE SHAPER ALIGNMENT PROCEDURES

We include here the procedure for alignment of the pulse shaper. Since misalignment can result in clipping and wavefront distortions, temporal chirp, spatial chirp, and pulse front tilt, a Grenouille [43] or other ultrafast pulse measurement tool that can characterize ultrafast pulses both temporally and spatially is required for precise alignment. Here we make use of white light generation in glass and ionization in air as rough gauges of temporal duration and spatial quality of the pulses during alignment process. Also note that the pulse shaper is *extremely* sensitive to input beam collimation.

The beam height changes inside the pulse shaper with tilted gratings and mirrors so stray surface reflections may end up at eye-level. Wearing appropriate safety goggles, be sure to check for these dangerous back-reflections. If the laser mode changes with output power, we recommend employing a half-wave plate followed by a polarizer for attenuation. This also ensures that the input beam is properly polarized for the SLM.

In addition, we have noted for a well-aligned shaper, the back-reflection from the SLM can propagate back to the laser source, potentially causing *severe damage* to an amplifier system. For initial alignment we make use of this back-reflection; during this process we recommend operating the laser source at the lowest power that will produce visible light. After the initial alignment of both halves is complete, the SLM mounting screws can be loosened, and the SLM should be tilted at an angle just large enough to prevent the back-reflection from feeding back into the laser source.

B.1   Initial Alignment

For the initial alignment, prepare four index cards as illustrated in Fig. 42. Trim card (b) so it does not obstruct the beam passing over it when placed inside the pulse shaper. Printing rules spaced at $\frac{1}{16}''$ on this card will be useful for measuring the width of the spectral line.
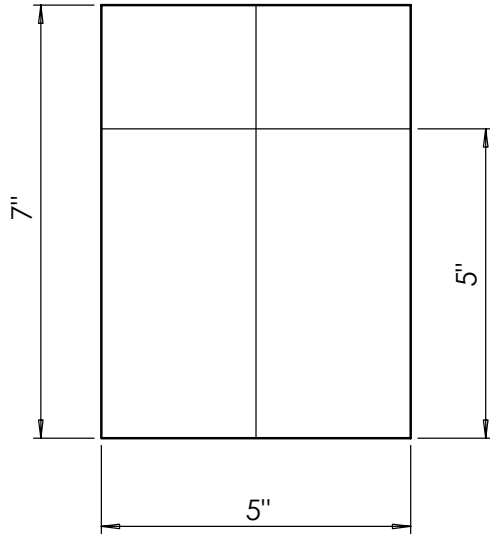
(a) Entrance/exit height from baseplate
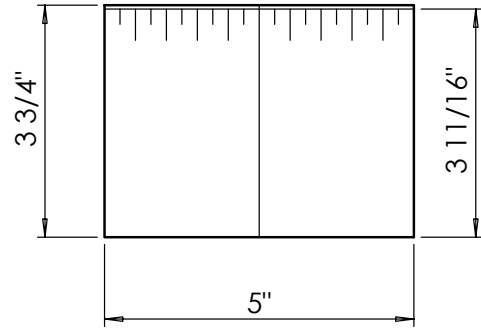
(b) SLM height from baseplate
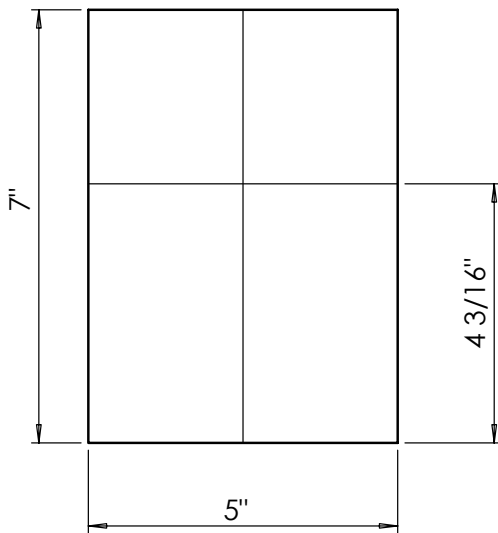
(c) SLM height from table
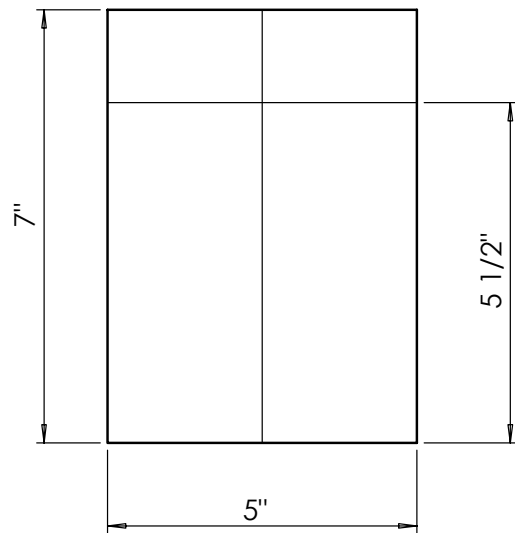
(d) Entrance/exit height from table

Figure 42: Alignment index cards
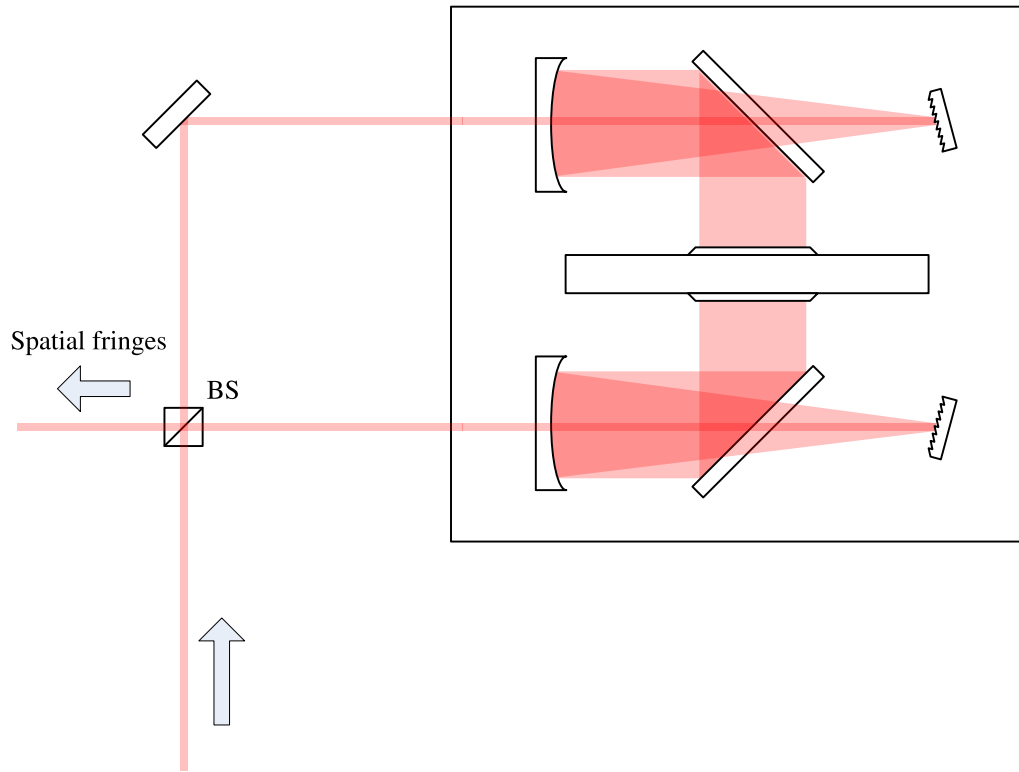
Figure 43: For alignment, a beam is split by a non-polarizing beamsplitter (BS), and is sent into each half of the shaper.

For easy placement of these cards, alignment holes have been drilled on the base plate.

We have found the best results when working with an optical ring to align the pulse shaper, illustrated in Fig. 43. A non-polarizing cube beam-splitter is used to split light from a laser source into two arms. Each is directed in to a separate half of the pulse shaper. When the shaper is well-aligned, both these beams will overlap, producing interference fringes in the far-field.

Perform the following procedures first on the output side of the pulse shaper, then repeat for the input side.

1. Set all stages and adjustment screws to their center positions. Ensure that the input beam is well collimated, with a diameter of 5 mm. Any light outside this dimension will be clipped at the SLM aperture.

2. Using card (a) with the alignment hole between the input focusing mirror and the
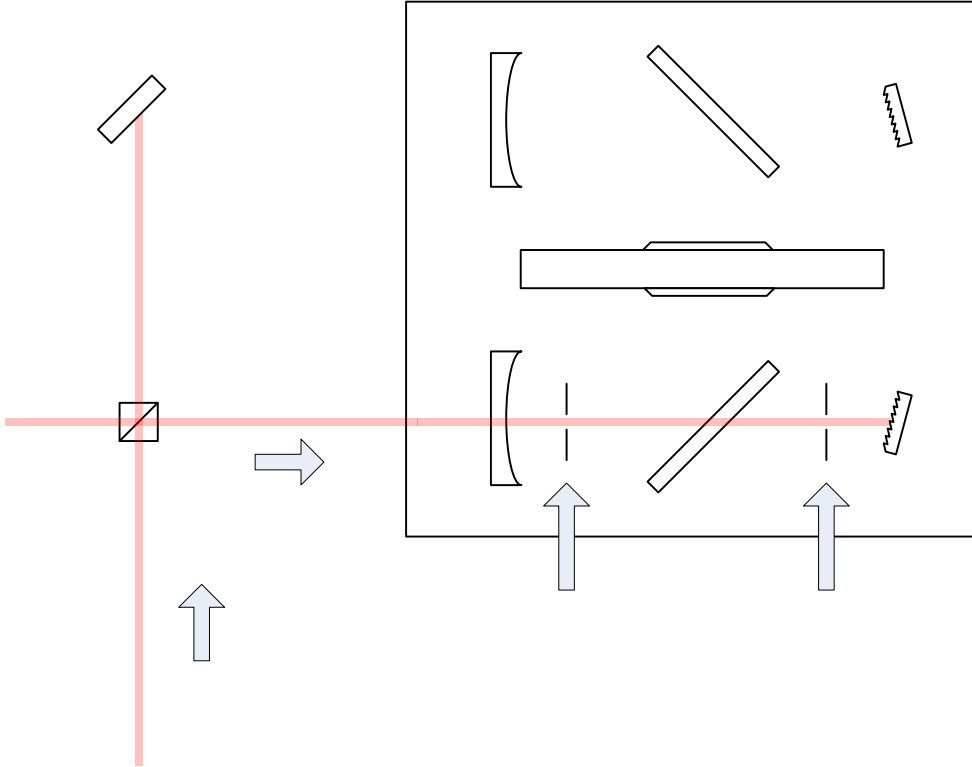
Figure 44: Step 2. Incident beam alignment.

input fold mirror, and the alignment hole between the input fold mirror and the input grating, ensure the beam enters the pulse shaper straight and at a constant height of $5''$ above the base plate, as shown in Fig. 44.

3. Align the grating by placing card (b) on the alignment hole between the focusing mirror and fold mirror, with the alignment mark on the side facing the grating. Alternate between the grating pitch, roll, and yaw adjustments to place the first order diffraction line on the horizontal line of the card. The diffraction line should be centered on the card. Use an IR indicator card or an IR scope to see the full extent of the spectrum (See Fig. 45).

4. Turn the alignment card around so that the mark faces the focusing mirror, as shown in Fig. 46. Adjust the pitch of the grating upwards until the beam passes over the card, reflects off of the focusing mirror and falls on the horizontal line on the card. It may be necessary to readjust the roll of the grating so that the diffraction line lies
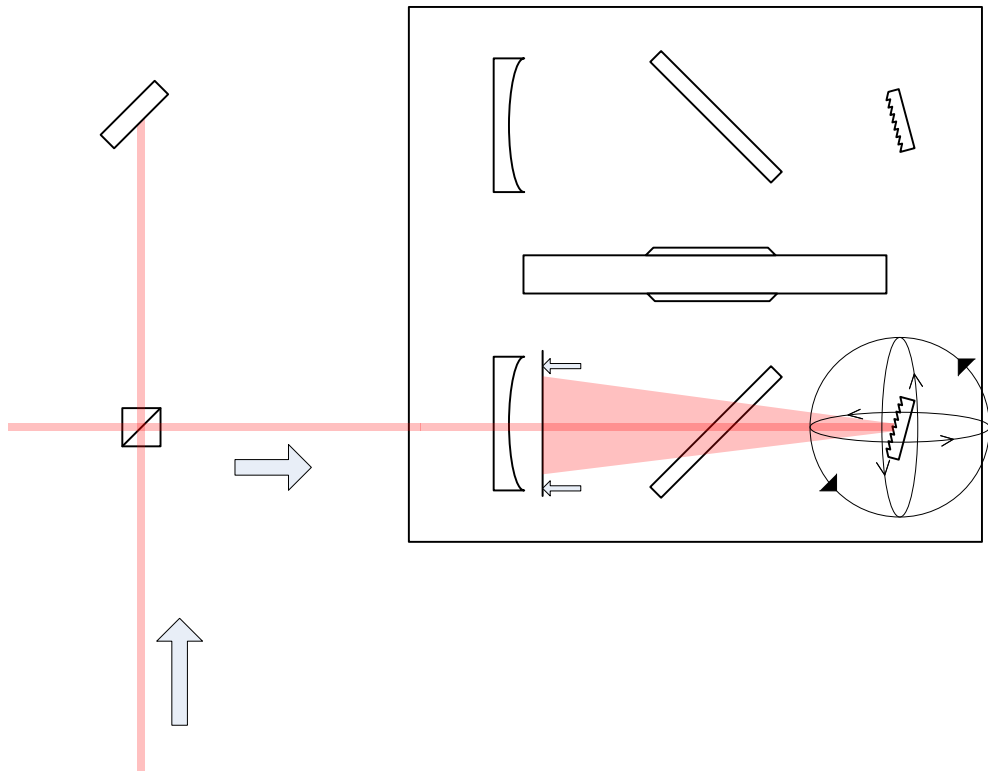
Figure 45: Step 3. Initial alignment of input grating.
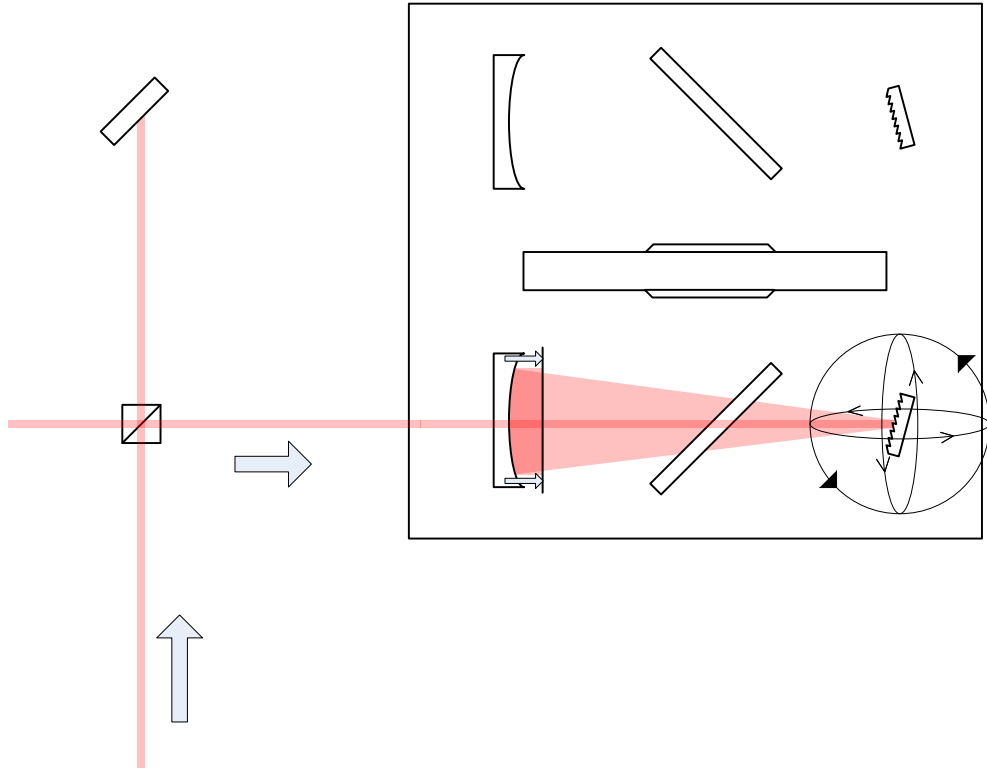
Figure 46: Step 4. Adjusting input grating pitch so beam after focusing mirror is at the correct height.

parallel to the horizontal line on the card.

5. Move the card to the alignment hole between the fold mirror and the SLM, and adjust the focus mirror to center the diffraction line on the card and bring it to horizontal as in Fig. 47.

6. Place the card on the alignment hole on the opposite side of the SLM and adjust the fold mirror accordingly. See Fig. 48.

7. Note whether the beam is clipped at the top or the bottom by the SLM aperture, and adjust the grating's pitch to minimize this clipping.

8. Iterate on these three adjustments until the diffraction line is centered and lies straight along the card's horizontal line. To verify this alignment, remove the exit fold mirror (see Fig. 49) and place card (c) at a distance down the table. Any error in the tilt of
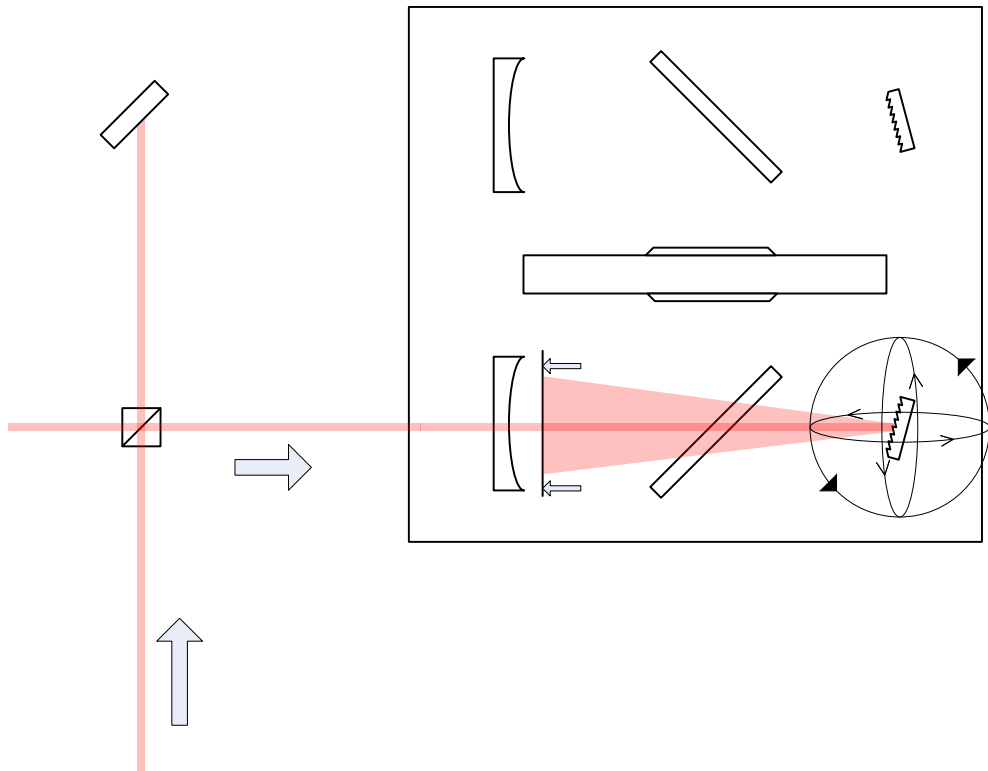
Figure 47: Step 5. Aligning input focusing mirror.
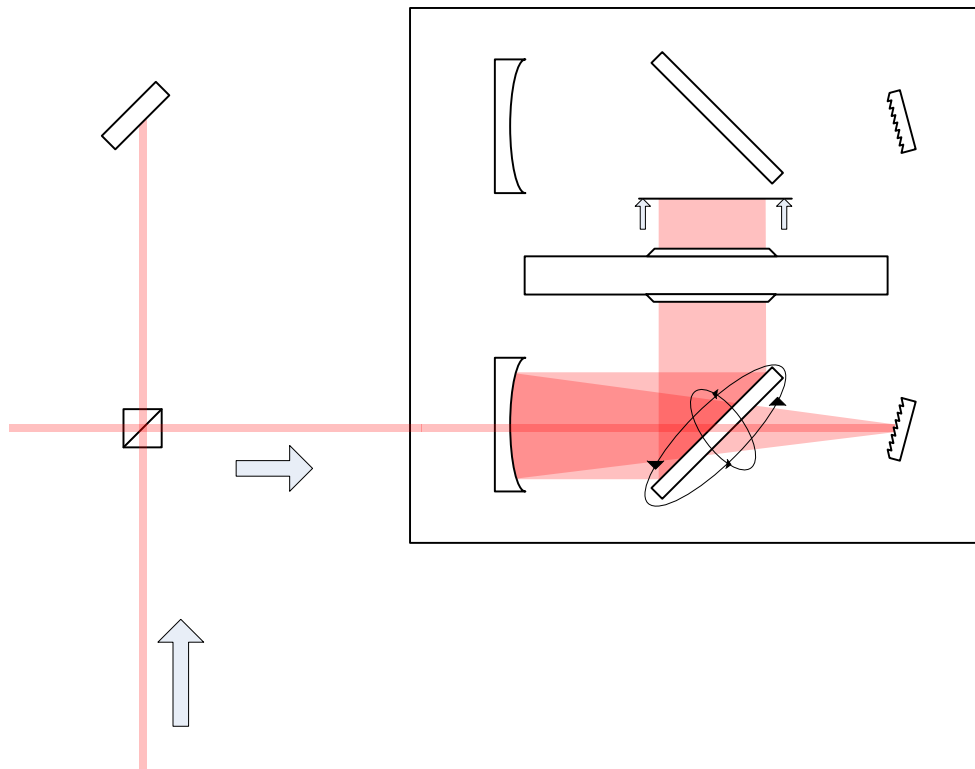
Figure 48: Step 6. Align input side fold mirror by observing beam on opposite side of the SLM.
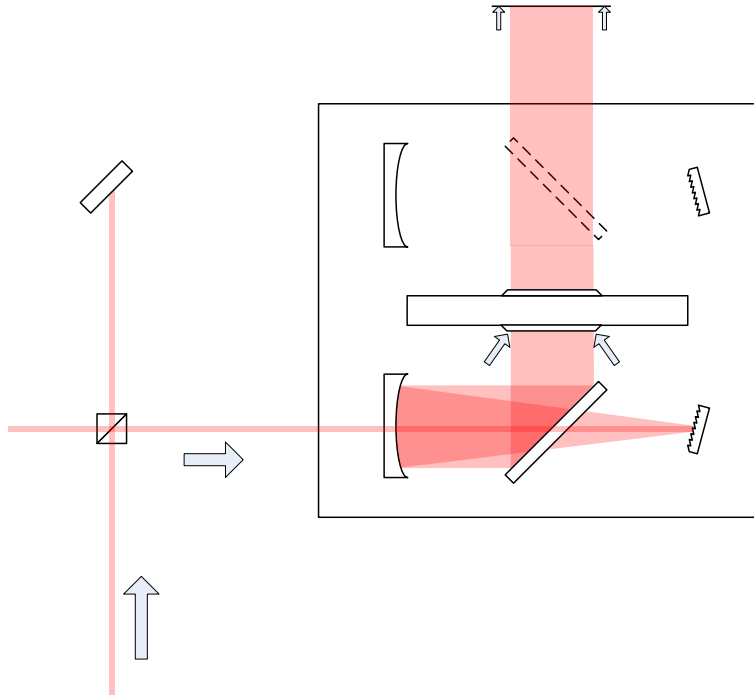
Figure 49: Step 8. With the output side fold mirror removed, poor collimation and beam tilt will be evident on a card placed far away. Dispersed spectrum should be centered on the SLM.

the beam will be evident with further propagation. At this point, use an IR viewer to ensure the dispersed spectrum is centered on the SLM.

9. Trace the surface reflection from the SLM back to the input grating, as shown in Fig. 50. *NEVER* perform this step with a laser amplifier running at full power! If the laser light is intense enough, it should be visible with an IR scope as a line on the focusing mirror and a spot on the grating (though these spots will not be distinguishable from the incident spots if they overlap well). In all cases, the back-reflection should overlap the input beam. Use the fold mirror to adjust the overlap on the focusing mirror, the focusing mirror to adjust the overlap on the grating, and the grating to adjust the overlap somewhere upstream (swiping an index card through the path of the beam to compare the input beam to the back-reflection). Be careful where this back-reflection goes, as it might leave the pulse shaper at such an angle
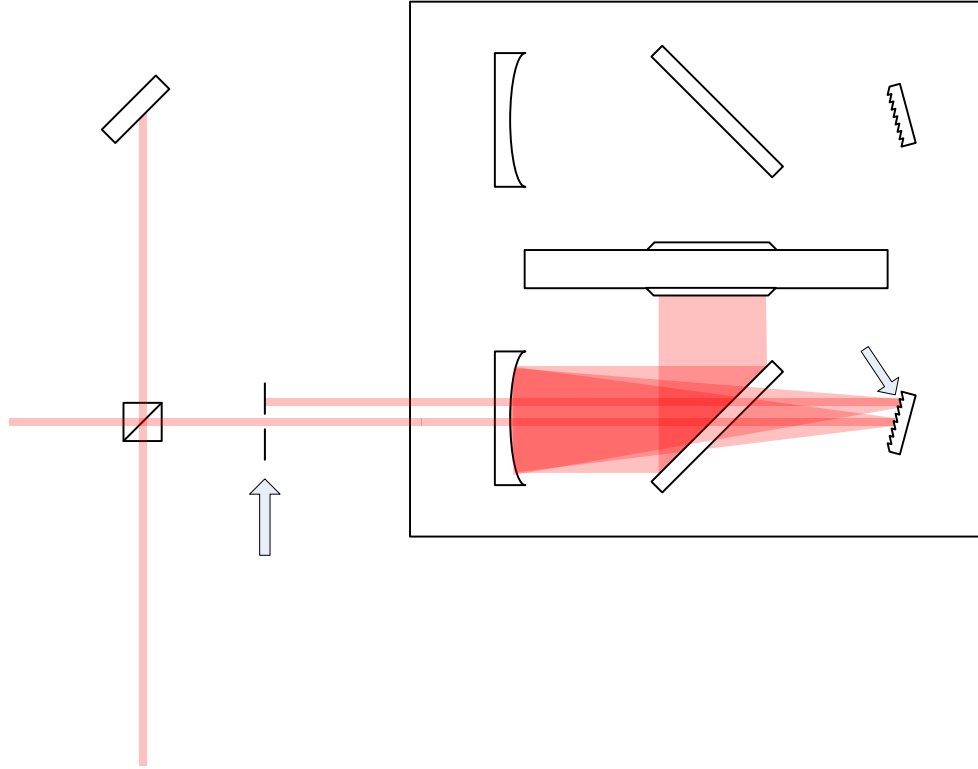
Figure 50: Step 9. Tracing back-reflection off of SLM surface. Adjust optics such that incident and reflected beams overlap on the grating surface and upstream from the shaper.

that it could travel to eye-level. If the alignment is being performed with an oscillator (not amplified), then when the surface reflection is well-aligned it may feed back into the oscillator causing CW breakthrough, producing a bright vertical band visible on the SLM's entrance aperture. This indicates good shaper alignment.

10. Redirect the input beam to the input side of the pulse shaper and repeat.

Once the above steps are complete, beams from both arms of the optical ring should overlap closely, leading to interference fringes observable in the far-field. When well aligned, you should be able to slide the gratings and focusing mirrors along their translation stages without affecting this overlap. This condition is critical; otherwise adjustment of the compressor for short pulses will steer the output beam and even distort the spatial mode. At this point, the SLM should be rotated just enough to prevent the back-reflection from feeding back into the laser source.

When properly aligned, the output half of the pulse shaper should compensate perfectly for the spatial dispersion of the input half. The output beam will ideally have the same spatial characteristics of the input beam. It should have the same diameter, and be well-collimated. There should be no spatial chirp; that is, the frequency components should be evenly distributed across the profile of the beam.

B.2   Temporal Dispersion Alignment

As noted before, the pulse shaper is a zero-dispersion stretcher. Ideally aligned to a $4f$ configuration, the shaper should neither stretch nor compress pulses. However for best pulse shaping results and phase fidelity, the SLM should only have to compensate for as little phase as possible to obtain transform-limited pulses. Hence the Martinez stretcher should be adjusted to compress the pulses as best as possible. The best approach we have found is to remove the optical ring and direct the beam into the input side of the pulse shaper, then place a doubling crystal after the output side. Adjusting *only* the optics on the output side of the shaper, optimize the SHG light.

Appendix C

NOTES ON PULSE MEASUREMENT WITH FROG

Throughout the course of aligning pulse shapers and acquiring data for this thesis, we have learned many valuable lessons regarding the frequency-resolved optical gating (FROG) technique for ultrafast pulse measurement [30]. Some of our initial assumptions, equipment, and phase retrieval efforts have cost many hours only to yield unreliable results. These notes are recorded in hopes that others will not have to learn these lessons the hard way.

Once the basic alignment of the FROG is complete, ensuring the incident pulses are of the proper polarization, it is important to fine-tune the alignment, iterating on three adjustments: temporal overlap, spatial overlap, and spectrometer steering. Maximizing the SFG signal seen by the spectrometer by iterating on these three adjustments ensures the best signal-to-noise ratio of the measured pulses.

We found that using a high-quality motor with an internal position encoder (such as the Newport LTA-HS) leads to the best FROG traces. A poor quality motor leads to asymmetry and visible striations in the FROG traces. These artifacts, if severe, can lead to poor convergence in the reconstruction algorithm and cast doubt on the retrieved phase.

Data conditioning is also crucial for accurate reconstructions. First, the experimental trace is trimmed according to the rule of thumb: "an island of data in a sea of zeros" [44]. That is no pulse energy should be present at the outer edges of the trace, nor should any measurable pulse energy be clipped by the conditioning process. The trace should occupy at most one fourth, but more ideally one eighth of the total trace area. The data should also be centered both spectrally and temporally within the trace, according to the center of mass computed from the marginals.

Background subtraction is crucial. The reconstruction algorithm works by postulating a theoretical pulse, generating a theoretical FROG trace, comparing it to the measured trace, and then adjusting the theoretical pulse based on the observed differences. A theoretical

FROG trace of an ideal, theoretical pulse, contains no background noise. Since the pulse occupies a small area of the trace, any noise in the background will be a large area which disagrees sharply with the theoretical trace, leading to an unreliable formulation of the next iteration guess in the algorithm.

Since a well-measured FROG trace will extend to time-delays for which there is no detectable gate/probe overlap, we can use the spectra at the extreme ends of the trace for background subtraction. If additional noise is present, a simple thresholding of the trace works well to produce a clean zero background.

Finally the best reconstruction results have been achieved with the principal component generalized projection algorithm [31]. The procedure is outlined in Fig. 51. Here phase is retrieved from an experimental FROG trace by an iterative process. First we posit an initial guess $P(t)$. We construct a theoretical FROG trace from the guess by computing its outer product, circularly shifting each row to the right by its row index, and performing an fft() along the columns, and an fftshift() along both rows and columns. The squared magnitude of the result F_{th} is now in the form of an SHG-FROG trace, with spectra for each time delay along the columns. Next we apply an intensity constraint, which replaces the magnitude of the theoretical trace with the magnitude of the experimental trace, preserving the theoretical phase. With the intensity constraint applied, we undo the operations performed in generating the theoretical trace to coax the data back into an outer product form. We perform a singular value decomposition (SVD) on the outer product form matrix, and retain the principal component (that is, the eigenvector with the strongest contribution) as the next guess $P(t)$. This cycle repeats until the sum-squared error between the intensity of the theoretical and experimental traces is below acceptable limits. A simplified, but functional MATLAB version of the algorithm is presented in Fig. 52.
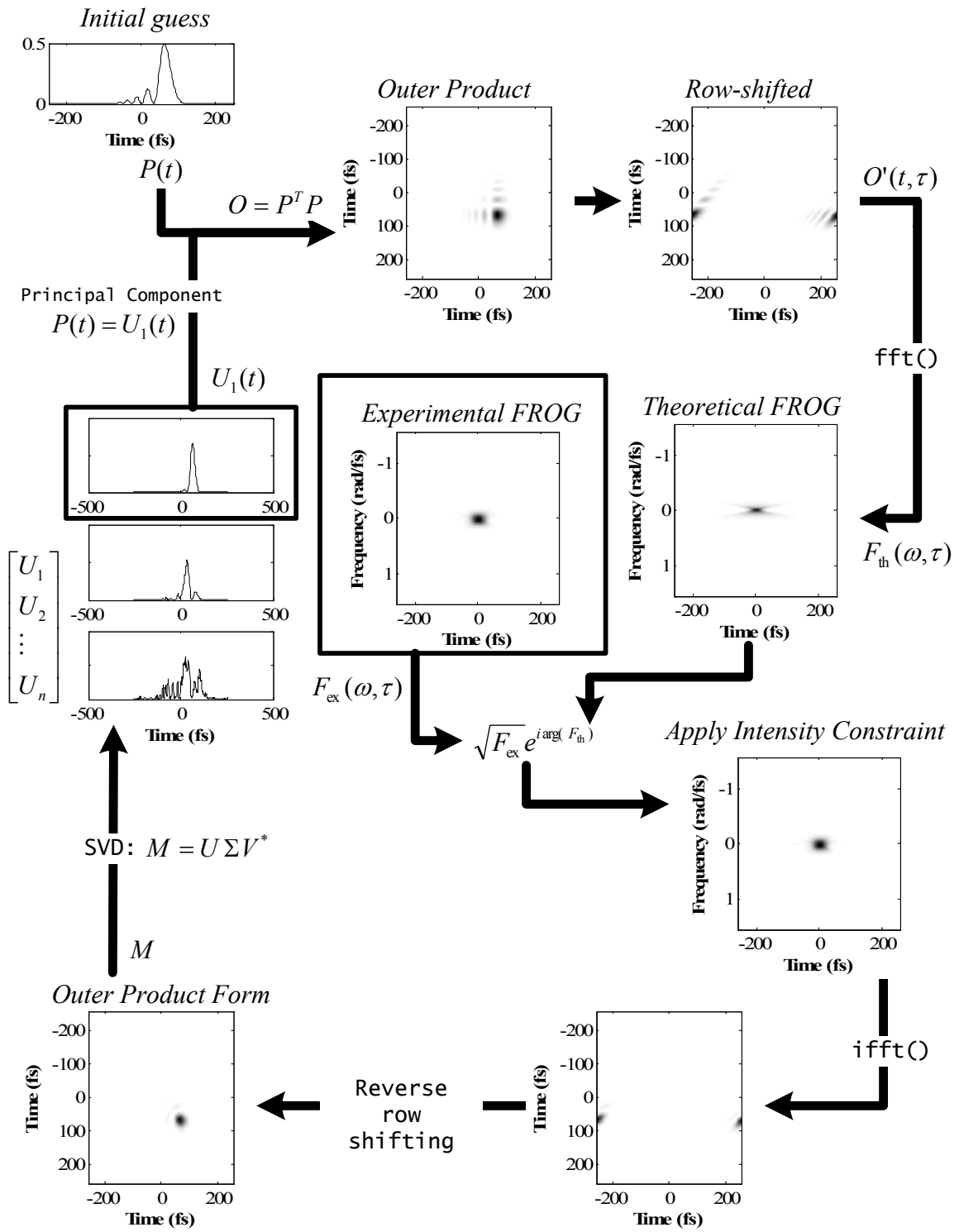
Figure 51: PCGP Algorithm.

```
1   % frgPCGP
2   % Jesse Wilson (2007)
3   % principal components SHG-FROG phase retrieval (Kane 1998)
4   % input arguments:
5   %   t           time axis of binned trace, in seconds
6   %   w           freq axis of binned trace, in rad/sec
7   %   Fexp        experimental binned FROG trace after background subtract
8   function E_t = frgPCGP( t, w, Fexp )
9       n = length(t);                          % no. of samples
10      Fexp = Fexp/max(max(abs(Fexp)));        % normalize binned trace
11      P = initialGuess( t, 20e-15 );          % generate initial guess
12      for iter = 1:512
13          P = P./max(abs(P));                 % normalize guess
14          O = P.'*P;                          % outer product
15          for iRow = 1:n                      %  row-shift
16              O(iRow,:) = circshift( O(iRow,:)...
17                  , [0 -(iRow-1)]);
18          end
19          O = fftshift( O, 2 );               % center time-zero
20          Fth = fftshift(fft( O, [], 1 ), 1 );   % fft along columns
21          Fthmag = conj(Fth).*Fth;            % mag. of guess trace
22          Fthmag = Fthmag/max(max(Fthmag));   % normalize
23          err = sum(sum( (Fexp-...            % error for this guess
24              Fthmag).^2 ))/(n^2);
25          frgGuess = sqrt(Fexp)...            % intensity constraint
26              .*exp(i*angle(Fth));
27          O = ifft(ifftshift(frgGuess,1),[],1);   % inverse fft
28          O=fftshift(O,2);                    % shift time-zero back
29          for iRow = 1:n                      % reverse row shifting
30              O(iRow,:) = circshift( O(iRow,:), ...
31                  [0 (iRow-1)]);
32          end
33          [U, W, V] = svds( O,1 );            % singular val. decomp.
34          P = transpose(U(:,1));              % principal component
35      end
36      E_t = P;
37  end
38
39  % initialGuess()
40  % given a time-axis, form a Gaussian pulse envelope as an initial guess.
41  function P = initialGuess( t, fwhm_t )
42      a0 = 2*log(2)/fwhm_t^2;
43      P = exp(-a0*t.^2);                      % gaussian pulse
44  end
```

Figure 52: PCGP-FROG phase retrieval MATLAB code.

Appendix D

LIST OF ACRONYMS AND ABBREVIATIONS

AOM Acousto-optic modulator

CMA-ES Covariance matrix adaptation evolutionary strategy

CW Continuous wave

DC Direct current (non-oscillatory)

DM Deformable mirror

ES Evolutionary strategy

FFT Fast Fourier transform

FROG Frequency resolved optical gating

fs Femtosecond (10^{-15} second)

FWHM Full width at half maximum

GDD Group delay dispersion

GVD Group velocity dispersion

IFFT Inverse fast Fourier transform

IR Infrared

LC Liquid crystal

PCGP Principal components generalized projection

SHG Second harmonic generation

SI Spectral interferometry

SLM Spatial light modulator

REFERENCES

[1] W. S. Warren, H. Rabitz, and M. Dahleh, "Coherent control of quantum dynamics - the dream is alive," *Science*, vol. 259, no. 5101, pp. 1581–1589, 1993.

[2] A. Assion, T. Baumert, M. Bergt, T. Brixner, B. Kiefer, V. Seyfried, M. Strehle, and G. Gerber, "Control of chemical reactions by feedback-optimized phase-shaped femtosecond laser pulses," *Science*, vol. 282, no. 5390, pp. 919–922, 1998.

[3] R. Bartels, S. Backus, E. Zeek, L. Misoguti, G. Vdovin, I. P. Christov, M. M. Murnane, and H. C. Kapteyn, "Shaped-pulse optimization of coherent emission of high-harmonic soft x-rays," *Nature*, vol. 406, no. 6792, pp. 164–166, 2000.

[4] R. J. Levis, G. M. Menkir, and H. Rabitz, "Selective bond dissociation and rearrangement with optimally tailored, strong-field laser pulses," *Science*, vol. 292, no. 5517, pp. 709–713, 2001.

[5] M. Artamonov, T. S. Ho, and H. Rabitz, "Quantum optimal control of ozone isomerization," *Chemical Physics*, vol. 305, no. 1-3, pp. 213–222, 2004.

[6] H. Rabitz, "Shaped laser pulses as reagents," *Science*, vol. 299, no. 5606, p. 525, 2003.

[7] R. A. Bartels, M. M. Murnane, H. C. Kapteyn, I. Christov, and H. Rabitz, "Learning from learning algorithms: Application to attosecond dynamics of high-harmonic generation," *Physical Review A*, vol. 70, no. 4, 2004.

[8] J. M. Geremia and H. A. Rabitz, "Efficient extraction of quantum hamiltonians from optimal laboratory data," *Physical Review A*, vol. 70, no. 2, 2004.

[9] R. S. Judson and H. Rabitz, "Teaching lasers to control molecules," *Physical Review Letters*, vol. 68, no. 10, pp. 1500–1503, 1992.

[10] C. J. Bardeen, V. V. Yakovlev, K. R. Wilson, S. D. Carpenter, P. M. Weber, and W. S. Warren, "Feedback quantum control of molecular electronic population transfer," *Chemical Physics Letters*, vol. 280, no. 1-2, pp. 151–158, 1997.

[11] J. Desbois, F. Gires, and P. Tournois, "New approach to picosecond laser pulse analysis shaping and coding," *IEEE Journal of Quantum Electronics*, vol. QE 9, no. 2, pp. 213–218, 1973.

[12] C. Froehly, B. Colombeau, and M. Vampouille, "Shaping and analysis of picosecond light-pulses," *Progress in Optics*, vol. 20, pp. 65–153, 1983.

[13] A. M. Weiner, J. P. Heritage, and E. M. Kirschner, "High-resolution femtosecond pulse shaping," *Journal of the Optical Society of America B-Optical Physics*, vol. 5, no. 8, pp. 1563–1572, 1988.

[14] A. M. Weiner, D. E. Leaird, J. S. Patel, and J. R. Wullert, "Programmable femtosecond pulse shaping by use of a multielement liquid-crystal phase modulator," *Optics Letters*, vol. 15, no. 6, pp. 326–328, 1990.

[15] A. M. Weiner, D. E. Leaird, J. S. Patel, and J. R. Wullert, "Programmable shaping of femtosecond optical pulses by use of 128-element liquid-crystal phase modulator," *IEEE Journal of Quantum Electronics*, vol. 28, no. 4, pp. 908–920, 1992.

[16] A. M. Weiner, "Femtosecond pulse shaping using spatial light modulators," *Review of Scientific Instruments*, vol. 71, no. 5, pp. 1929–1960, 2000.

[17] O. E. Martinez, "Matrix formalism for pulse compressors," *Ieee Journal of Quantum Electronics*, vol. 24, no. 12, pp. 2530–2536, 1988.

[18] A. M. Weiner, "Femtosecond optical pulse shaping and processing," *Progress in Quantum Electronics*, vol. 19, no. 3, pp. 161–237, 1995.

[19] A. E. Siegman, *Lasers.* University Science Books, Sausalito, California, 1986.

[20] R. N. Thurston, J. P. Heritage, A. M. Weiner, and W. J. Tomlinson, "Analysis of picosecond pulse shape synthesis by spectral masking in a grating pulse compressor," *IEEE Journal of Quantum Electronics*, vol. 22, no. 5, pp. 682–696, 1986.

[21] J. P. Heritage, R. N. Thurston, W. J. Tomlinson, A. M. Weiner, and R. H. Stolen, "Spectral windowing of frequency-modulated optical pulses in a grating compressor," *Applied Physics Letters*, vol. 47, no. 2, pp. 87–89, 1985.

[22] A. Präkelt, M. Wollenhaupt, A. Assion, C. Horn, C. Sarpe-Tudoran, M. Winter, and T. Baumert, "Compact, robust, and flexible setup for femtosecond pulse shaping," *Review of Scientific Instruments*, vol. 74, no. 11, pp. 4950–4953, 2003.

[23] M. Takeda, H. Ina, and S. Kobayashi, "Fourier-transform method of fringe-pattern analysis for computer-based topography and interferometry," *Journal of the Optical Society of America A*, vol. 72, no. 1, pp. 156–160, 1982.

[24] A. Yariv and P. Yeh, *Optical Waves in Crystals: Propagation and Control of Laser Radiation.* Wiley-Interscience, 1984.

[25] M. M. Wefers and K. A. Nelson, "Analysis of programmable ultrashort wave-form generation using liquid-crystal spatial light modulators," *Journal of the Optical Society of America B*, vol. 12, no. 7, pp. 1343–1362, 1995.

[26] C. W. Hillegas, J. X. Tull, D. Goswami, D. Strickland, and W. S. Warren, "Femtosecond laser-pulse shaping by use of microsecond radiofrequency pulses," *Optics Letters*, vol. 19, no. 10, pp. 737–739, 1994.

[27] J. C. Vaughan, T. Hornung, T. Feurer, and K. A. Nelson, "Diffraction-based femtosecond pulse shaping with a two-dimensional spatial light modulator," *Optics Letters*, vol. 30, no. 3, pp. 323–325, 2005.

[28] E. Frumker, E. Tal, Y. Silberberg, and D. Majer, "Femtosecond pulse-shape modulation at nanosecond rates," *Optics Letters*, vol. 30, no. 20, pp. 2796–2798, 2005.

[29] S. Akturk, X. Gu, M. Kimmel, and R. Trebino, "Extremely simple single-prism ultrashort-pulse compressor," *Optics Express*, vol. 14, no. 21, pp. 10101–10108, 2006.

[30] D. J. Kane and R. Trebino, "Characterization of arbitrary femtosecond pulses using frequency-resolved optical gating," *IEEE Journal of Quantum Electonics*, vol. 29, no. 2, pp. 571–579, 1993.

[31] D. J. Kane, "Real-time measurement of ultrashort laser pulses using principal component generalized projections," *IEEE Journal of Selected Topics in Quantum Electronics*, vol. 4, no. 2, pp. 278–284, 1998.

[32] P. Schlup, J. Wilson, K. Hartinger, and R. A. Bartels, "Dispersion-balancing of variable-delay monolithic pulse splitters," *Submitted to Applied Optics*, 2007.

[33] E. K. P. Chong and S. H. Żak, *An Introduction to Optimization.* John Wiley & Sons, 2 ed., 2001.

[34] B. J. Pearson, J. L. White, T. C. Weinacht, and P. H. Bucksbaum, "Coherent control using adaptive learning algorithms," *Physical Review A*, vol. 6306, no. 6, 2001.

[35] H. Rabitz, R. de Vivie-Riedle, M. Motzkus, and K. Kompa, "Chemistry - whither the future of controlling quantum phenomena?," *Science*, vol. 288, no. 5467, pp. 824–828, 2000.

[36] H. A. Rabitz, M. M. Hsieh, and C. M. Rosenthal, "Quantum optimally controlled transition landscapes," *Science*, vol. 303, no. 5666, pp. 1998–2001, 2004.

[37] N. Hansen and A. Ostermeier, "Adapting arbitrary normal mutation distributions in evolution strategies: The covariance matrix adaptation," *Proceedings of the 1996 IEEE International Conference on Evolutionary Computation*, pp. 312–317, 1996.

[38] N. Hansen, "The cma evolution strategy: A tutorial." http://www.bionik.tu-berlin.de/user/niko/cmaesintro.html, November 2005.

[39] R. W. Boyd, *Nonlinear Optics.* San Diego, CA: Academic Press, 2 ed., 2003.

[40] R. Trebino, *Frequency-resolved optical gating: the measurement of ultrashort laser pulses.* Boston: Kluwer Academic Publishers, 2000.

[41] A. Nazarkin, G. Korn, M. Wittmann, and T. Elsaesser, "Generation of multiple phase-locked stokes and anti-stokes components in an impulsively excited raman medium," *Physical Review Letters*, vol. 83, no. 13, pp. 2560–2563, 1999.

[42] N. Dudovich, D. Oron, and Y. Silberberg, "Single-pulse coherently controlled nonlinear raman spectroscopy and microscopy," *Nature*, vol. 418, no. 6897, pp. 512–514, 2002.

[43] P. O'Shea, M. Kimmel, X. Gu, and R. Trebino, "Highly simplified device for ultrashort-pulse measurement," *Optics Letters*, vol. 26, no. 12, pp. 932–934, 2001.

[44] R. Trebino, K. W. DeLong, D. N. Fittinghoff, J. N. Sweetser, M. A. Krumbugel, B. A. Richman, and D. J. Kane, "Measuring ultrashort laser pulses in the time-frequency domain using frequency-resolved optical gating," *Review of Scientific Instruments*, vol. 68, no. 9, pp. 3277–3295, 1997.